Capabilities of a Closely-Packed, Wearable Radiation Detector Array: Source Localization, Directionality, and Multi-Modal Data Fusion

A Dissertation Presented for the

Doctor of Philosophy

Degree

The University of Tennessee, Knoxville

Carl G. Britt III

May 2021

© by Carl G. Britt III, 2021
All Rights Reserved.

Acknowledgments

I would like to thank the members of my PhD committee: Dr. Jason Hayward, Dr. Cari Seifert, Dr. Hairong Qi, and Dr. Peter Angelo. Their feedback throughout the dissertation process and life wisdom imparted during our interactions were invaluable. Some of this wisdom I had naively disbelieved, but ultimately proved to be true throughout my graduate career. Each member's support through this process, especially at the end of the PhD, was especially helpful.

Thanks to Elliot Greenlee for developing the video object detection and tracking strategy, Steven Patrick and Michael Han for further developing its implementation, and Stephanie Kreutz for propsing new and novel target tracking approaches.

Thanks to Caleb Redding and Cordell Delzer for assisting with the dynamic source localization experiment on short notice. They donated their free time to demonstrate the capability shown in this work.

A special thanks goes out to my family and friends who supported me through this ordeal.

Thanks goes out to the administrative and technical staff at the NE department working behind the scenes. Both Tonya Mathes and Candy Anderson for dealing with the funding accounts related to CNEC, Michelle McBee for everytime I messed up the travel reimbursement forms, Ashly Pearson for everytime I needed equipment or a specific setup, and Scott Emert for letting me use the workshop which was pivotal in some of the experiments performed.

Thanks goes out to the coordinators, Stefani Buster and Bernie Kirk, at CNEC for the access to a large number of opportunities.

And last but certainly not least, our sponsors. This material is based upon work supported by both the Department of Homeland Security and Department of Energy

National Nuclear Security Administration under Award Numbers DHS-15-DNDO-077-001 and DE-NA0002576. This report was prepared as an account of work sponsored by an agency of the United States Government. Neither the United States Government nor any agency thereof, nor any of their employees, makes any warranty, express or implied, or assumes any legal liability or responsibility for the accuracy, completeness, or usefulness of any information, apparatus, product, or process disclosed, or represents that its use would not infringe privately owned rights. Reference herein to any specific commercial product, process, or service by trade name, trademark, manufacturer, or otherwise does not necessarily constitute or imply its endorsement, recommendation, or favoring by the United States Government or any agency thereof. The views and opinions of authors expressed herein do not necessarily state or reflect those of the United States Government or any agency thereof.

Abstract

The capability of assigning source carrier probabilities by fusing both video and radiation data is demonstrated. Potential targets are automatically detected and tracked with computer vision techniques. Meanwhile, a newly developed method for exploiting the angular response of closely-packed radiation detector arrays points towards a radiation source using short, periodic measurements on the order of 1 s. Source carrier probabilities are then assigned after the object's movement measured from the video data stream is correlated with the radiation directionality estimates over a set period of time. In demonstrating source carrier probability assigned to moving sources, three main contributions were made. A radiation directionality algorithm was developed and characterized for a detector array as a function of unattenuated gamma fluence. The Mean Absolute Error (MAE) was measured to be 8.2 degrees using a 113 uCi Cs-137 source and 17.8 degrees using a 35 uCi Co-60 source, where both sources were placed 172.4 cm away and 1 s measurement times were used. The source localization capabilities of the WIND backpack detector array was characterized for source offsets up to 5.2 m for a variety of experimental variables such as integration time and detector speed. Finally, the data fusion strategy was developed such that probabilities calculated with the directionality algorithm could be appropriately accounted and attributed to tracked targets from the video data stream. It was found that the data fused result improved the radiation only result from a MAE of 18 degrees to 8 degrees for a 113 uCi Cs-137 source at an average distance and speed of 4 m and 0.6 m/s, respectively.

Table of Contents

1 Introduction **1**

1.1 Background . . . 1

1.2 Related Measurement Platforms in Previous Work . . . 1

1.2.1 Commercially Off The Shelf Systems . . . 1

1.2.2 Imagers . . . 2

1.2.3 Detector Arrays . . . 6

1.3 Source Localization Approaches . . . 11

1.3.1 Source Directionality Approaches . . . 17

1.3.2 The Role of Data Fusion . . . 19

1.4 Dissertation Contributions . . . 26

1.4.1 WIND Backpack Detector Array . . . 26

1.4.2 Agnostic Method Development for Detector Arrays . . . 30

2 The Use of Radiation Detector Occlusion for Directionality **33**

2.1 Introduction . . . 33

2.2 Methodology . . . 36

2.2.1 Experimental Setup for Static Detector Array, Static Source Case . . . 37

2.2.2 Experimental Setup for Static Detector Array, Mobile Source Case . . . 40

2.2.3 Directionality Algorithm . . . 42

2.3 Results . . . 46

2.3.1 Angular Response Measurements . . . 46

2.3.2 Directionality Performance for the Stationary Detector Array, Stationary Source . . . 50

2.3.3 Directionality Demonstration in the Stationary Detector Array, Moving Source . . . 58
2.4 Conclusions . . . 61
2.5 Acknowledgements . . . 62

3 Source Localization of the WIND Backpack Detector Array 63
3.1 Introduction . . . 63
3.2 Methodology . . . 64
3.2.1 Angular Response . . . 64
3.2.2 Radiation Transport . . . 64
3.2.3 Maximum Likelihood Expectation Maximization . . . 67
3.2.4 Experimental Setup . . . 69
3.3 Results . . . 74
3.3.1 Iteration Convergence Criteria . . . 74
3.3.2 Source Type and Source Offset . . . 80
3.3.3 Integration Time and Detector Array Speed . . . 84
3.3.4 Energy Threshold . . . 88
3.3.5 kSigma . . . 92
3.4 Conclusions . . . 92
3.5 Acknowledgements . . . 94

4 Fusion of Radiation and Video Data Modalities 95
4.1 Introduction . . . 95
4.2 Methodology . . . 98
4.2.1 Data Fusion Algorithm . . . 98
4.2.2 Experimental Setup . . . 104
4.3 Results . . . 106
4.3.1 SCP Calculation Example . . . 106
4.3.2 DFM Scenario Commentary . . . 108
4.3.3 DFM Performance Summary . . . 112
4.4 Conclusions . . . 113

4.5 Acknowledgements 116

5 Conclusions **117**

5.1 Future Work 118

5.2 Acknowledgements 119

Bibliography **120**

Appendix **127**

A Source Localization Using the Government Reference System 128

A.1 Preliminary Dataset 128

A.2 Preliminary Results 133

Vita **141**

List of Tables

1.1 Summary of Commercial Off The Shelf (COTS) equipment for radiation detection applications from SAVER market surveys. Items denoted with "*" denotes that this system can be made man-portable 3

1.2 Ideal characteristics for backpack detector array design 29

3.1 Sample calculation times with respect to number of MLEM iterations for a 30 s data segment. 70

4.1 Subset of data fusion results. The row in dark gray is the specific time step mentioned in the text. PDF values denote the single time step probabilities as given by the radiation directionality algorithm for the tracked object. SCP values denote the source carrier probabilities given the tracked object directionality histories from both the radiation and video data modalities. The PDF values of the rows in light gray are used to calculate the SCP value of the row in dark gray. 107

1 Summary of Results: 2D Gaussian optimal fitting parameters. 139

List of Figures

1.1 Source localization using the LAI array using CAI. (Left) Picture of the LAI. (Right) Source localization result which represents a top-down view of the world. Both images from [46] 4

1.2 Source localization using the MISTI system using CAI. (Left) Picture of the MISTI system. (Right) Source localization result which represents a slice of a three-dimensional view of the world. Both images from [20]. 5

1.3 (Top) MURS measurement platform. This is a SUV-borne system. (Bottom) MLEM Result on simulated data. 7

1.4 (Top) MURS detector array configuration. (Bottom) Angular response (energy spectra) of the MURS detector array due to a Co-60 source placed 2m away at chosen angles. Both images are from Reference [7]. 8

1.5 (Top) Airborne Radiological Enhanced-sensor System (ARES), also known as the Helicopter-based Stand-Off Radiation Detection System (HeliSORDS), with typical flight parameters from Reference [29]. (Bottom) Probability map generated using Maximum Likelihood Estimation from Reference [25]. 9

1.6 (Top) HeliSORDS CsI array geometry. (Bottom) Angular response (normalized count rates) heat map for one of the detectors in the array. Both figures from Reference [23]. 10

1.7 (Top) Source localization experiment. A detector system in a truck is driven past a potential source location denoted by the red 'x'. The optimal integration window is the time it takes to travel from -x_0 to x_0, spanning 108^o in front of the source. (Bottom) Source localization map denoting the SNR with respect to position. This was generated with measured data. The source is a 200 μCi I-131 located at the black 'x'. From Reference [1]. 12

1.8 Source localization results on synthetic data describing a helicopter flying 70 knots in a straight line at an altitude of 83 m. (Top 3) Source localization estimates for each run. 10 runs were done for each input type. (Bottom) Error distribution with respect to source strength for different source offsets and input data types. From Reference [29]. 14

1.9 Source localization results on synthetic data describing a helicopter flying 70 knots in a straight line at an altitude of 83 m. Error distribution with respect to source strength for different source offsets and input data types. From Reference [29]. 15

1.10 Source localization results where the color of each pixel denotes source strength. From left to right. 1) Ground truth K40 (background NORM) activity distribution. 2) Ground truth Cs-137 activity distribution. 3) Reconstructed K40 activity distribution. 4) Reconstructed Cs137 activity distribution. From Reference [34]. 16

1.11 Source localization results from Reference [41]. (Left) Source localization result using measurements from a single detector array at a fixed position. Scenario is a 750 μCi Co-60 source at a distance of 762 cm away from the array. As shown, this localization result can be interpreted as directionality: source direction estimates relative to the system. (Right) Source localization result using measurements from two detector arrays at 2 different locations. The two detector arrays were placed 914.4 cm away from each other. The 750 μCi Co-60 was placed 304.8 cm perpendicularly away from the halfway point between the detector arrays. 18

1.12 Compton scattering distributions as a function of Cs-137 source position. Each plot represents the energy spectra measured for coincidence events. The left column of plots is when the source is placed at 90^o. The right column of plots is when the source is placed at 45^o. (Top left) Energy spectrum from the left detector. (Middle left) Energy spectrum from the right detector. (Bottom left) Summed energy spectrum from both detectors. (Top right) Energy spectrum from the left detector. (Middle right) Energy spectrum from the right detector. (Bottom right) Summed energy spectrum from both detectors. All plots from Reference [15]. 20
1.13 (Top) Mean energy difference signature from Reference [15]. (Bottom) Energy spectra covariance between two detectors for coincident events from Reference [30]. 21
1.14 Real-time source tracking concept introduced by Reference [41]. Multiple detector arrays with directionality estimates tracking and pursuing the lone source carrier. 23
1.15 Localization error as a function of measurement time. Different localization algorithms were used: Maximum Likelihood Estimation (MLE) and Maximum Likelihood Expectation Maximization (MLEM). Omni refers to the use of non-directional radiation detectors. Plot from Reference [8]. 24
1.16 Source localization performance with respect to included measurement time for a sensor network from Reference [19]. 25
1.17 Scene Data Fusion concept. Source localization using a CI coupled to a Microsoft Kinect. (Top) Detector system. (Middle) Source localization result, radiation data only. (Bottom) Source localization result, fused data. Figures from Reference [3] 27
1.18 Data fusion between video RGB data and count rate data from a 2" × 4" × 16" NaI(Tl). Source strengths are attributed automatically to detected objects given their movement history. Figure from [28]. 28

1.19 Data fusion between LIDAR pointcloud data and count rate data from a EJ-309. Source is a 131 μCi Cf-252. (Left) RGB camera footage. Not used in the calculation. (Middle) LIDAR pointcloud of the scene, top down view. (Right) Distance to each person above the plot of the radiation data. Figures from [17]. 28
1.20 Built WIND Backpack detector array. 31

2.1 Source directionality illustrated in a hypothesized choke point monitoring scenario, such as a ticket check-in while boarding an airplane. Each time step involves a source position estimate as denoted by the conic, cross-hatched projection. The width of the source position estimates the probable source locations with a 95% probability. (Top) Source position estimate at time=0s. (Middle) Source position estimate at t=1s. (Bottom) Source position estimate at t=2s. 35
2.2 (Top) Measured net count rates of all 3 dimensions of angles 0, 15, 30, and 45 degrees. (Bottom) Measured net count rates of all 3 dimensions of angles 0, 15, 30, and 45 degrees after being normalized to the 1-norm. 38
2.3 (Top) Sodium Iodide detector array geometry. 2" $\times$ 2" $\times$ 4" rectangular crystals. Phantom not shown, but is to be included in the angular response measurement. (Bottom) Two-dimensional cross section of the detector array geometry, top-down view. All units are in centimeters. Human phantom is approximated with an ellipsoid. The marked cross hatch circle is the defined center of the system for the entire angular response measurement. 39
2.4 Experimental setup photo of the angular response measurement with the source position labeled with a yellow circle. The source is located at a fixed distance but is placed at different angles with respect to the center of the array. Both the centers of the source and the detectors are at the same height. 41

2.5 (Top) In action picture of the stationary detector array, moving source experiment. The right experimentalist is carrying the only Cs-137 source in his left hand. Experimentalists are moving left to right, right to left, front to aft, and aft to front throughout the measurement. (Bottom) Stationary detector array, moving source experimental setup. See Figure 2.3 for the top down view of the array used in this experiment as well as a detailed schematic. 43

2.6 Comparison between the 1-normed count rates of angular groups 0 (red), 30 (blue), and 60 (green) degrees. Plots are histograms across each Cartesian dimension. The top is the higher statistics case, while the bottom represents the case in lower statistics. (Top) 133.3 μCi Cs-137 source at 172.4cm. (Bottom) Same source at 304.8cm. 45

2.7 (Top) Measured angular response for a 113.3 μCi Cs-137 source at 172.4 cm. The polar angle represents source position in degrees, while the radius denotes magnitude in (cps). (Bottom) Measured angular response for a 113.3 μCi Cs-137 source at 172.4 cm after normalization. Polar angle corresponds to source position in degrees, while the radius denotes magnitude but is unitless due to normalization. 47

2.8 (Top) Measured angular response for a 113.3 μCi Cs-137 source at 304.8 cm. The polar angle represents source position in degrees, while the radius denotes magnitude in (cps). (Bottom) Measured angular response for a 113.3 μCi Cs-137 source at 304.8 cm after normalization. Polar angle corresponds to source position in degrees, while the radius denotes magnitude but is unitless due to normalization. 48

2.9 (Top) Measured angular response for a 34.6 μCi Co-60 source at 172.4 cm. The polar angle represents source position in degrees, while the radius denotes magnitude in (cps). (Bottom) Measured angular response for a 34.6 μCi Co-60 source at 172.4 cm after normalization. Polar angle corresponds to source position in degrees, while the radius denotes magnitude but is unitless due to normalization. 49

2.10 (Top) Directionality performance while trained with a 113.3 μCi Cs-137 source at 172.4 cm while observing a 113.3 μCi Cs-137 at 172.4 cm. (Bottom) Directionality performance while trained with a 113.3 μCi Cs-137 source at 172.4 cm while observing a 113.3 μCi Cs-137 at 304.8 cm. 51
2.11 Probability with respect to deviation from ground truth source angle. (Top) Directionality estimates at a source angle of 30°. (Bottom) Directionality estimates at a source angle of 285°. 52
2.12 (Top) Directionality performance while trained with a 113.3 μCi Cs-137 source at 172.4 cm while observing a 113.3 μCi Cs-137 at 172.4 cm using 0.5s as the integration time. (Bottom) The same as the top plot, but using 5s as the integration time. 54
2.13 (Top) Directionality performance while trained with a 34.6 μCi Co-60 source at 172.4 cm while observing a 34.6 μCi Co-60 at 172.4 cm. Integration time for both is 1 s. (Bottom) Directionality performance with a 34.6 μCi Co-60 source, 172.4 cm, integration time of 1 s source template observing a 34.6 μCi Co-60, 172.4 cm, integration time of 5 s. 55
2.14 Directionality performance with respect to uncollided gamma fluence. The top equation is a fit for the Co-60 MAE, while the bottom equation is a fet for the Cs-137 MAE. 57
2.15 Directionality performance and count rates of detector 1, both with respect to set energy threshold. The blue squares denote MAE values which use the left axis, while the red diamonds and yellow triangles denote detector 1 count rate values using the right axis. The red diamonds represent the minimum count rate, the count rate of detector 1 when the source is placed at 0°. The yellow triangles represent the maximum count rate, the count rate of detector 1 when the source is placed at 180 °. Detector 1 is chosen arbitrarily, as all 3 detectors trend with one another at 0° and 180°. A 113.3 μCi Cs-137 at 172.4 cm was used with a 1 s integration time for the MAE, and the count rates were measured in the same manner as the angular response measurements. . 59

2.16 (Top) Directionality comparison to the ground truth in the static detector array, moving source case. As mentioned in the Methodology, ground truth source angle is known to 0.6° ± 0.9°, but is not plotted for clarity. (Bottom) Directionality performance as observed from the static detector array, moving source experiment. 60

3.1 (Left) Measured angular response for a 95 μCi Co-57 source at 172.4 cm. The polar angle represents source position in degrees, while the radius denotes detector count rate in cps. Uncertainties are the standard deviation of the count rate across the 5 minute measurement. (Right) Measured angular response for a 95 μCi Co-57 source at 172.4 cm after L1 normalization. Polar angle corresponds to source position in degrees, while the radius denotes magnitude but is unitless due to normalization. 65

3.2 (Left) Measured angular response for a 113 μCi Cs-137 source at 172.4 cm. The polar angle represents source position in degrees, while the radius denotes detector count rate in cps. (Right) Measured angular response for a 113 μCi Cs-137 source at 172.4 cm after normalization. Polar angle corresponds to source position in degrees, while the radius denotes magnitude but is unitless due to normalization. 66

3.3 The source localization detector array setup. At the top left is a silver component: a custom power supply used to power the two ORTEC Model 113 preamplifiers. At the bottom left is a black box which is the lithium ion battery. The detector array is positioned at the bottom middle. At the top middle, there are the two brown Model 113 preamplifiers. At the bottom right is the CAEN DT5725 digitizer. Finally, the laptop used for data acquisition is shown at the top right. 72

3.4 Source localization experiment in action. The experimenter moving at walking speed pushes a cart containing the detector array along one of the straight lines past a radiation source positioned at the same height as the center of the detectors. 73

3.5 An example of an acquired point cloud during the experiment. At the middle of the point cloud, an experimentalist is pushing the cart setup shown in Figure 3.4. At the left of the point cloud, the red points denote contours describing the floor of the room. The back wall can be found at the top of the image labeled by green points. Towards the right of the figure, the cluster of points describes a wall with windows. 75
3.6 Sample of a source localization result. Red "x" denotes ground truth source position. Green dots denote detector array positions. The source was a 113 μCi Cs-137 source at a 2.2 m source offset. Detector array speed was at 0.46 m/s, and the net count rate was taken after a 81 keV energy threshold was applied with a 1.00 s time integration. MLEM iterations set to 10,000. . . . 76
3.7 Sample of a source localization result. Red "x" denotes ground truth source position. Green dots denote detector array positions. The source was a 113 μCi Cs-137 source at a 2.2 m source offset. Detector array speed was at 0.46 m/s, and the net count rate was taken after a 81 keV energy threshold was applied with a 1.00 s time integration. MLEM iterations set to 100,000. . . . 77
3.8 Localization RMS with respect to source offset using 30 s measurements. Results for a 113 μCi Cs-137 with 1.00 s time integrations and 0.46 m/s detector array speed. See the text for analysis. 78
3.9 Localization performance with respect to source offset using 30 s measurements. Results for a 113 μCi Cs-137 with 1.00 s time integrations and 0.46 m/s detector array speed. See the text for analysis. 79
3.10 Sample of a source localization result. Red "x" denotes ground truth source position. Green dots denote detector array positions. The source was a 95 μCi Co-57 source at a 2.2 m source offset. Detector array speed was at 0.46 m/s, and the net count rate was taken after a 81 keV energy threshold was applied with a 1.00 s time integration. 81

3.11 Sample of a source localization result. Red "x" denotes ground truth source position. Green dots denote detector array positions. The source was a 113 μCi Cs-137 source at a 4.2 m source offset. Detector array speed was at 0.46 m/s, and the net count rate was taken after a 81 keV energy threshold was applied with a 1.00 s time integration. 82
3.12 Localization performance with respect to source offset using 30 s measurements. Results between 95 μCi Co-57 and 113 μCi Cs-137 source are compared. See the text for analysis. 83
3.13 Sample of a source localization result. Red "x" denotes ground truth source position. Green dots denote detector array positions. The source was a 113 μCi Cs-137 source with a 2.3 m source offset. Detector array speed was at 0.69 m/s, and the net count rate was taken after a 81 keV energy threshold was applied. (Left) A 0.20 s time integration was used. (Right) A 1.00 s time integration was used. See the text for analysis. 85
3.14 Localization performance with respect to source offset using 30s measurements, a 113 μCi Cs-137 source, and a 81 keV energy threshold. Results between 1.00 and 0.20 time integrations are compared. (Left) Detector array speed at 0.46 m/s. (Right) Detector array speed at 0.69 m/s. See the text for analysis. 86
3.15 Localization performance with respect to source offset using 30s measurements and a 113 μCi Cs-137 source. Results between 1.00 and 0.20 time integrations are compared with the detector array traveling at 0.46 m/s. (Left) The energy threshold was set to 81 keV. (Right) Only Cs-137 photopeak counts were included. See the text for analysis. 87
3.16 Sample of a source localization result. Red "x" denotes ground truth source position. Green dots denote detector array positions. The source was a 113 μCi Cs-137 source with a 4.2 m source offset, a 0.20 s integration time was used, and the net count rate was taken after a 81 keV energy threshold was applied. (Left) Detector array speed was 0.46 m/s. (Right) Detector array speed was 0.69 m/s. See associated text for analysis. 89

3.17 Localization performance with respect to source offset using 30s measurements. Results between 0.46 m/s and 0.69 m/s detector array speeds are compared. Source was a 113 μCi Cs-137 source with a 122 keV energy threshold and an integration time of 0.20 s. Refer to text for analysis. 90

3.18 Localization performance with respect to source offset using 30 s measurements. Source was a 113 μCi Cs-137 source and the detector array's speed was 0.46 m/s. (Left) Integration time of 1.0 s. (Right) Integration time of 0.20 s. See the text for analysis. 91

3.19 Localization performance with respect to kSigma. Measurement time was 30 s with an integration time set to 1.0 s. (Left) The energy threshold was set to 32 keV, where the entire energy spectrum is considered. (Right) Input type was photopeak counts, where fewer counts would be considered NORM, hence the higher kSigma. 93

4.1 WIND Backpack Detector Array. (Left) Concealed backpack configuration. (Right) Radiation detector array packaged within backpack. 96

4.2 Data fusion workflow overview. Red ellipses denote measured data, blue blocks denote algorithm modules, and blue ellipses denote output generated from algorithms. 99

4.3 (Measured angular response for a 113 μCi Cs-137 source at 172.4 cm. The polar angle represents source position in degrees, while the radius denotes magnitude of the net count rate (cps) after background subtraction and an 81 keV threshold is applied. 100

4.4 Directionality performance while trained with a 113.3 μCi Cs-137 source at 172.4 cm while observing a 113.3 μCi Cs-137 at 172.4 cm for the detector array used in this work. X-axis represents directionality estimates. Y-axis represents ground truth source angle. Color denotes probability of classification. Every pixel describes an angle spanning 5 degrees. See associated text for more detail. (Left) Directionality performance with an integration time of 0.2 s. (Right) Directionality performance with an integration time of 1.0 s. 101

4.5 Dynamic source localization experimental setup. 105
4.6 Source transfer scenario. (Top) DFM output at 17:51 where the experimentalist in the flannel shirt is carrying the 113 μCi Cs-137 source. (Middle) Fusion output at 17:54 where the experimentalist in orange now carries the source. (Bottom) Fusion output at 17:56. See the text for analysis. 109
4.7 Object occlusion scenario, where the true target is the furthest away. (Top) Fusion output at 17:56, before the occlusion event. The experimentalist in orange is carrying the 113 μCi Cs-137 source. (Middle) Fusion output at 18:05. (Bottom) Fusion output at 18:06, after the occlusion event. See the text for analysis. 110
4.8 Object occlusion scenario, where the true target is the closest person. (Top) Fusion output at 18:18, before the occlusion event. The experimentalist in orange is carrying the 113 μCi Cs-137 source. (Bottom) Fusion output at 18:24, after the occlusion event. See the text for analysis. 111
4.9 113 μCi Cs-137 directionality results. (Top) Radiation data only. (Bottom) Video and radiation data fused result. 114
4.10 95 μCi Co-57 directionality results. (Top) Radiation data only. (Bottom) Video and radiation data fused result. 115

1 (Top) Detector array configuration. (Bottom) Angular response (count rate in cps) with uncertainties of the detector array to a 25 μCi source placed 2m away. 129
2 Rotating stage setup. The detector array rotates at a fixed position and the source is in a fixed position. 130
3 (Top) GPS location of each measurement. Actual movement of the measurement platform was a straight line at a constant velocity. (Bottom) Count rate measured at each measurement interval every 0.1s. 131

4 (Top) GPS location of each aggregated measurement. The red dot denotes the location of the estimated Point of Closest Approach. (Bottom) Count rate after aggregating the raw measurements to an integration time of 1s. The red dot denotes the estimated Point of Closest Approach. The SNR for the PoCA location is also provided. 132
5 (Top) MLE result. White lines are the contours of the 2D Gaussian fit. The pixel color denotes the log probability value of the posterior. (Bottom) MLE result from Reference [25]. 134
6 MLEM Result. White lines are the contours of the 2D Gaussian fit. The pixel color denotes the log probability value of the posterior. 135
7 MCMC Result. 137
8 (Top) MLEM Result with the removal of angular response. (Bottom) MLEM Result with angular response information. Duplication of Figure 6 for the reader's convenience. (Both) White lines are the contours of the 2D Gaussian fit. The pixel color denotes the log probability value of the posterior. 138

Chapter 1

Introduction

1.1 Background

Source localization is the act of finding non-natural radiation sources in the environment. Non-natural radiation sources of particular interest are Special Nuclear Material (SNM) and industrial radioisotopes. SNM such as U-235 and Pu-239 can be used in the construction of an improvised nuclear device. Industrial radioisotopes such as Co-60 can be dispersed into the environment through a radiological dispersal device. Standoff Radiation Detectors (SRDs) are typically "used by law enforcement and emergency responder personnel to find lost, stolen, illegal, or potentially threatening radiological sources" [9].

1.2 Related Measurement Platforms in Previous Work

1.2.1 Commercially Off The Shelf Systems

There are a number of man-portable and vehicle-based measurement systems that could be used for source localization. The System Assessment and Validation for Emergency Responders (SAVER) was a program established by the Department of Homeland Security to inform procurement decisions for emergency responders. A portion of their scope was to perform market surveys for various radiation detection missions. Personal Radiation Detectors (PRDs) and Spectroscopic Personal Radiation Detectors (SPRDs) are devices with

small form factors used to "detect changes in the radiation level slightly above background with a fast response time to provide an alert for further investigation" [12]. PRDs and SPRDs tend to be "small, lightweight, and cheap" so they can be deployed to many responders to "detect and interdict the illicit movement of material that could be used in a radiological dispersal device or other radiological threat" [12]. Radionuclide Identification Devices (RIDs) "are instruments that identify the radionuclides present in a radioactive source by identifying these characteristic gamma-ray emission patterns" [11]. "SPRDs are limited in detection and radionuclide identification capabilities relative to RIDs," such that they are typically used to identify radioactive material after a detection[11]. However, the higher cost RIDs could be solely used in lieu of PRDs or SPRDs. Radiation detection backpacks are a subset of wearable detection systems designed for "executing covert searches of gamma-emitting (and in some cases neutron-emitting) radioactive materials" that "are especially useful in situations where radiation search surveys of large crowds or high-profile events are performed" [10]. Finally, Standoff Radiation Detectors (SRDs) are the largest, most expensive devices of the radiation detection missions which also tend to be the most sensitive and capable. They are typically used to "search for radioactive material from a certain standoff distance so that a wide area of coverage can be obtained" [9]. Table 1.1 summarizes the size and cost of various commercial off the shelf (COTS) equipment as a function of the radiation detection mission.

1.2.2 Imagers

The Coded Aperture Imager (CAI) (see Figure 1.1) uses a plane of radiation detectors and a patypssive plane of lead bars. The passive plane casts a shadow pattern upon the detector plane when a source is present, from which one can infer the source position. With this Large Area Imager (LAI), Ziock et al. was able to localize a 1 mCi Cs-137 source at a stand off distance of 46 m and a vehicle speed of 5 km/h (see Figure 1.1) [46]. The MISTI system is another example of a CAI where Huh et al. improve upon the source localization result of CAIs by incorporating system movement within the radiation transport model within the algorithm [20]. Note that the MISTI system has a 2D hit pattern as both the front passive lead layer and the radiation detector array have a 2D pattern. Despite the impressive inherent background discrimination and imaging capabilities of a CAI, sensitivity for such a system

Table 1.1: Summary of Commercial Off The Shelf (COTS) equipment for radiation detection applications from SAVER market surveys. Items denoted with "*" denotes that this system can be made man-portable

Detector	Mission	System Weight (lb)	Mass of Active Detector Material (lb)	Approximate Cost ($)	References
Passport G300*	SPRD	0.55	0.04	8,000	[12, 32]
FLIR IdentiFINDER R400*	RID	3.2	0.2	20,000	[11, 14]
STE Inc. RadPack*	Backpack	14	0.3	35,000	[10, 39]
ORTEC Detective EX-100T*	RID	15.2	0.1	95,000	[11, 31]
Bubble Tech FlexSpec Mobile	SUV Based SRD	550	70	200,000	[9, 6]
FLIR iFind Compton Camera	Trailer Based SRD	2,000	N/A	900,000	[9]

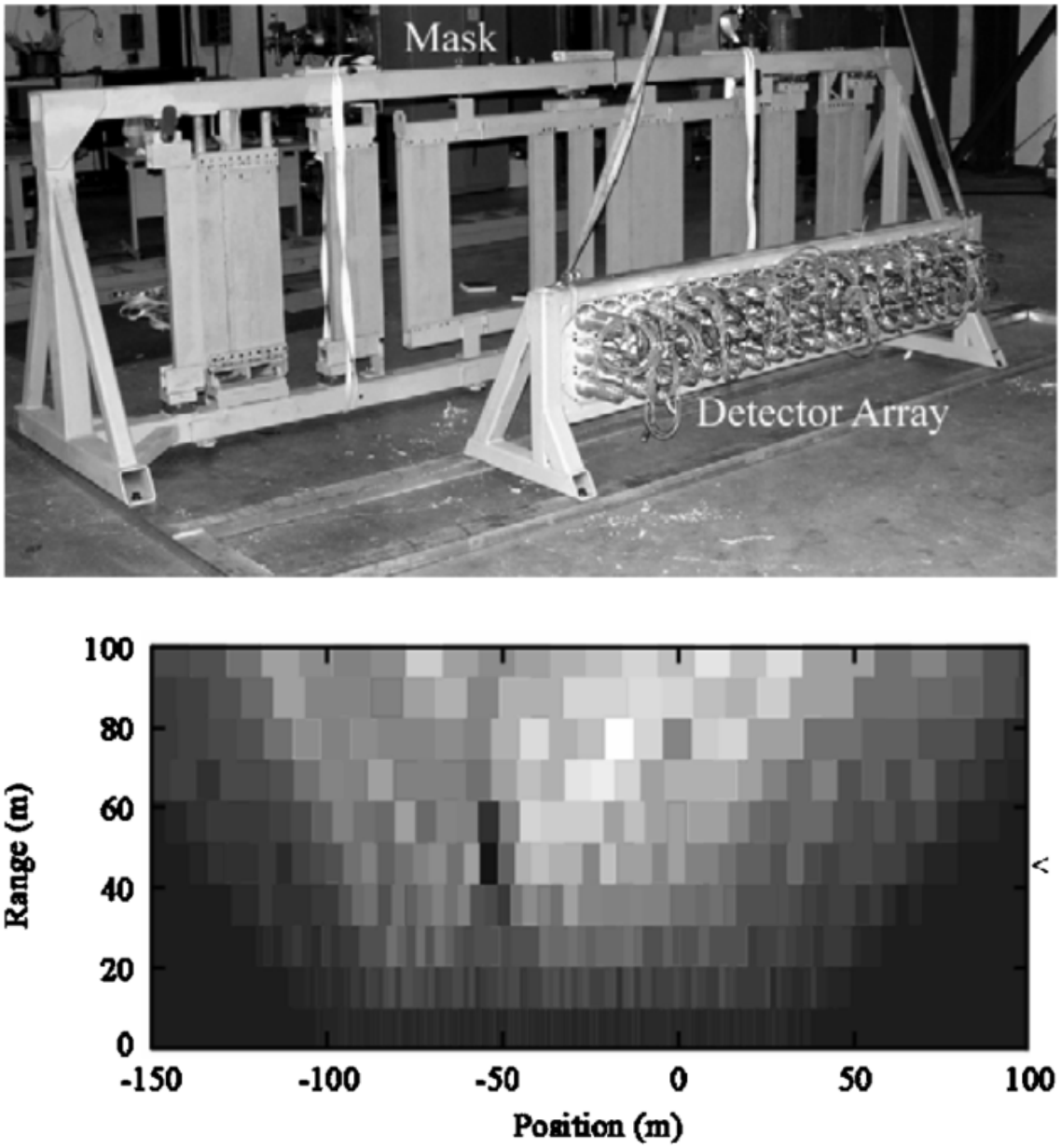


Figure 1.1: Source localization using the LAI array using CAI. (Left) Picture of the LAI. (Right) Source localization result which represents a top-down view of the world. Both images from [46]

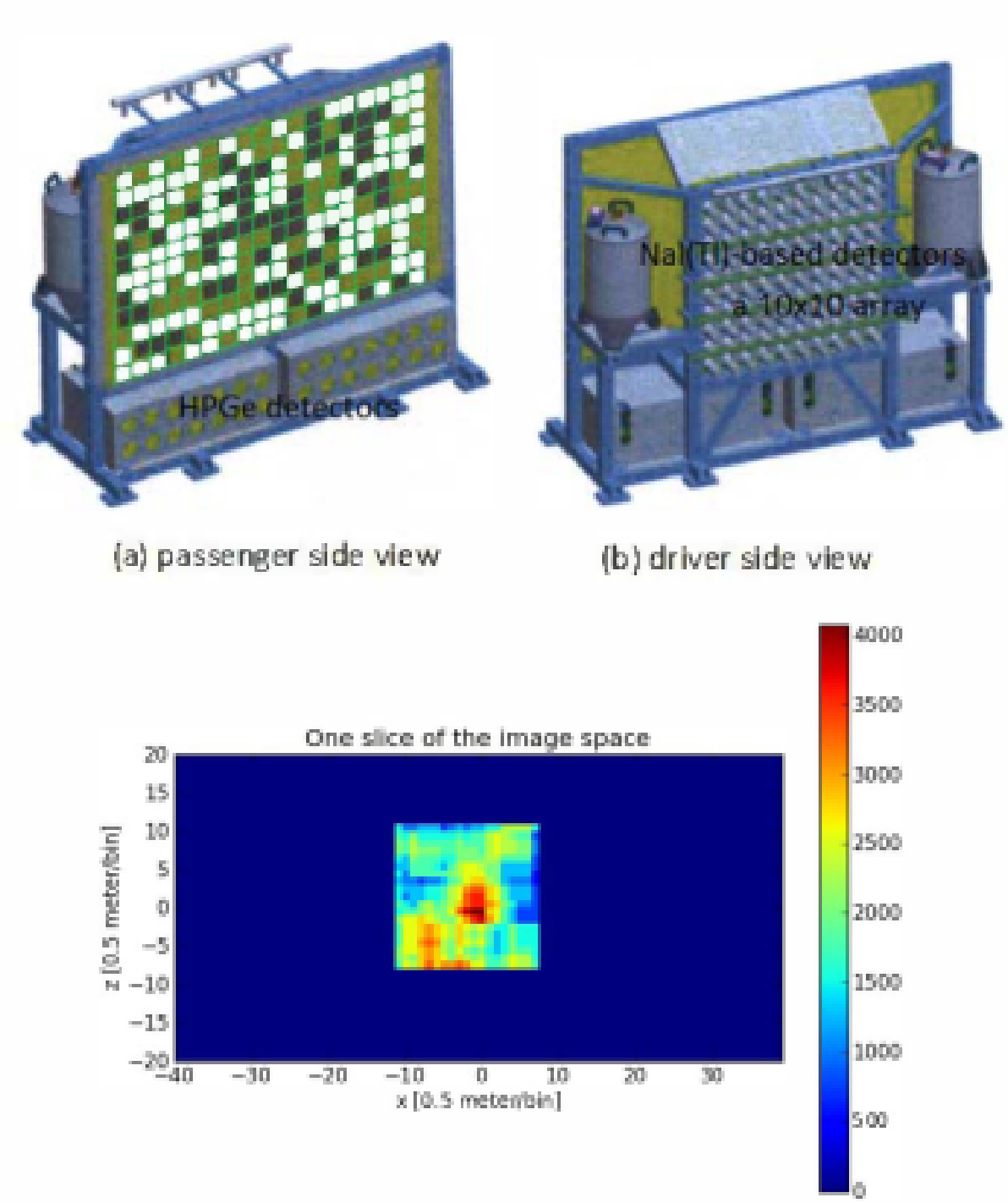


Figure 1.2: Source localization using the MISTI system using CAI. (Left) Picture of the MISTI system. (Right) Source localization result which represents a slice of a three-dimensional view of the world. Both images from [20].

degrades as 50% of energy deposition events are discarded through interactions with the passive mask layer.

It also worth noting Compton Imagers (CIs), such as the Polaris H imaging spectrometer [42] which comes in a portable form factor, can also be used for source localization. CIs employ Compton scattering, where an incident gamma photon fully deposits its energy at two locations. With knowledge of the energy deposited and the position at those locations, the incident gamma photon direction can be inferred: two procedures for inference include Filtered Backprojection [16] and Maximum Likelihood [26]. The trade-off which CI techniques is it requires both incident gamma energy to be high enough such that Compton scattering events occur often enough and that the detection of two partial energy depositions which sum to the incident gamma energy occur often enough. Consequently, CIs can be challenging to localize SNM or industrial sources with lower gamma energy signatures such as Am-241; this is a scenario where CAIs would excel.

1.2.3 Detector Arrays

The Mobile Urban Radiation Search (MURS) is an Sports Utility Vehicle (SUV) based platform intended to be used for source localization [7]. It consists of 6 Sodium Iodide (NaI) detectors in a close array, creating unique angular responses which aid in source localization (see Figure 1.4). This particular platform can be used as a static or dynamic measurements depending on the operational scenario, especially designed for radiation source localization.

The localization performance of a Helicopter-based, Stand-Off Radiation Detection System (HeliSORDS) detector array was studied in great detail [25, 23, 35, 29, 34]. This measurement platform contains two pods with 46 Cesium Iodide (CsI) scintillators each in the configuration shown in the left of Figure 1.6. Utilizing the high fidelity simulations and measurements shown to the right of Figure 1.6, it was demonstrated with synthetic data that a point source could be localized from a single pass of some operational area in both References [29] and [34].

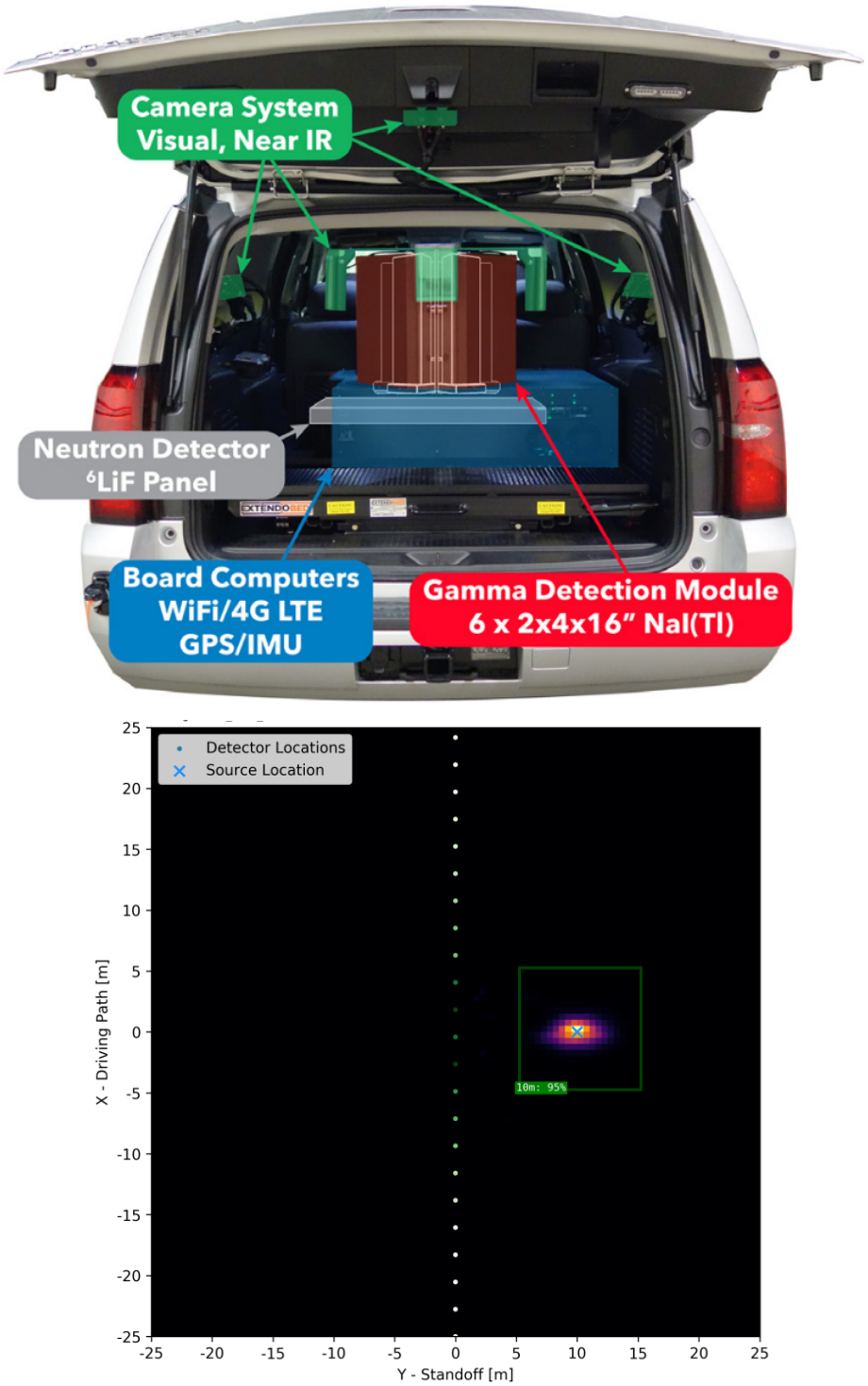


Figure 1.3: (Top) MURS measurement platform. This is a SUV-borne system. (Bottom) MLEM Result on simulated data.

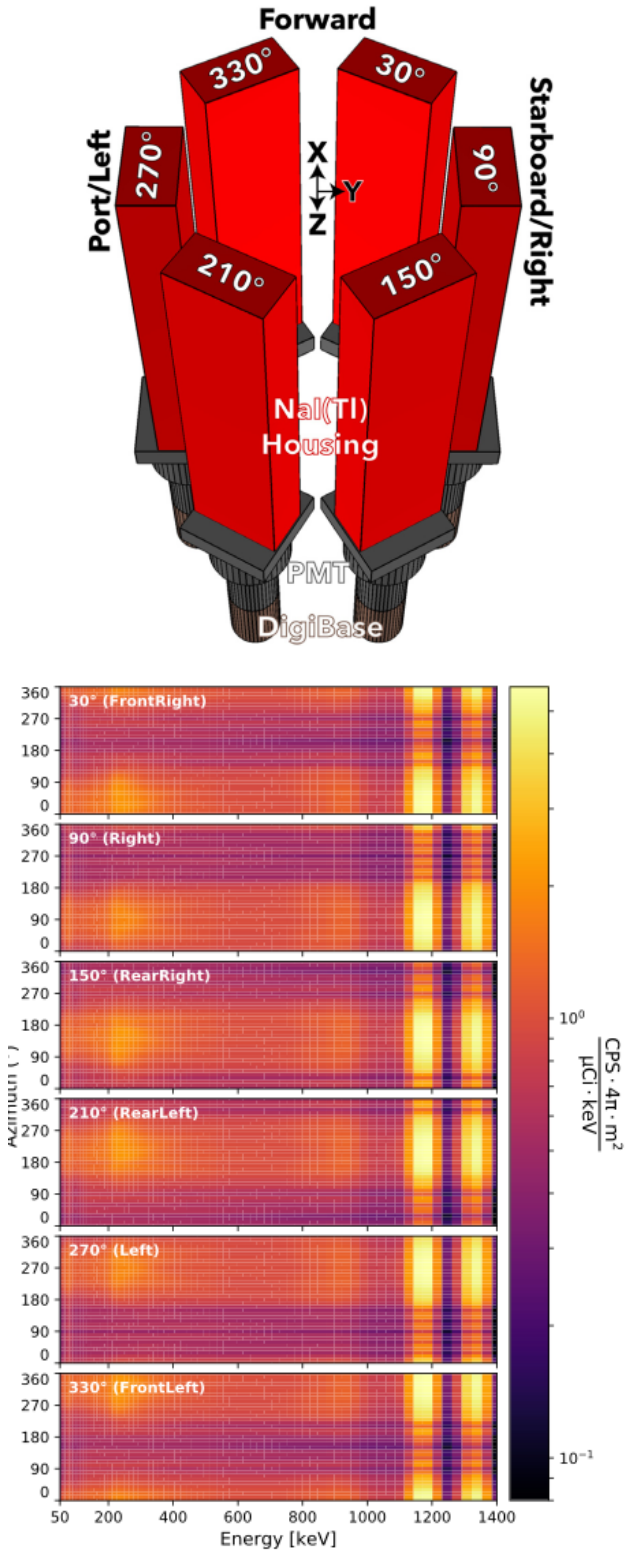


Figure 1.4: (Top) MURS detector array configuration. (Bottom) Angular response (energy spectra) of the MURS detector array due to a Co-60 source placed 2m away at chosen angles. Both images are from Reference [7].

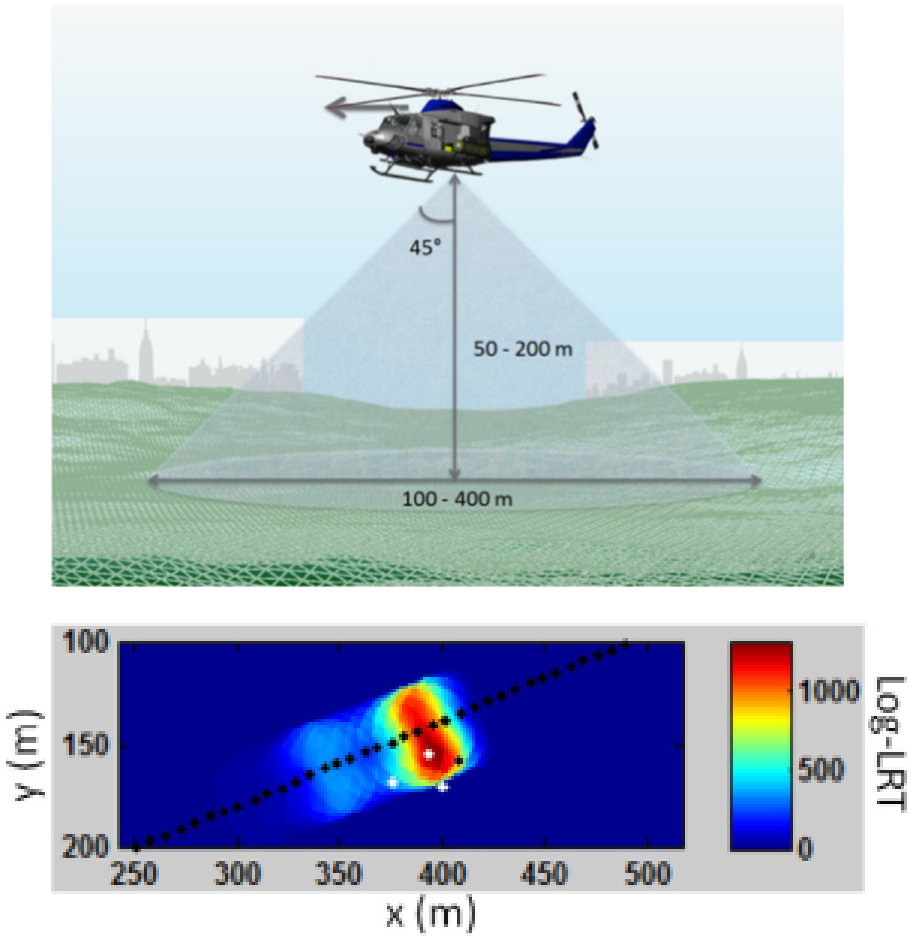


Figure 1.5: (Top) Airborne Radiological Enhanced-sensor System (ARES), also known as the Helicopter-based Stand-Off Radiation Detection System (HeliSORDS), with typical flight parameters from Reference [29]. (Bottom) Probability map generated using Maximum Likelihood Estimation from Reference [25].

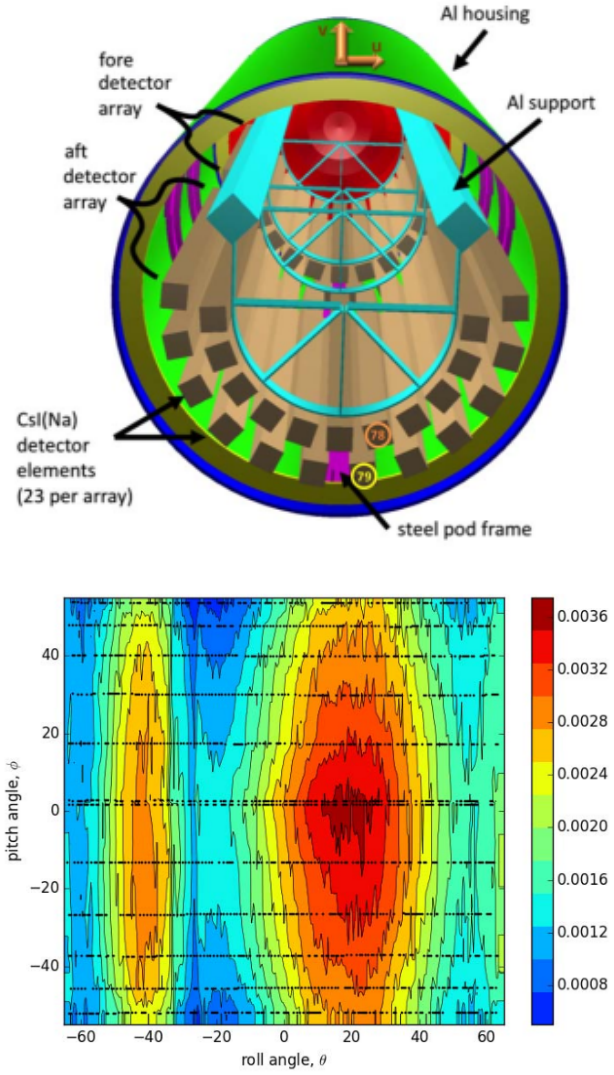


Figure 1.6: (Top) HeliSORDS CsI array geometry. (Bottom) Angular response (normalized count rates) heat map for one of the detectors in the array. Both figures from Reference [23].

1.3 Source Localization Approaches

Source localization, also known as imaging or reconstruction, can be separated into 3 distinct components: the inputs, the radiation transport model to generate an expectation for the inputs, and a method to compare the expectation to the measurement. The inputs denote some radiation signature that can be measured, such as the number of radiation events in some time period (gross counts). The radiation transport model describes how the presence of a source at some location would affect the inputs, such as the full Monte Carlo (MC) radiation transport from a given location to the detector. Finally, the comparison method is some procedure that quantifies how well the measurement matches the expectation.

Proximity imaging uses variable integration periods (measurement times) as well as detector movement to calculate source localization results. Aucott et al. started with the definition of signal-to-noise (SNR) ratio, where the signal consists of counts contributed from a radiation source while the homogeneous background is considered a constant rate. The first derivative is taken to find the integration window that yields the highest SNR: an integration window spanning of 108^o according to Reference 1. This result was significant because this integration window is independent of detector speed, background contribution, or source strength. As long as the integration period reflects a pass spanning a total angle change of 108^o, the source strength calculated would have the least amount of uncertainty. The top of Figure 1.7 describes a typical measurement taken with the CAI platform in Aucott et al's framework, while the bottom of Figure 1.7 shows a source localization result describing the SNR of each potential source location.

Adaptively Reevaluated Bayesian Localization (ARBL), developed by Miller et al., has applied Maximum Likelihood Estimation (MLE) to measurements from a helicopter borne system to localize a source in a given patch of land below a system [29]. This work explored the effects of using three different inputs: 1) summing all measured counts across all 92 detectors (this option removes all angular response information), 2) summing measured counts every four detectors, and 3) using measured counts in each detector. The radiation transport in their approach accounted for the photon contributions to the measured counts directly from the source, indirectly from the photons scattered off the ground from the

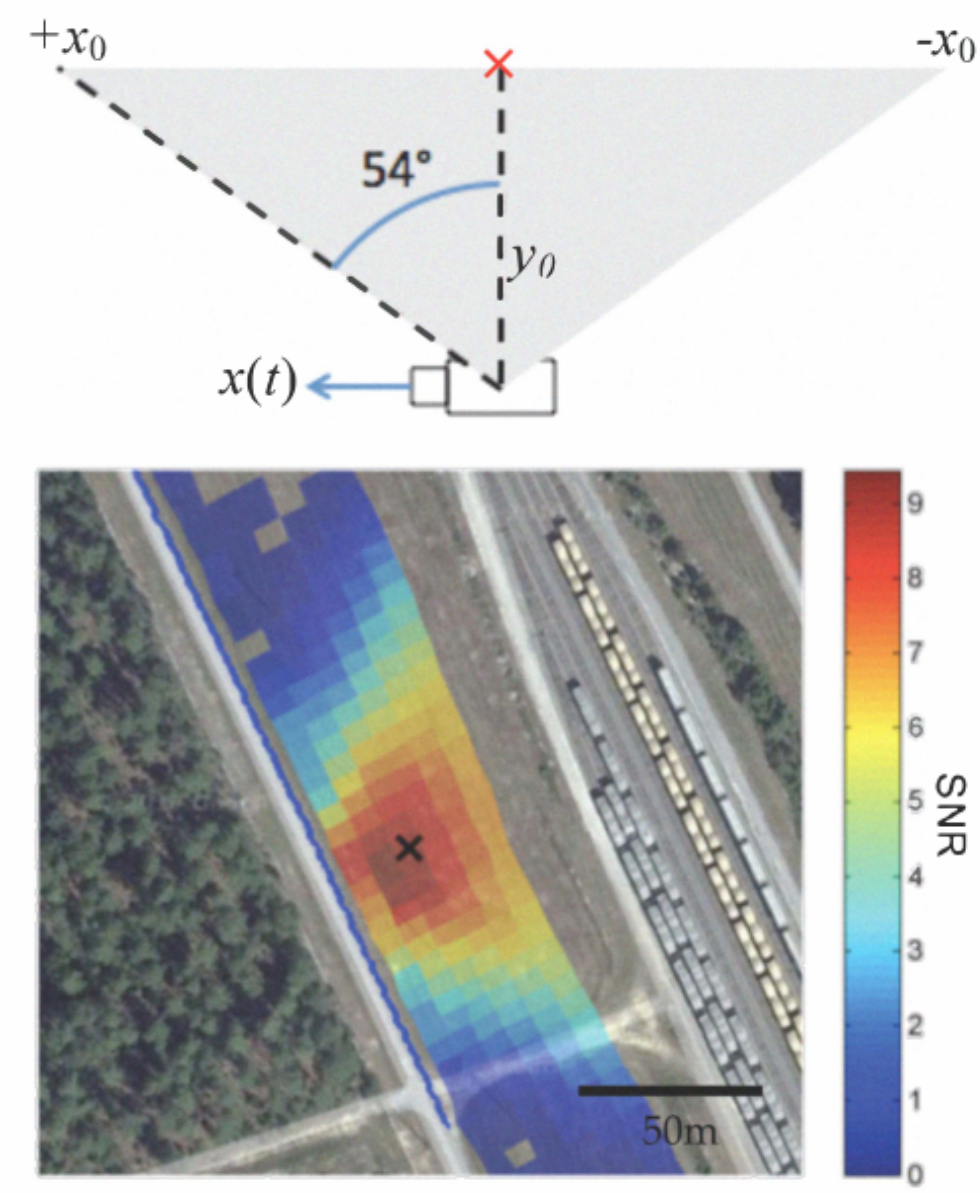


Figure 1.7: (Top) Source localization experiment. A detector system in a truck is driven past a potential source location denoted by the red 'x'. The optimal integration window is the time it takes to travel from -x_0 to x_0, spanning 108^o in front of the source. (Bottom) Source localization map denoting the SNR with respect to position. This was generated with measured data. The source is a 200 μCi I-131 located at the black 'x'. From Reference [1].

source, and finally, air scattering from the ground or source into the array. Comparison was performed using MLE. This comparison method aggregates a collection of measurements, discretizes possible source locations below the ARES platform. This approach ultimately generates a two-dimensional source existence probabibility of the search space below, where the source position with the highest value is where the point source is most likely located: the source position estimate. Figure 1.8 showcases source localization estimates for 10 samples of radiation measurements for each measurement type (All, Fours, Each). Note the variability on the localization estimates.

Miller et al. thoroughly explored the localization performance of ARBL on synthetic runs, where sampled synthetic radiation data is used to characterize both the mean and variance of the localization estimate's error as a function of source offset to the flight path and radiation measurement used. Figure 1.8 showcases source localization estimates for 10 samples of radiation measurements for each measurement type (All, Fours, Each). Note the variability on the localization estimates. Figure 1.9 characterizes the source localization estimates with respect to localization error and source strength for different measurement scenarios. Essentially, Figure 1.9 is a summary of the source position estimates given in Figure 1.8.

On the same measurement platform as ARBL, MLEM has also been used for source localization by Penny et al. [34]. They use spectroscopic radiation measurements as their inputs. They use one-dimensional radiation transport, where only the photons emanating directly from the source to the detector array are accounted. Finally, they use MLEM to discretize the search space and generate a map describing each position's contribution to the measurement. Figure 1.10 shows the ground truth source distributions in 1) and 2), as well as the estimated source distributions in 3) and 4). They were able to demonstrate accurate reconstruction of both the background and source pixels in their synthetic dataset. An important feature of MLEM is that it generates a source activity or source strength map: MLEM does not assume there is 1 source like MLE, but it assumes that every potential source location (read pixel) is a source. Hence, MLEM tends to be the favored solution for localizing distributed sources or when the number of sources present are unknown. Ultimately, the key result from Reference 34 was the ability to reconstruct both the background and source

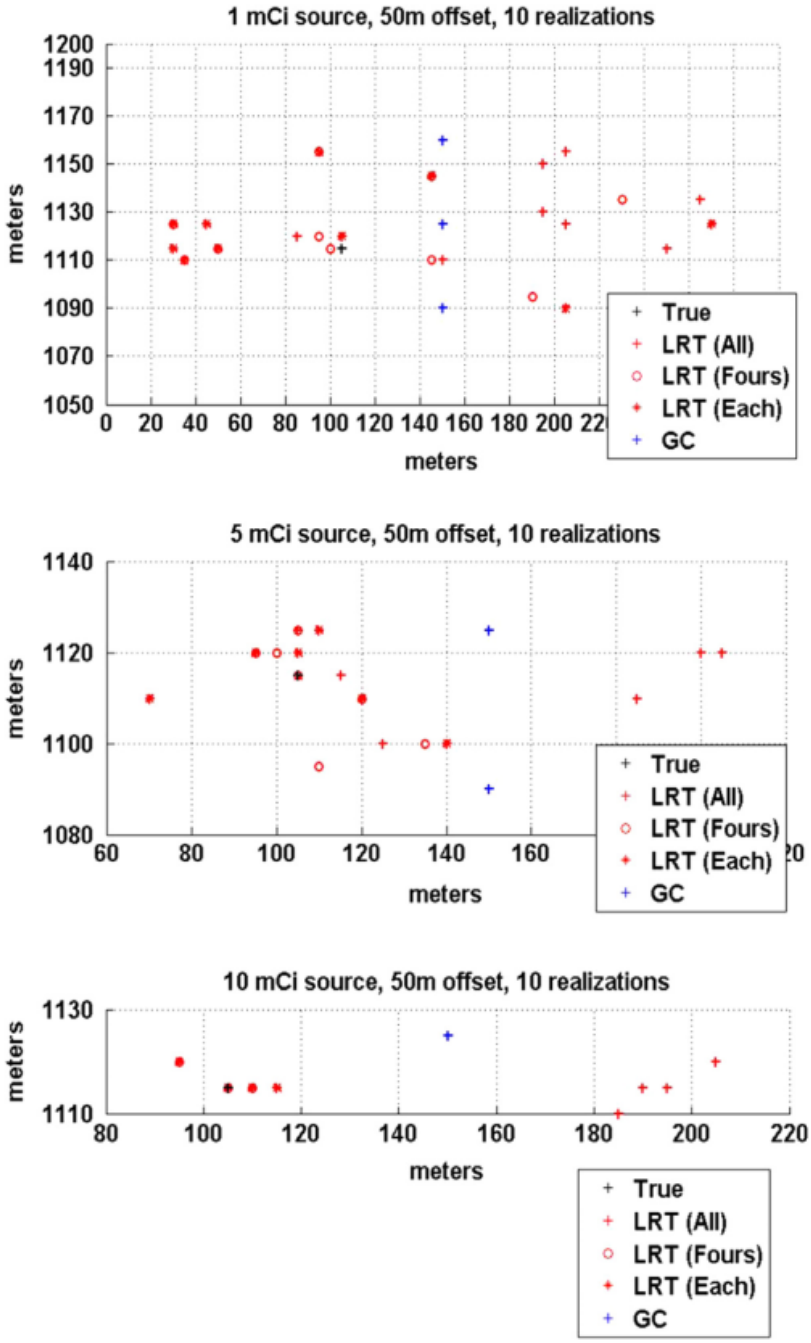


Figure 1.8: Source localization results on synthetic data describing a helicopter flying 70 knots in a straight line at an altitude of 83 m. (Top 3) Source localization estimates for each run. 10 runs were done for each input type. (Bottom) Error distribution with respect to source strength for different source offsets and input data types. From Reference [29].

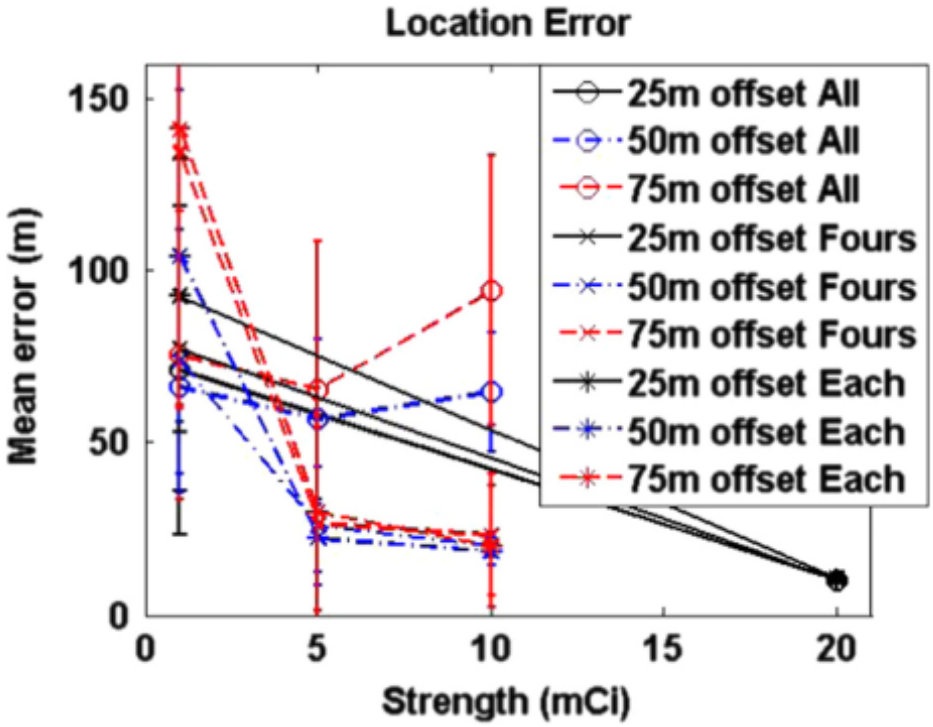


Figure 1.9: Source localization results on synthetic data describing a helicopter flying 70 knots in a straight line at an altitude of 83 m. Error distribution with respect to source strength for different source offsets and input data types. From Reference [29].

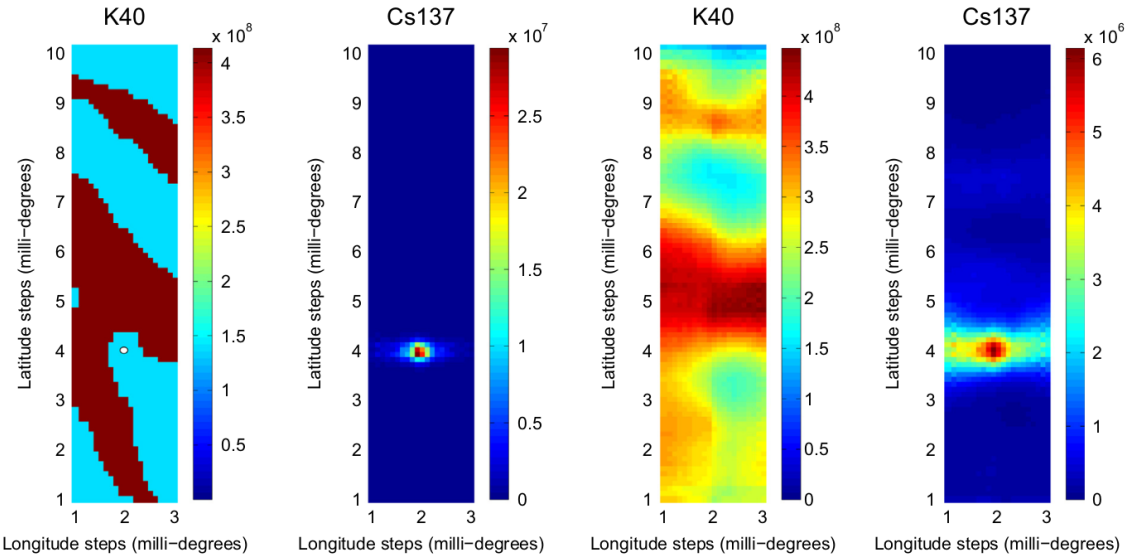


Figure 1.10: Source localization results where the color of each pixel denotes source strength. From left to right. 1) Ground truth K40 (background NORM) activity distribution. 2) Ground truth Cs-137 activity distribution. 3) Reconstructed K40 activity distribution. 4) Reconstructed Cs137 activity distribution. From Reference [34].

activity distributions to generate their source localization result; however, that work did not characterize localization performance in terms of the source localization error.

For completeness, a microcosm is shown for source localization in the context of radiation sensor networks where multiple static sensors are used to infer the location of a static source. Deb et al. studied localization performance using measured counts as the inputs, one-dimensional radiation transport as the expectation model, and either MLE and MLEM as the comparison method [8]. Their key result was the ability to calculate the source localization error with respect to measurement time for arbitrary sensor configuration using their synthetic test bed. More recently, Hite et al. characterized a sensor network's localization performance using measured data and a different comparison approach in Reference 19. Gross count measurements were collected with a sensor network consisting of 12 NaI(Tl) detectors of 2" $\times$ 4" $\times$ 16" dimension. Using Markov Chain Monte Carlo to compare the expectation to the measurement and one-dimensional radiation transport to calculate the expectation, they were able to compute the localization error for a 37 mCi Cs-137 source as a function of measurement time. Using 30 minutes of data across 12 detectors, the source localization L2 error (euclidean distance) in their single experiment was found to be on the order of 2 m: an impressive result considering their area of operation spanned a cluttered 200 $\times$ 100 m field.

1.3.1 Source Directionality Approaches

Directionality is the act of determining the source direction relative to a given radiation measurement system in short time scales, such as 1s. Vilim et al. introduced the idea of directionality by performing source localization with a detector array consisting of 4 NaI(Tl) in a closely packed configuration [41]. They showed with their measurements that using a directional detector system (closely-packed detector array) and a single measurement position, the source position estimates can be best interpreted as a direction relative to the system itself, i.e. the source is most likely positioned at unknown distance at 90^o (see left of Figure 1.11). However, when using the measurements from two directional detector systems,

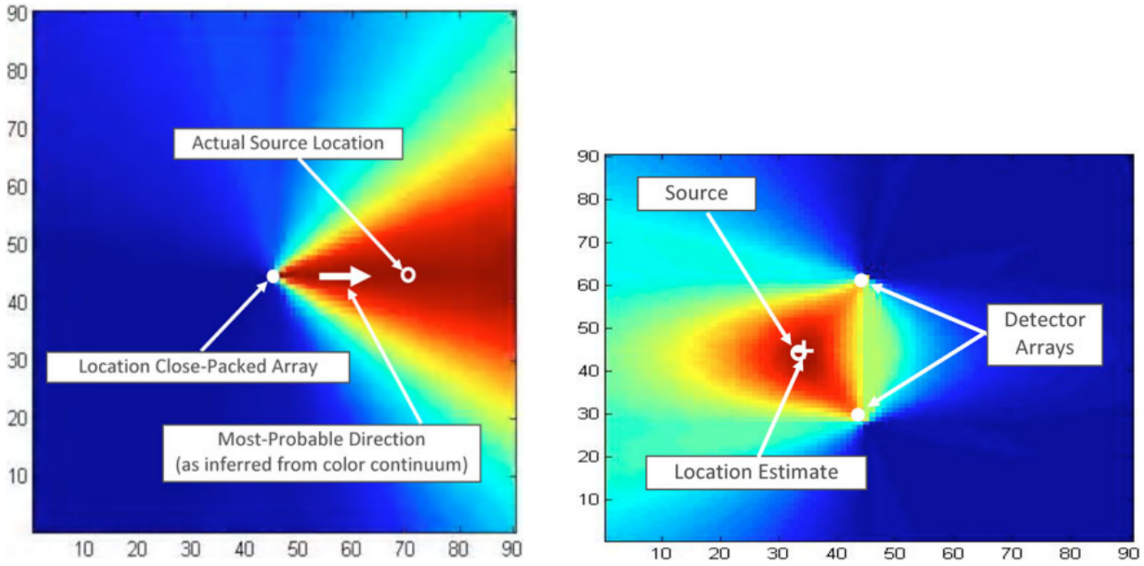


Figure 1.11: Source localization results from Reference [41]. (Left) Source localization result using measurements from a single detector array at a fixed position. Scenario is a 750 μCi Co-60 source at a distance of 762 cm away from the array. As shown, this localization result can be interpreted as directionality: source direction estimates relative to the system. (Right) Source localization result using measurements from two detector arrays at 2 different locations. The two detector arrays were placed 914.4 cm away from each other. The 750 μCi Co-60 was placed 304.8 cm perpendicularly away from the halfway point between the detector arrays.

the two direction estimates combine into a source position estimate, i.e. the source is most likely posited at x=35 and y=45 (see right of Figure 1.11).

Like Compton Imaging, directionality on detector arrays has been demonstrated using the Compton scattering signature. Gueorguiev et al demonstrated this idea using two 2" $\times$ 4" $\times$ 16" NaI(Tl) scintillators, where the mean energy difference in each detector is a function of incident source angle [15]. The mean energy difference refers to how higher energy gamma rays tend to have a forward scattering bias when undergoing Compton scattering, as thoroughly described by the Klein-Nishina cross section. Figure 1.12 showcases the exploited signature, where the difference in mean deposited energy between the detectors yields source directionality. This method was extended for several detector arrays of arbitrary geometry and arbitrary number of detectors in Reference [30], where covariance gamma-ray spectroscopy is used to exploit this mean energy difference signature. Note that the use of Compton scattering requires coincidence events, which share the same drawbacks as Compton Imagers.

Willis et al. takes a different approach to directionality by using the angular response as defined by the count rates in Reference [44]. They used Fuzzy logic to determine the sources direction using a simulated templates of a NaI(Tl) array composed of four 2" x 2" x 4" detectors. With this approach, the claim is the directional uncertainty is at most $\pm 10.4^o$ for this geometry attempting to ascertain the direction of a 5.4μCi Cs-137 source 18" away from the center of the array with a 1s measurement time.

1.3.2 The Role of Data Fusion

Real time source tracking was a concept introduced by Vilim et al. in Reference [41] (see Figure 1.14). The intention of their work was to use multiple detector arrays cooperatively to give intersecting directionality estimates using short measurement times, as shown in Figure 1.14. The directionality estimates from each detector array would update at each time step in order to capture source movement. The challenge is to get directionality estimates in very short measurement times in order to capture the source's motion, which is what Deb et al was investigated in the context of venue defense with a static sensor network.

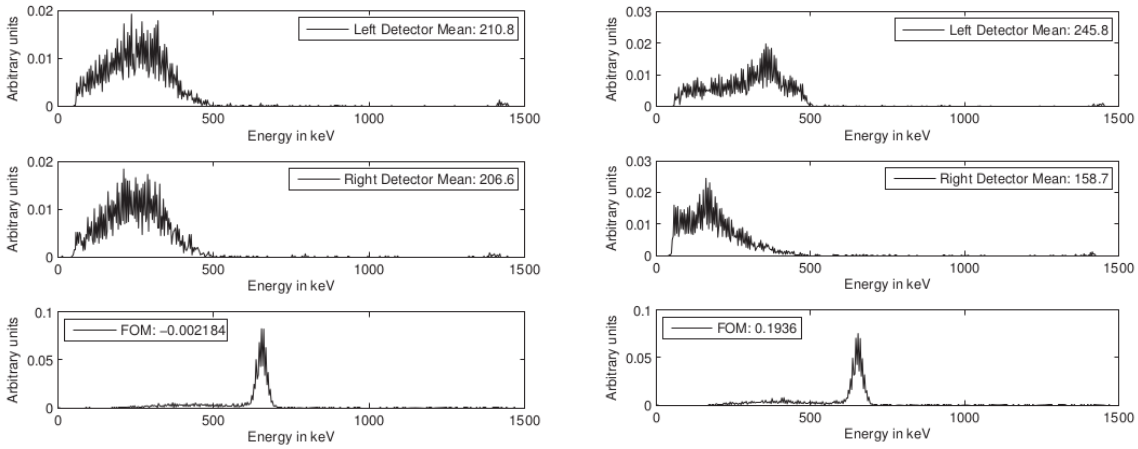


Figure 1.12: Compton scattering distributions as a function of Cs-137 source position. Each plot represents the energy spectra measured for coincidence events. The left column of plots is when the source is placed at 90^o. The right column of plots is when the source is placed at 45^o. (Top left) Energy spectrum from the left detector. (Middle left) Energy spectrum from the right detector. (Bottom left) Summed energy spectrum from both detectors. (Top right) Energy spectrum from the left detector. (Middle right) Energy spectrum from the right detector. (Bottom right) Summed energy spectrum from both detectors. All plots from Reference [15].

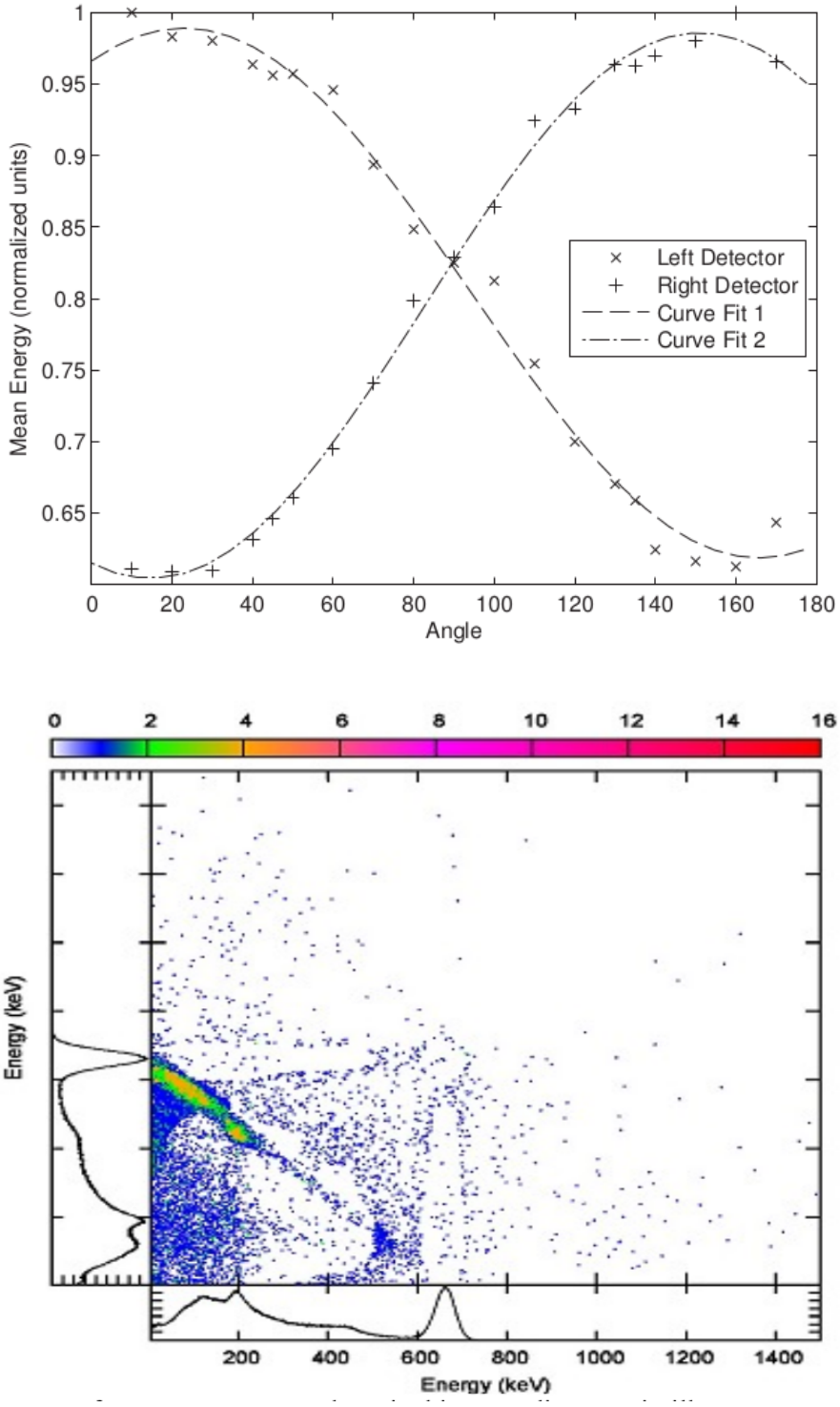


Figure 1.13: (Top) Mean energy difference signature from Reference [15]. (Bottom) Energy spectra covariance between two detectors for coincident events from Reference [30].

Deb et al characterized localization performance as a function of measurement time for a variety of localization algorithms, different sensor network configurations, and different source assumptions using a synthetic test bed (see Figure 1.15. More recently, Hite et al investigated source localization performance of a sensor network consisting of 12 2" × 4" × 16" NaI(Tl) detectors with respect to included measurement time on measured data. Significantly, Hite et al included not only the mean localization error but the uncertainty in their results [19] (see Figure 1.16). The underlying theme in these source localization works is the use of a sensor network and studying localization performance over time, where real time source tracking requires short measurement times to correctly capture source motion.

Radiation data has been fused with contextual information from other data modalities to improve source localization results. Barnowski et al. demonstrated that source localization results could be improved by fusing CI results with point cloud data from LIDAR sensors [3]. This was an early work of scene data fusion where contextual information improved source localization by constraining the radiation transport to detected surfaces from the point cloud data stream, which required the source to be stationary. Note how in Figure 1.17 that the degenerate solutions in the radiation only results are removed when the pointcloud data is included. Another example was Ziock et al. [45] where a CAI was used in conjunction with a contextual sensor suite, consisting of a gyroscope, GPS, and camera, to help determine where a radiation source would be located on a suspected small vessel. The contextual sensors accounted for the relative movement during the measurement period between the detector's boat and the suspected small vessel such that a source localization result could be computed in a 3-dimensional, target centered, coordinate system.

Fusion of radiation with other data modalities has been proposed in the literature for the localization of moving sources. Marshall et al. [28] use computer vision approaches to automatically detect objects via an RGB camera or LIDAR, track its distance history from a stereoscopic camera, then correlate the measured counts collected with a 2" × 4" × 16" NaI(Tl) detector to improve detection sensitivity. Henderson et al. [17] have developed a similar approach in parallel by correlating the radiation measurements from EJ-309 detectors with a potential target's distance history acquired from either a RGB camera, thermal camera, or LIDAR sensor. Both References 28 and 17 fundamentally use the one

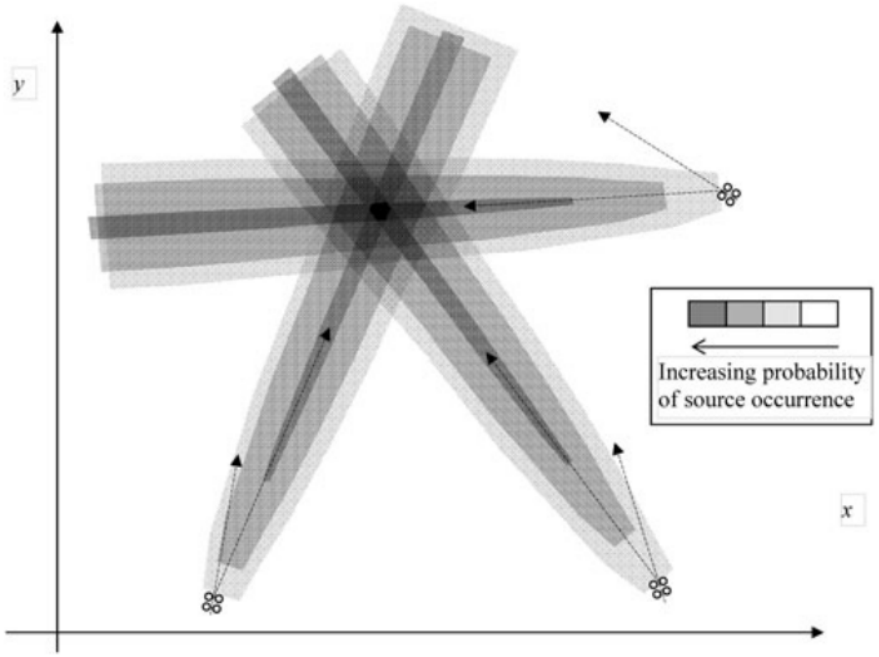


Figure 1.14: Real-time source tracking concept introduced by Reference [41]. Multiple detector arrays with directionality estimates tracking and pursuing the lone source carrier.

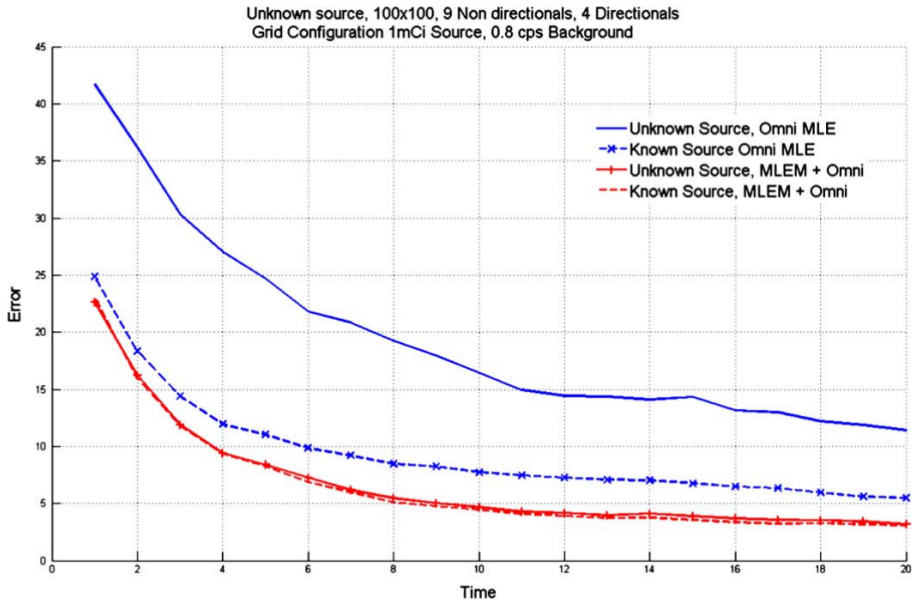


Figure 1.15: Localization error as a function of measurement time. Different localization algorithms were used: Maximum Likelihood Estimation (MLE) and Maximum Likelihood Expectation Maximization (MLEM). Omni refers to the use of non-directional radiation detectors. Plot from Reference [8].

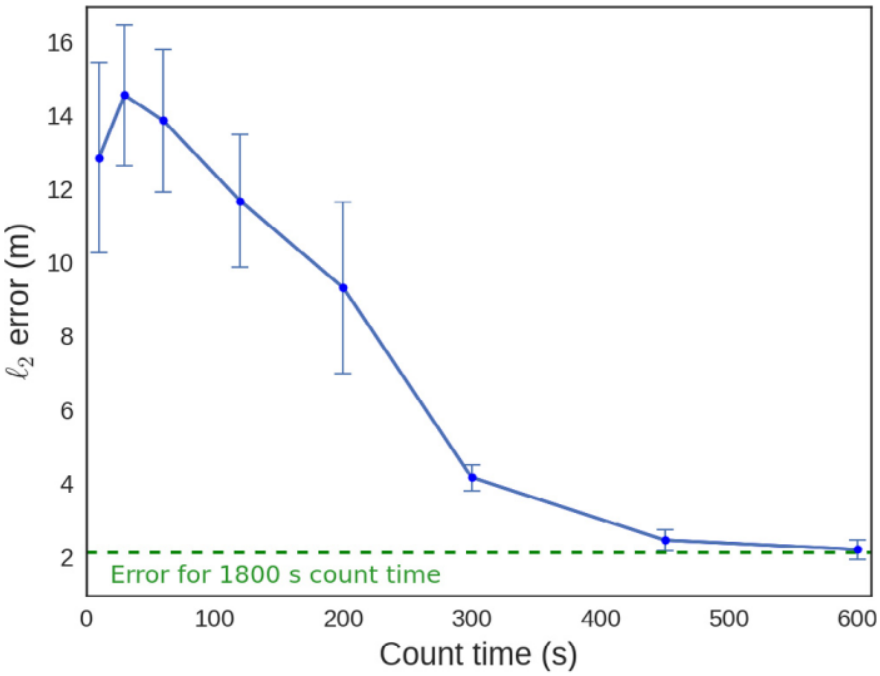


Figure 1.16: Source localization performance with respect to included measurement time for a sensor network from Reference [19].

over the square distance between the radiation source and detector to determine whether or not a tracked target carries the source. This work also shows the capability to account for complex, arbitrary object-source movement, where the object's view can be blocked by another object and the object can follow a path other than a straight line path or fixed distance rotation as also considered in Reference 17.

More recent data fusion approaches attempt to track radiation sources in motion or attribute sources to tracked objects. These approaches use a single detector system with the aid of contextual sensors. Marshall et al. demonstrated that computer vision methods could be combined with the count rate from a single 2" × 4" × 16" NaI(Tl) to automatically assign source strengths to detected objects within a video sequence [28] (see Figure 1.18. Henderson et al. demonstrated that object tracks measured by a thermal camera, RGB camera, or LIDAR sensor could be successfully correlated with radiation count rate information acquired by a sensor network of at least one detector to determine the most likely source carriers [17] (see Figure 1.19. Note how the experimentalist distance correlates well with the radiological measurements in the right plot. Both References [28] and [17] exploit the measured count rates relationship of one over the distance squared between the source and detector to execute their respective goals.

1.4 Dissertation Contributions

1.4.1 WIND Backpack Detector Array

The University of Tennessee WIND team has designed a backpack detector array for the source search scenario in simulation space. Ideally, this system will have the characteristics laid out in Table 1.2. Some of these characteristics make assumptions on what algorithms are to be employed on the platform. For example, it is assumed that the 1462 keV photopeak from Potassium-40 (K40) will be used for gain stabilization; however, an internal calibration source to the system can also be used for the same purposes. Much more detail on these choices and criteria can be found in Reference [2].

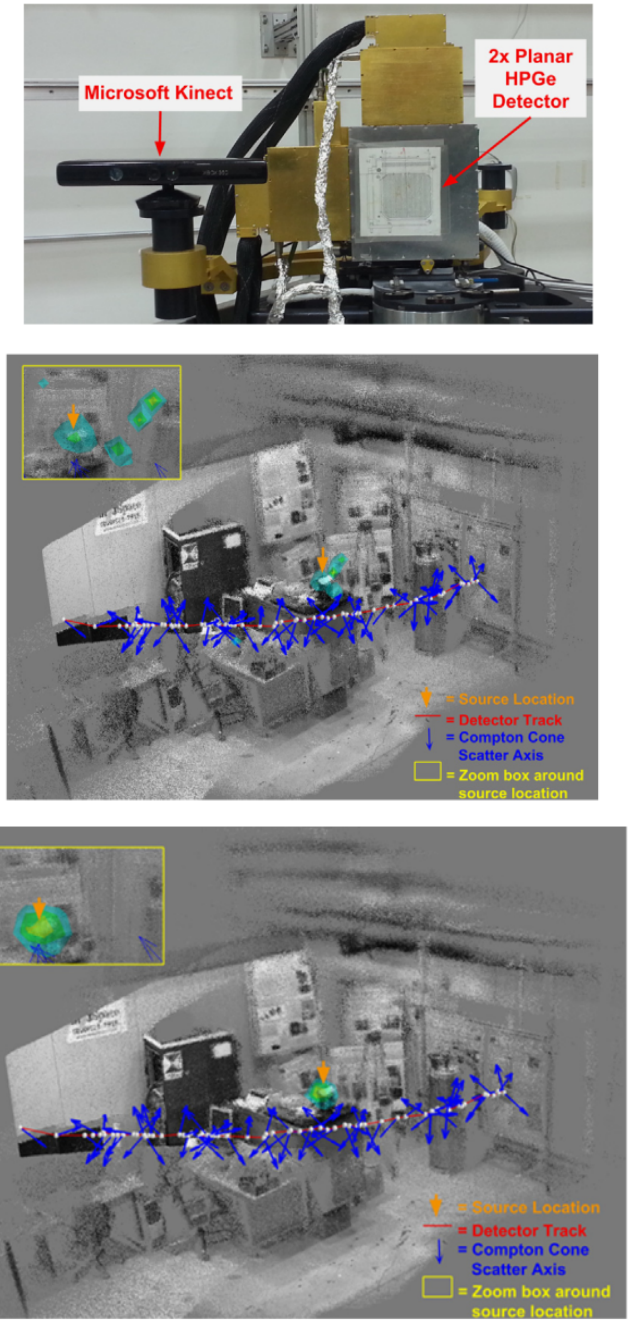


Figure 1.17: Scene Data Fusion concept. Source localization using a CI coupled to a Microsoft Kinect. (Top) Detector system. (Middle) Source localization result, radiation data only. (Bottom) Source localization result, fused data. Figures from Reference [3]



Figure 1.18: Data fusion between video RGB data and count rate data from a 2" × 4" × 16" NaI(Tl). Source strengths are attributed automatically to detected objects given their movement history. Figure from [28].

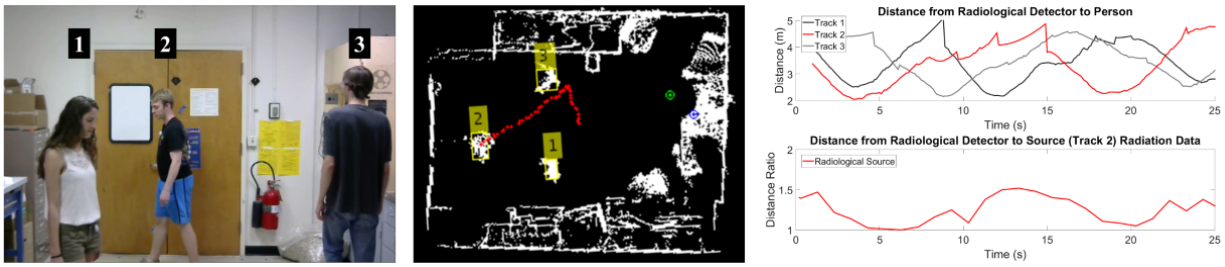


Figure 1.19: Data fusion between LIDAR pointcloud data and count rate data from a EJ-309. Source is a 131 μCi Cf-252. (Left) RGB camera footage. Not used in the calculation. (Middle) LIDAR pointcloud of the scene, top down view. (Right) Distance to each person above the plot of the radiation data. Figures from [17].

Table 1.2: Ideal characteristics for backpack detector array design

Characteristic	**Purpose**	**Simulation Metric**
Easy source detection	High sensitivity to sources of interest	Max. Total counts
Easy source identification	Make informed decisions on detected source	Max. peak to total ratio
Easy gain stabilization	Data consistency	Max. 1462 keV photopeak fitting
Easy source localization	Find sources quickly once detected to take action	Minimize directionality error

A trade-off analysis done in simulation space (Reference [2]) guided the design iteration, which have manifested in the built WIND Backpack detector array. A picture of the array can be seen in Figure 1.20. This array is a modular system where the detectors can be swapped. Currently, the system consists of 3 Scionix NaI(Tl) detectors 54 × 54 × 152 mm in dimension packaged with Silicon Photomultipliers. The signals from the anodes are directly processed by a CAEN DT5725 digitizer. This backpack also includes a VectorNav VN-300 GPS device, a Spedal 1080p webcam, and a laptop for data collection. This system is powered by a 54,000 mAh battery. Total mass of just the detectors is 4.9 kg, and the entire system weight is 16.6 kg. Note that the detector array frame and laptop comprises of 37% of the total backpack mass. This system is meant to be modular in nature, and throughout this dissertation, one of the NaI(Tl) detectors is substituted for 2 CLYC 54 × 54 × 76 mm coupled to BICRON PhotoMultiplier Tubes (PMTs).

This work explored the capabilities of a backpack-sized wearable radiation detector array. This form factor is of particular interest as it is a compromise between RIDs and SRDs with respect to cost, performance, and complexity. The results showcased intend to provide guidance in operation of similar systems for law enforcement and emergency responders, as well as inform the design of future iterations.

1.4.2 Agnostic Method Development for Detector Arrays

This dissertation developed a strategy to localize a radiation source in motion by exploiting the angular response inherent in closely packed detector arrays. Using only radiation data, one can pursue moving radiation sources using the radiation directionality method presented in Chapter 2. However, the ultimate goal was to demonstrate that source carrier probabilities could be assigned to tracked targets in an automated fashion by fusing both radiation and video data modalities. This strategy consisted of 3 components: radiation directionality, object directionality, and data fusion. In radiation directionality, methods were developed using net count rates from each detector to generate source direction estimates using short, periodic measurements. In object directionality, the context of object positions from the RGB video data stream are automatically detected and tracked. Finally, data fusion involves



Figure 1.20: Built WIND Backpack detector array.

the combination of both the radiation directionality and object directionality components to correlate tracked object histories with the radiation data.

The structure of this dissertation is as follows. Details of the measurement of an array's angular response and its exploitation radiation directionality is given in Chapter 2, which has been published in Reference [5]. The source localization capabilities of the WIND Backpack detector array on a static source is given in Chapter 3, which gave an understanding of what could be done using only radiation data. Finally, Chapter 4 demonstrated data fusion between radiation directionality and video data to assign source carrier probabilities.

Chapter 2

The Use of Radiation Detector Occlusion for Directionality

This chapter is a reproduction of the paper published in Reference [5].

2.1 Introduction

The use of a mobile directional radiation detector system could play a pivotal role in protecting a venue of interest, such as a stadium, concert venue, or airport, from illicit radioactive material. These mobile directional systems are intended for pursuit of the radiation source after a radiation detection alarm has been triggered. Figure 2.1 illustrates the desired source position estimation results for a hypothetical choke point monitoring scenario where the detector array is stationary. The rectangle labeled "checkpoint" is a station where an item is checked which causes the line of individuals to halt, such as when a passenger's boarding pass is scanned before boarding an airplane. For the sake of this example, the radiation source is carried by a passenger. Circles denote individuals who could be potential source carriers, the passengers boarding the airplane. Each circle's color denotes a passenger's identity. The blue circle containing the red "x" denotes the particular passenger carrying the radiation source. The radiation detector array composed of 3 detectors is placed offset to the boarding line. The cross-hatched cone projections represent source position estimates the width represents the 2 sigma uncertainty or 95% confidence. These

results are generated after a radiation detection alarm has been triggered, where source position estimates compile the measurements prior to the alarm for context and may take into account measurements until the radiation source has been interdicted.

There are a number of strategies to generate the desired results for the illustrated example. A coded aperture [20] or Compton imager [40] could be used for source localization, but these systems tend to be more complex, more expensive, and have lower detection efficiency when compared to directionally-capable detector arrays of similar size. There are a number of source localization methods that have been applied to detector arrays, which include Adaptively Recursive Bayesian Localization [29], Maximum Likelihood Expectation Maximization [34], and Markov Chain Monte Carlo [18]. To understand the source's movement, source localization methods are to generate source position estimates in constrained measurement times of up to a few seconds. This constrained measurement time translates into limited statistics in the measurement which hinders source localization performance for a single directional detector system. The aforementioned methods can provide the source position estimates as illustrated in Figure 2.1 but localization performance has yet to be quantified in the literature for the moving source, stationary detector array case. This challenge of localizing a moving radiation source serves as the motivation for this research on radiation directionality: enabling lone detector arrays to pursue moving radiation sources, which would benefit both static and dynamic source localization efforts.

This work builds upon prior work toward simplifying the source localization problem into source directionality, estimation of the radiation source's angular coordinate on the horizontal plane up to a few seconds, for localizing moving sources. Deb et al. [8] showed that source localization methods applied to a single non-directional or directional radiation detector can only point towards a source because both the source strength and distance cannot be inferred from a single position. Vilim et al. [41] proposed the use of multiple directional detector arrays as a cost effective alternative to sensor coverage, each array consisting of four 3" $\times$ 3" NaI(Tl) detectors (total detector mass of 5.1 kg). Both Deb et al. and Vilim et al. argue that the dynamic source localization problem is better suited for a sensor network consisting of both mobile and static detectors for cost effective venue coverage. Finally, Willis et al. [44] focused on single system directionality performance for a moving source at a fixed speed

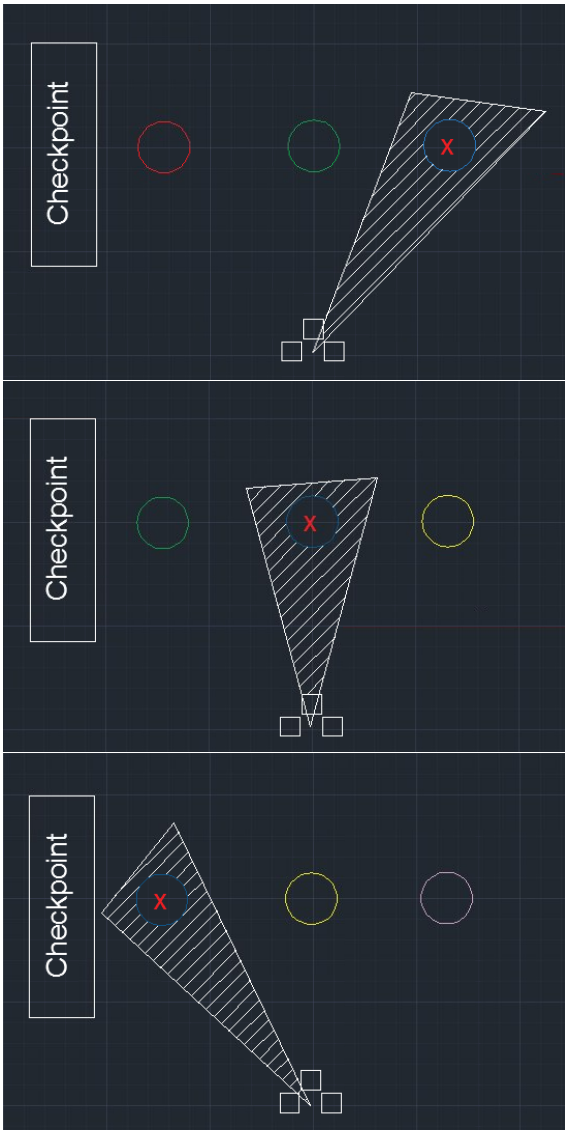


Figure 2.1: Source directionality illustrated in a hypothesized choke point monitoring scenario, such as a ticket check-in while boarding an airplane. Each time step involves a source position estimate as denoted by the conic, cross-hatched projection. The width of the source position estimates the probable source locations with a 95% probability. (Top) Source position estimate at time=0s. (Middle) Source position estimate at t=1s. (Bottom) Source position estimate at t=2s.

and distance using a detector array consisting of four 2" × 2" × 4" NaI(Tl) detectors (total detector mass of 3.85 kg) [44].

This work develops a directionality method appropriate for wearable, closely packed detector arrays. It investigates the performance of an example system as a function of uncollided gamma fluence, different energy thresholds, and two different penetrating gamma sources. The quantitative performance of directionality is reported for a wearable detector array but is general enough to be applied to other detector arrays. This wearable detector array consisted of three 2" × 2" × 4" NaI(Tl), the mass of which is a factor of 2.3 greater than a single 3" × 3" NaI(Tl) and 2.7 times smaller than a single 2" × 4" × 16" NaI(Tl). This work determined how well this detector array can point to a stationary radiation source using a short measurement, and then demonstrated that this directionality method can work in the moving source, stationary detector array case.

2.2 Methodology

This work exploited the masking of detectors by one another in the presence of a source, also known as occlusion, within a closely packed detector array. The angular response is defined as the expected response of the detector array with respect to the source's angle relative to the system, θ, and the solid angle experienced by each detector. Directionality in this work collapses the two-dimensional Cartesian plane parallel to the floor to one dimension: source angle relative to the detector array's orientation. This work uses the net count rate $\vec{y}$ where each element is the measured net count rate in each detector for a given integration time Δt. Net count rate is the number of energy depositions after thresholding and background subtraction divided by the integration time. Note that the integration time is the time during which each measurement is collected. For example, a total measurement time of 5 minutes and an integration time of 1s yields a total number of 300 measurements.

The top of Figure 2.2 shows repeated measurements of the net count rate, $\vec{y}$, of a source at some angle and distance. The count rates have clustered around a mean value due to the nature of Poisson counting statistics (explained in the source localization context in Miller et al. [29]). It is assumed that the 1-norm of the measured net count rates of each detector,

$\vec{x} = \frac{\vec{y}}{||\vec{y}||_1}$, will cluster in similar fashion to the bottom of Figure 2.2 despite differences in the observed source's distance and strength. Additionally, there is the prior assumption that the angular response used by the directionality algorithm, the template, matches the detector response observed within the detectors, the observation. Differences in source distance and strength between the template and observed affects lower energy gamma rays more than higher energies as air attenuation factors in more. More discussion on this assumption is given in Section 2.2.3.

Due to these assumptions, directionality performance ultimately depends on the amount of separation observed between the clusters in the bottom of Figure 2.2. This cluster separation is determined by the distance between each angular group's position (mean of the 1-norm of the count rates) and overlap (covariance of the 1-norm of the count rates) to one another. Normalization is done to introduce robustness such that directionality can be done despite differences between the observed and the expected source strength and distance of the radiation source. Ideally, the features are to remain invariant regardless of the source's type, strength, and distance to the detector array in order for consistent directionality estimates.

2.2.1 Experimental Setup for Static Detector Array, Static Source Case

The detector array used in this work consists of three NaI(Tl) detectors in a closely-packed detector array geometry shown in the top of Figure 2.3. The bottom two detectors were spaced 5 inches apart, while the top detector was placed 3.54" from each of the bottom detectors. In front of the detector array is a human torso phantom, approximated by a 9" x 14" ellipsoid, 32" in height. The center to center distance between both the phantom and the detector array was 10".

The angular response of the detector array was measured by placing a radiation source at a fixed distance from the center of the detector array. The geometry of the detector array is shown in the bottom of Figure 2.3. The source was placed in 15 degree increments from the center of the array. Data was collected for ten minutes at each position. Angular

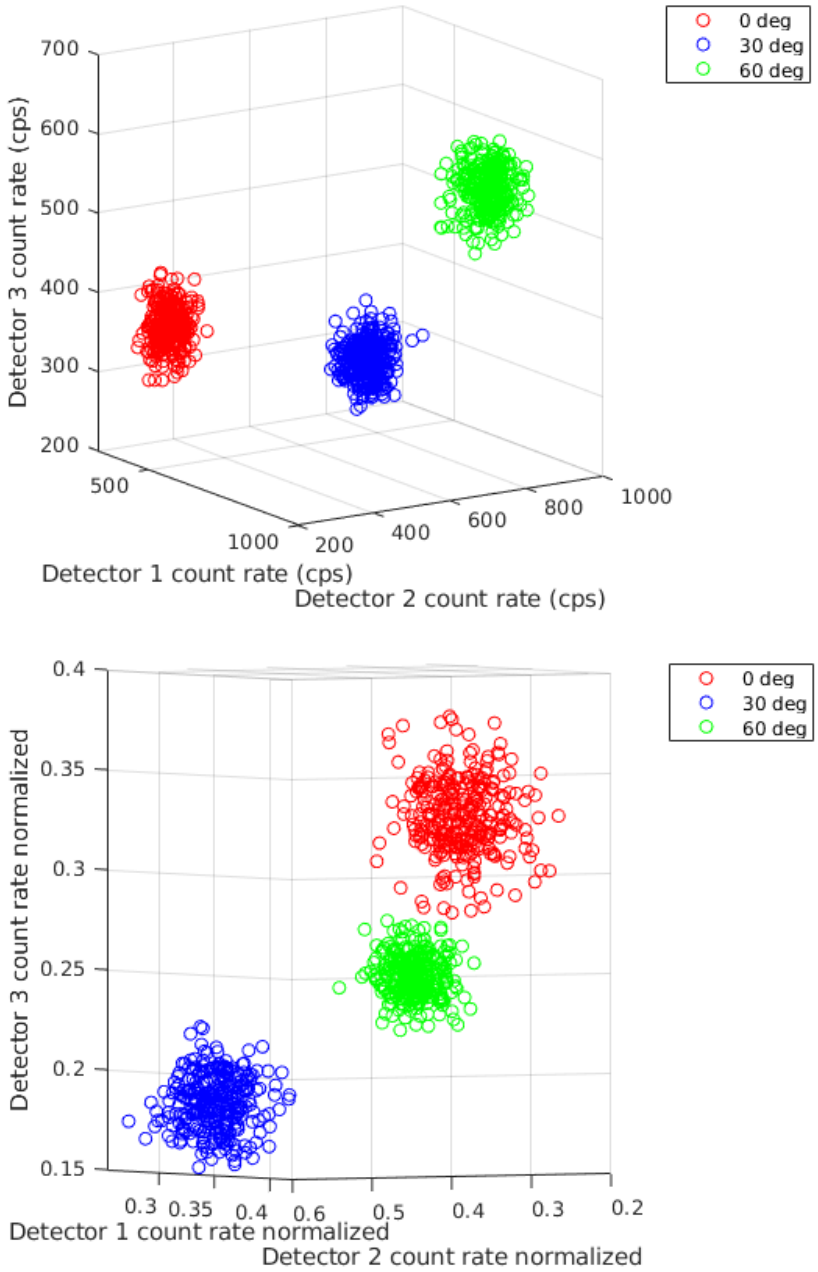


Figure 2.2: (Top) Measured net count rates of all 3 dimensions of angles 0, 15, 30, and 45 degrees. (Bottom) Measured net count rates of all 3 dimensions of angles 0, 15, 30, and 45 degrees after being normalized to the 1-norm.

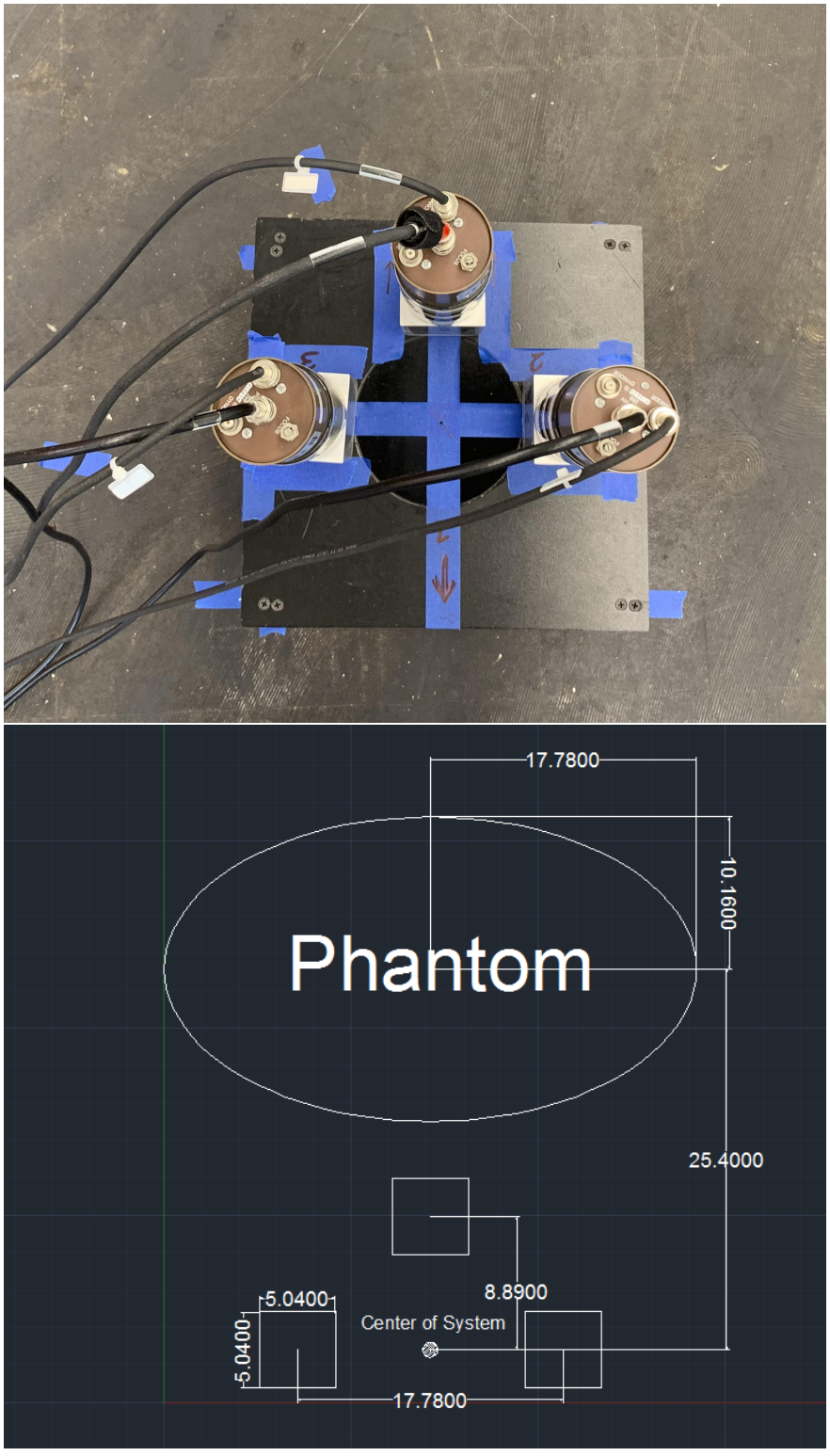


Figure 2.3: (Top) Sodium Iodide detector array geometry. 2" × 2" × 4" rectangular crystals. Phantom not shown, but is to be included in the angular response measurement. (Bottom) Two-dimensional cross section of the detector array geometry, top-down view. All units are in centimeters. Human phantom is approximated with an ellipsoid. The marked cross hatch circle is the defined center of the system for the entire angular response measurement.

responses for both 113.3 μCi Cs-137 and 34.6 μCi Co-60 sources were collected; in both cases, a 10% uncertainty in source strength was assumed. The centers of both the source and the detector array were placed 14" above the ground. Background subtraction was used to calculate the net count rate. An hour long background measurement before the experiment yielded background count rates of 255.0 $\pm$ 0.3, 265.5 $\pm$ 0.3, and 270.4 $\pm$ 0.3 cps for detectors 1, 2, and 3, respectively. Unless stated otherwise, gamma energy depositions above 40 keV were accepted after a linear energy calibration using Ba-133, Co-60, Cs-137, Eu-152, and Na-22 sources.

The data acquisition equipment consists of the NaI(Tl) radiation detectors packed with the Photomultiplier Tubes (PMT), PMT bases, a digitizer, and a high voltage power supply (HVPS). The 2" $\times$ 2" $\times$ 4" NaI(Tl) were Saint Gobain's Model 2 $\times$ 2M/2 which were already packaged with the BICRON PMTs. These PMTs were coupled to a Model 266 ORTEC PMT base. High voltages of 875V, 950V, and 950V were supplied to these bases using two HVPSs, iseg NHQ 213M and iseg NHQ 203M, powered by a NIM rack. The PMT anode pulses were acquired using a CAEN DT5720 digitizer.

Placement for both the source and detector array were marked by a manually operated turn table and an aluminum rod of fixed length. Uncertainties associated with the position of the detector array and source placement are given the worst configuration, which yields a conservative estimate on the angular uncertainty. The respective uncertainty in angle at 172.4 cm and 304.8 cm are 0.8° and 0.6°. Finally, a phantom was placed in front of the detector array with a center to center distance of 10", mimicking an operator carrying this detector array inside a backpack. An example measurement is shown in Figure 2.4, where the Cs-137 source was placed 172.4 cm from the center of the array at 0°.

2.2.2 Experimental Setup for Static Detector Array, Mobile Source Case

A 113.4 μCi Cs-137 source was moved in front of the backpack detector array to demonstrate that radiation directionality estimates can be made on moving sources. The backpack detector array and phantom are placed on top of a table. The experimentalists carried

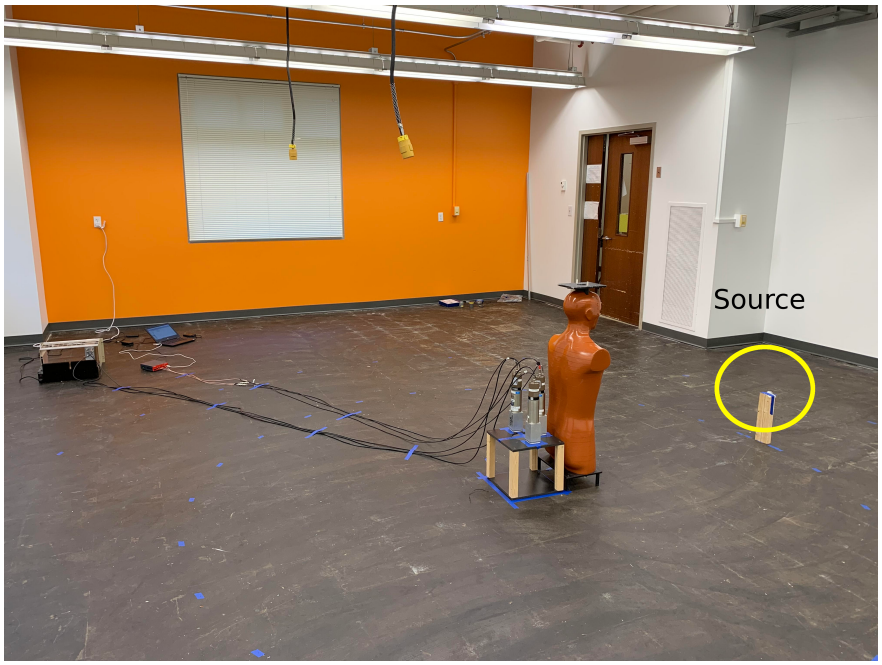


Figure 2.4: Experimental setup photo of the angular response measurement with the source position labeled with a yellow circle. The source is located at a fixed distance but is placed at different angles with respect to the center of the array. Both the centers of the source and the detectors are at the same height.

the Cs-137 source at approximately the same height as the center of the detector array at his or her own "walking pace", roughly 1 m/s. The path of each experimentalist spanned across the width (left-right) and depth (front-back) of the room. A Logitech C310 webcam attached to the front of the phantom took pictures during the experiment. The top of Figure 2.5 shows the right actor carrying the Cs-137 source with his left hand. Although the distance from the detector array to the source ranges from 200-550cm throughout this experiment, the average distance to the source was 350cm. A Velodyne VLP-16 LIDAR was placed on top of the phantom's head to generate point cloud data. The experimental setup summary picture is given at the bottom of Figure 2.5.

To note the ground truth source position, the point cloud taken with the LIDAR is measured every 1 s. The point cloud was thresholded such that the points from the walls and floors of the room were excluded. The experimentalist's hand carrying the source was manually selected every 1 s to mark the source's position after time synchronization between the radiation and LIDAR data was resolved to 0.2 s. The centroid of the selected cluster of points defined the source's position. Measurements were taken for 300 seconds, but only data where the source position within the LIDAR could be identified was included (approximately 217 seconds). The source's ground truth position is assumed to be $\pm$ 2 cm in each cardinal direction, which is the uncertainty of each individual point within the cloud. The source's ground truth angle is a function of the synchronization between the LIDAR and radiation data, the source distance, the source angle, the real time source movement vector, and point cloud measurement uncertainty. Considering the source path taken in the experiment and uncertainties associated with ground truth source position, the source's ground truth angular uncertainty was averaged to $0.6^\circ \pm 0.9^\circ$.

2.2.3 Directionality Algorithm

Maximum Likelihood Estimation (MLE) was used to perform directionality estimation. This algorithm was chosen as the data was observed to follow a multivariate normal distribution. This multivariate normal distribution assumption was found valid for integration times greater than 0.3s for the 113.3μCi Cs-137 source at 172.4cm using the Royston test statistic at the 95% confidence threshold [38, 37]. Angles from 0 to 360 degrees are divided into n

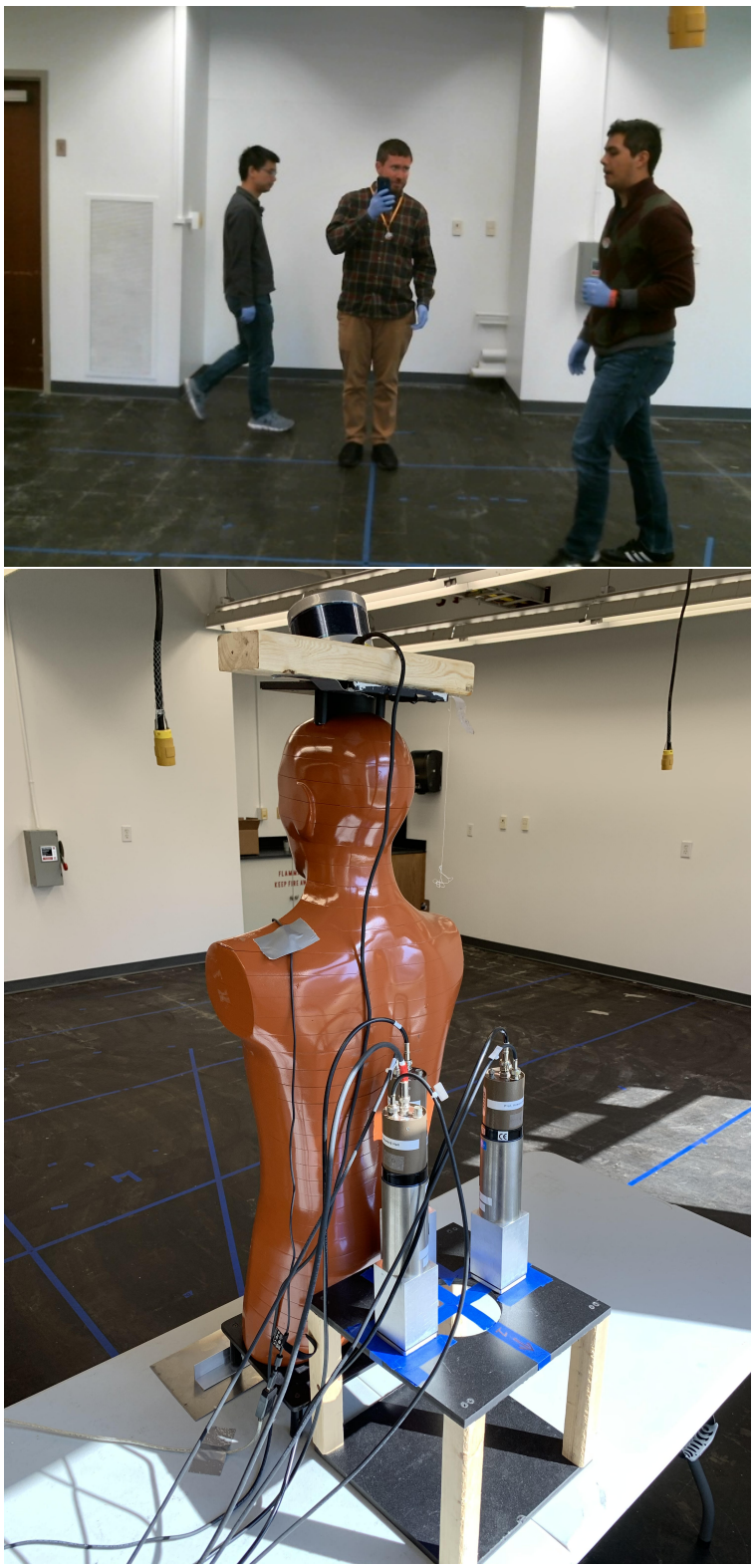


Figure 2.5: (Top) In action picture of the stationary detector array, moving source experiment. The right experimentalist is carrying the only Cs-137 source in his left hand. Experimentalists are moving left to right, right to left, front to aft, and aft to front throughout the measurement. (Bottom) Stationary detector array, moving source experimental setup. See Figure 2.3 for the top down view of the array used in this experiment as well as a detailed schematic.

angular groups and are indexed by i, such that $i = 1, 2, 3, \ldots, n$. Measurements $\vec{x}$ for each angle θ_i were characterized by their sample mean ($\vec{\mu}$) and sample covariance (Σ). Clusters shown in the bottom of Figure 2.2 are assumed to be multivariate normal, which yields the probability density function:
$p(\vec{x}|\theta_i) = (2\pi)^{-\frac{n}{2}}|\Sigma_i|^{-\frac{1}{2}}e^{-\frac{1}{2}(\vec{x}-\vec{\mu}_i)^T\Sigma_i^{-1}(\vec{x}-\vec{\mu}_i)}$. A uniform prior probability $P(\theta_i)$ was assumed such that the probability of source placement along any particular direction is equivalent. The evidence term $p(\vec{x}) = \sum_{i=1}^{k} p(\vec{x}|\theta_i)P(\theta_i)$ sums over all of the possible angles. Since measurements were taken in 15 degree increments, k is equal to 24. Now, the posterior probability in Bayes' theorem can be constructed: $p(\theta_i|\vec{x}) = \frac{p(\vec{x}|\theta_i)P(\theta_i)}{p(\vec{x})}$. The angle θ_i which maximizes $p(\theta_i|\vec{x})$ is the most likely source direction. This formulation employs the zero/one loss function, where the risk associated with choosing all angular groups is equal. Furthermore, the uncertainty in the 1-norm of the net count rate is captured within the covariance matrix, as it determines the cluster size and shape of each angular group.

The key assumption for this approach is that the net count rates, $\vec{y}$, and its 1-norm, $\vec{x}$, will cluster in similar fashion despite different source strengths and distances. This directionality approach in particular requires the count rates from each detector to follow a multi-variate normal distribution: according to the Royston's test metric, a measured net count rate of approximately 100cps in each detector. Degraded performance is to be expected when this threshold is not met. Shifts in the sample mean of the 1-normed net count rate ($\vec{\mu}_i$) and sample covariance matrix (Σ_i) of each angular group are observed when the template and observation are mismatched in differences of source strength and distance. For example, source strength and distance combinations resulting in a lower SNR than the template will degrade performance as the classification boundary calculated shifts. Differences in the covariance (cluster shape) and mean (cluster position) between the template and observed can be seen in the comparison between the 1-norm count rates between the 113.3 μCi Cs-137 source at 172.4cm (top) to the same source at 304.8cm (bottom) in Figure 2.6. The distributions across the angular groups overlap as the SNR decreases, thereby diminishing directionality performance because 1) the means are shifting towards one another as the SNR decreases and 2) the variance increases as the uncertainty in the count rate, and therefore the variance in the 1-norm of the count rate, increases.

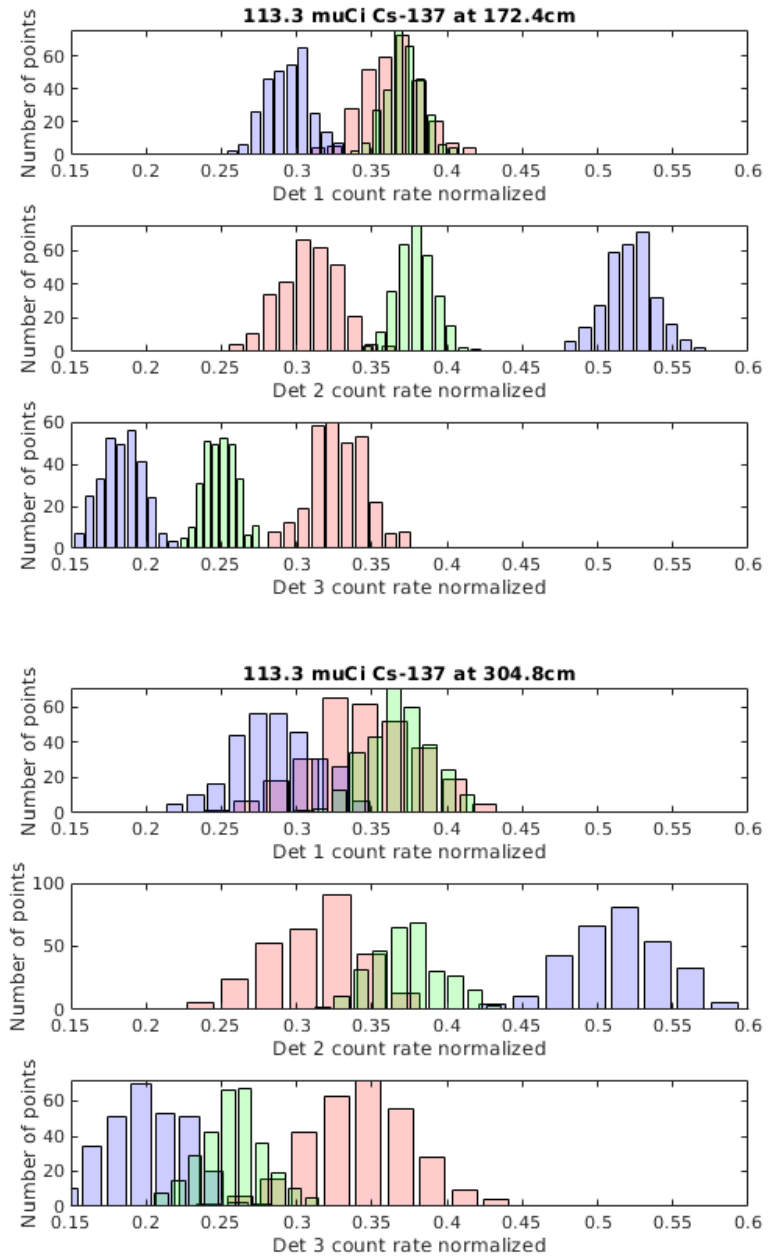


Figure 2.6: Comparison between the 1-normed count rates of angular groups 0 (red), 30 (blue), and 60 (green) degrees. Plots are histograms across each Cartesian dimension. The top is the higher statistics case, while the bottom represents the case in lower statistics. (Top) 133.3 μCi Cs-137 source at 172.4cm. (Bottom) Same source at 304.8cm.

2.3 Results

2.3.1 Angular Response Measurements

The results of the measured angular responses are shown on the top of Figures 2.7, 2.8, and 2.9. The bottom of each of the figures showcases the same data after normalization, which serves as the input to the directionality algorithm as described in Section 2.2.3. Figure 2.7 is referred to as the reference angular response measurement as it is the template which the directionality algorithm is looking for in future measurements. A depression in the net count rate was observed from 315° to 45° (-45° to 45°) due to the attenuation of gamma rays through the phantom. As such, the count rate when the source was placed in front of the detector array, 0°, was less than the count rate when the source was behind the detector array, 180°. At 90°, the source was directly to the bottom of the detector array with detectors 1 and 2 are in full view of the source, while detector 3 was occluded entirely by detector 2. The center to center distance from detector 2 to the source is less than that from detector 1 in the 90° case (166.1 vs 172.5 cm, respectively) despite the fixed center to center distance from the source to the detector array, which explains detector 2's highest count rate, followed by detector 1, then detector 3. This trend was mirrored in the 270° case, where the source was directly to the to the left of the detector array.

Figure 2.8 shows measurements taken in the same manner as the base measurement, except the source distance is increased to 304.8 cm. This change is made to study the effect on directionality performance with respect to a decreased gamma flux. This change in source distance yields a lower count rate magnitude as the measured counts decrease *approximately* with source strength, A_0, over the square of distance, r, while neglecting air attenuation ($\frac{A_0}{r^2}$). Count rate changes due to air attenuation are expected to be 2% to 4% with the source distances and types considered in this work. Figure 2.9 showcases the angular response taken at the same distance as the reference measurement, but with a 34.6 μCi Co-60 source instead of a Cs-137. So not only is the number of incident gamma rays different, but the occlusion effects of the detector array differ as higher energy gamma rays are involved. Compared to the reference measurement, detectors blocking full view to another cause less

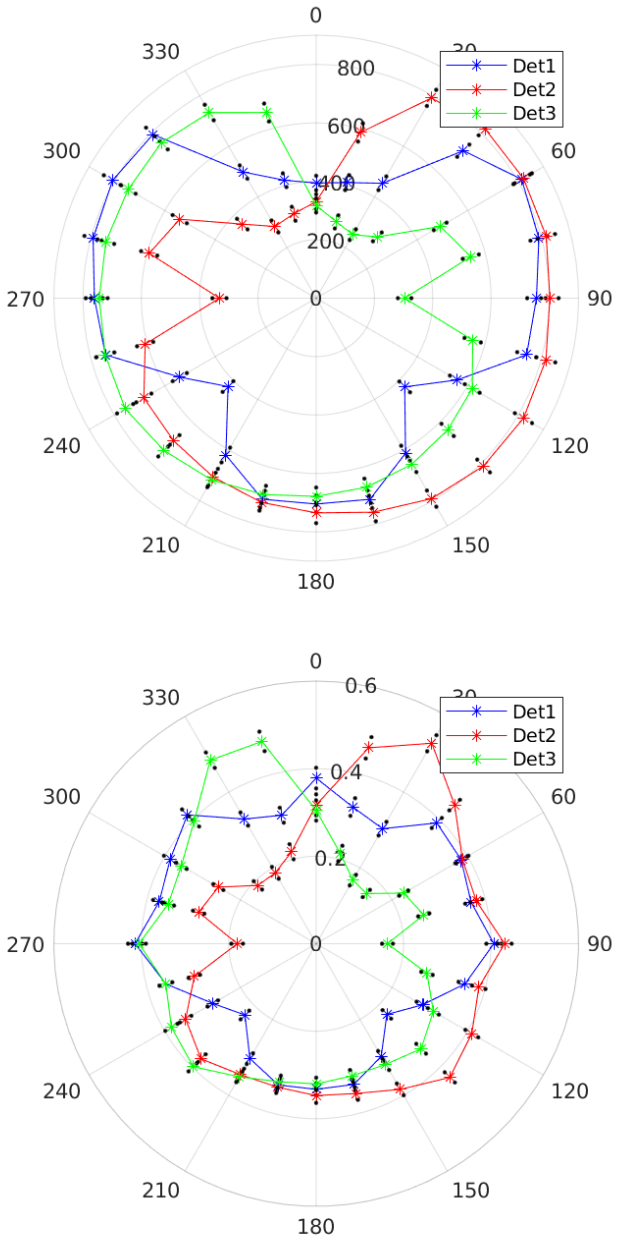


Figure 2.7: (Top) Measured angular response for a 113.3 μCi Cs-137 source at 172.4 cm. The polar angle represents source position in degrees, while the radius denotes magnitude in (cps). (Bottom) Measured angular response for a 113.3 μCi Cs-137 source at 172.4 cm after normalization. Polar angle corresponds to source position in degrees, while the radius denotes magnitude but is unitless due to normalization.

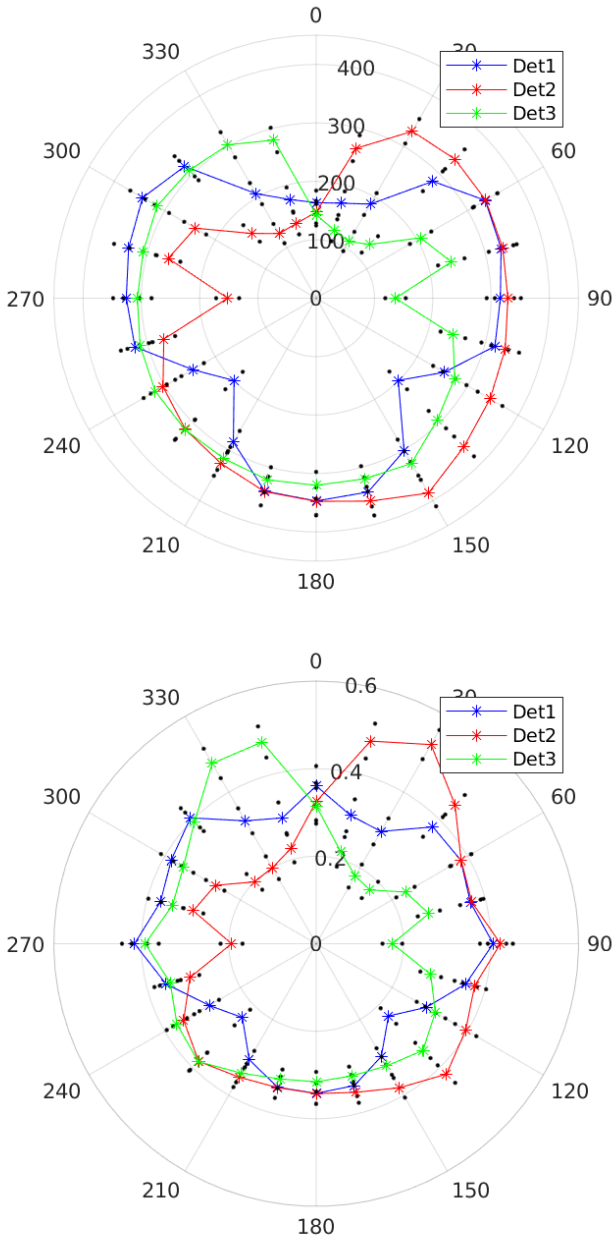


Figure 2.8: (Top) Measured angular response for a 113.3 μCi Cs-137 source at 304.8 cm. The polar angle represents source position in degrees, while the radius denotes magnitude in (cps). (Bottom) Measured angular response for a 113.3 μCi Cs-137 source at 304.8 cm after normalization. Polar angle corresponds to source position in degrees, while the radius denotes magnitude but is unitless due to normalization.

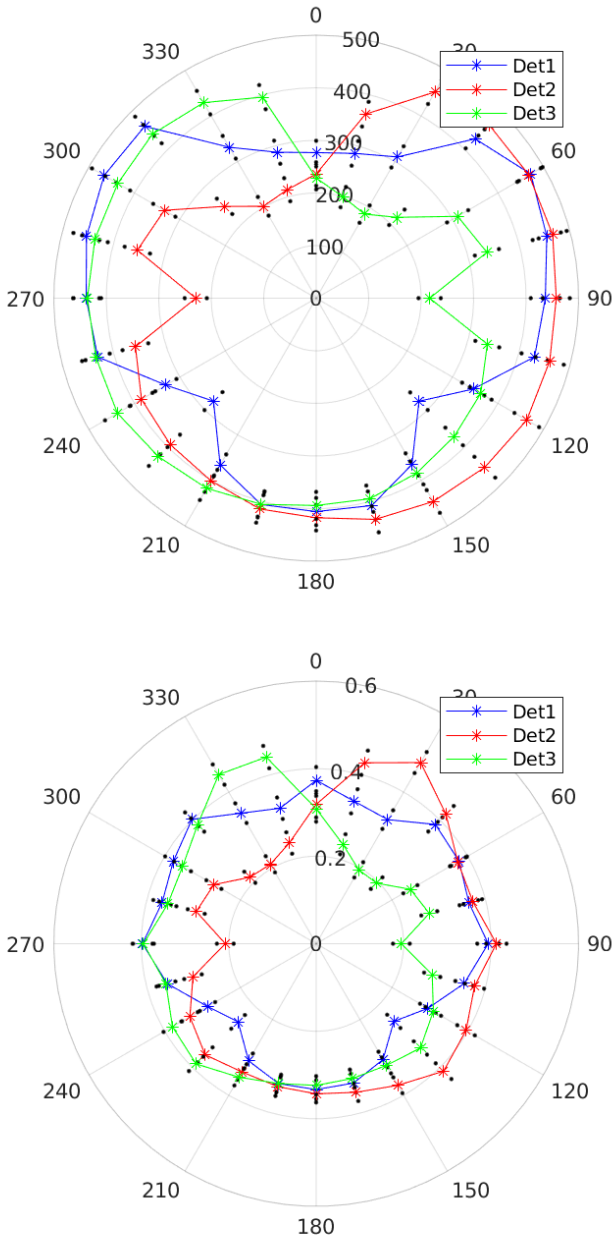


Figure 2.9: (Top) Measured angular response for a 34.6 μCi Co-60 source at 172.4 cm. The polar angle represents source position in degrees, while the radius denotes magnitude in (cps). (Bottom) Measured angular response for a 34.6 μCi Co-60 source at 172.4 cm after normalization. Polar angle corresponds to source position in degrees, while the radius denotes magnitude but is unitless due to normalization.

of a drop due to the decrease in cross section with respect to the increase in gamma ray energy.

2.3.2 Directionality Performance for the Stationary Detector Array, Stationary Source

Directionality performance and behavior for 1 s integration times are given in the confusion matrices in Figures 2.10, 2.12, and 2.13. These plots are used to quantitatively assess the directional estimates made by the algorithm given a single time integration period. Each pixel's color in the confusion plot can be interpreted as the probability of classifying ground truth angle i as angle j, as indexed in the horizontal and veritcal axes of each confusion plot. In other words, the horizontal axis represents when the algorithm makes a specific angular estimation, while the vertical axis represents the actual location of the source. The values of probability are given in the color bar to the right of each confusion plot. Each angle is defined with the angle's uncertainty with respect to the distance: 0.8° for 172.4 cm and 0.6° for 304.8 cm. In this analysis, the distribution in the columns are of interest to understand the misclassification behavior. These classification behaviors of each confusion matrix are coarsely condensed into a single value, the Mean Absolute Error (MAE), for purposes of discussion. Ideally, the best performance would have a low MAE and have a black diagonal across the plot, both of which indicate that correct direction estimates were made by the algorithm. The off-diagonal colors reveal a probability of angle i being miscategorized as angle j, while the MAE denotes significant errors between the ground truth and estimated angle.

Confusion plots give insight to an array's directionality behavior. Figure 2.10 describes the directionality performance of a 113.3 μCi Cs-137 source at 172.4 cm (top) and 304.8 cm (bottom) in template matching scenarios. Directionality estimates made at 30° are correct with a probability of over 95 %, with the remainder misclassified to the adjacent 15°. This misclassification behavior is not only for adjacent angles. Directionality estimates of 285° can misclassify sources actually placed at 300°, 255°, and 0°. Plots of the deviation from the ground truth source angle for both of these cases can be observed by plotting the columns of

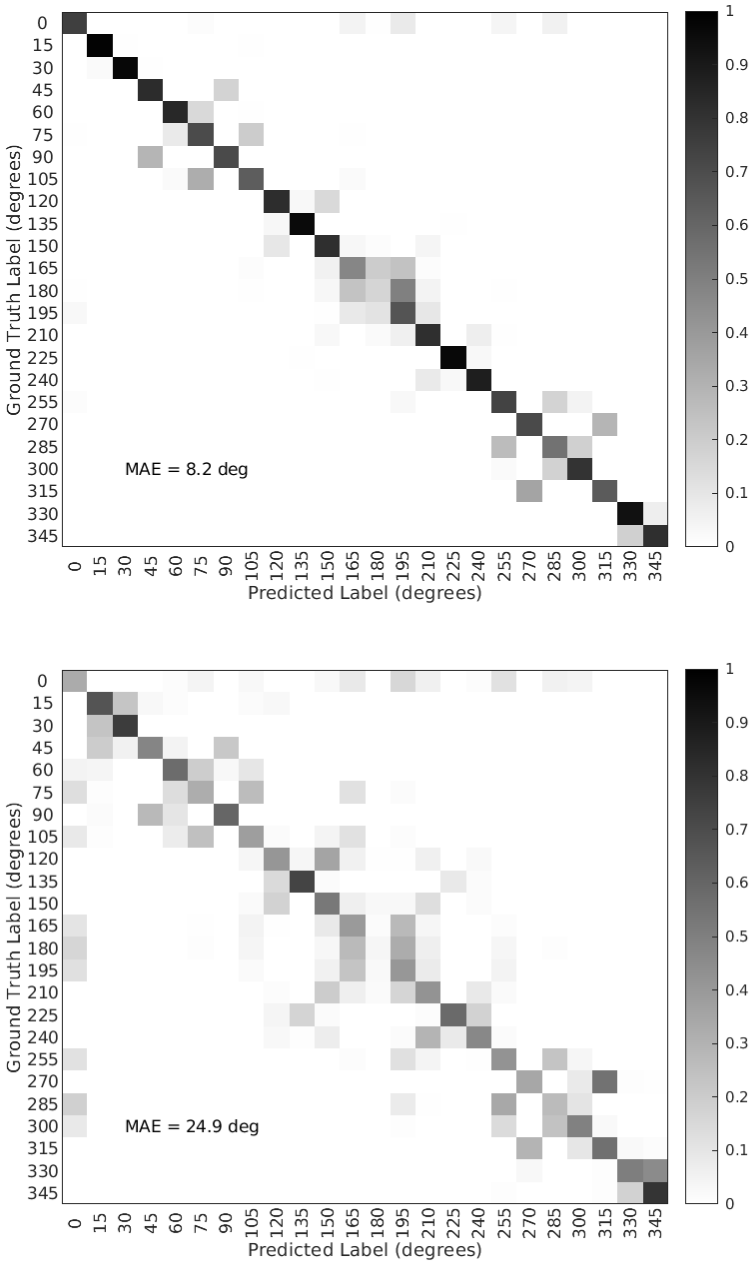


Figure 2.10: (Top) Directionality performance while trained with a 113.3 μCi Cs-137 source at 172.4 cm while observing a 113.3 μCi Cs-137 at 172.4 cm. (Bottom) Directionality performance while trained with a 113.3 μCi Cs-137 source at 172.4 cm while observing a 113.3 μCi Cs-137 at 304.8 cm.

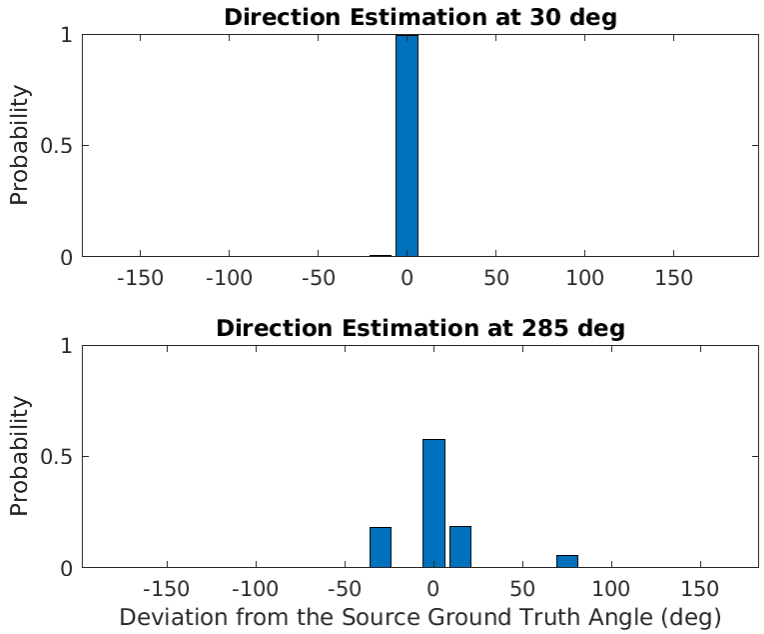


Figure 2.11: Probability with respect to deviation from ground truth source angle. (Top) Directionality estimates at a source angle of 30°. (Bottom) Directionality estimates at a source angle of 285°.

the confusion plots, as shown in Figure 2.11. In relation to the angular response template in the top of Figure 2.8, the count rates and respective uncertainties of angles 0°, 255°, and 300° overlap with the count rate at angle 285°. This overlap causes the directionality algorithm to confuse the Poisson realizations within the count rate of sources placed at 0°, 255 °, and 300° for angle 285°'s mean and covariance. The classification behavior for angles with similar angular responses gets worse with decreased SNR as shown with an increased source distance in the bottom of Figure 2.10 and decreased integration time in the top of Figure 2.12, as both scenarios involve decreased statistics. Likewise, differentiation between angles with similar angular responses can be made with more statistics, as better classification performance between these angles can be observed with increased integration time shown in the bottom of Figure 2.12. These results suggest that strategies which improve statistics will improve directionality performance. In the context of the choke point monitoring scenario, slowing down the search or increasing detector mass by making the detectors longer are examples of factors that can be expected to improve directionality performance in the case of a static detector, static source.

Figure 2.13 describes the directionality performance for a 34.6 μCi Co-60 source at 172.4cm. Note that the directionality is diminished compared with the Cs-137 measurement. This is to due to the following two variations in the experimental setup: 1) the decrease in source strength leads to less statistics for a fixed time integration and, more interestingly, 2) the decreased cross section associated with a higher energy gamma rays which produces a less favorable angular response. Note the angular response for the Co-60 source shown in the top of Figure 2.9. There are more instances of angles with similar means and overlapping uncertainties compared to the Cs-137 case. The directionality performance reflects the need for higher statistics to differentiate angles with this high overlap, as when the directionality performance increased if the integration time is increased to 5 s as in the bottom of Figure 2.13.

Figure 2.14 is the directionality performance with respect to the uncollided gamma fluence, where each data point represents the MAE computed from each confusion matrix. The MAE is no substitute for a confusion plot, as the classification behavior could be very unfavorable in some directions compared to others depending on the scenario. For example,

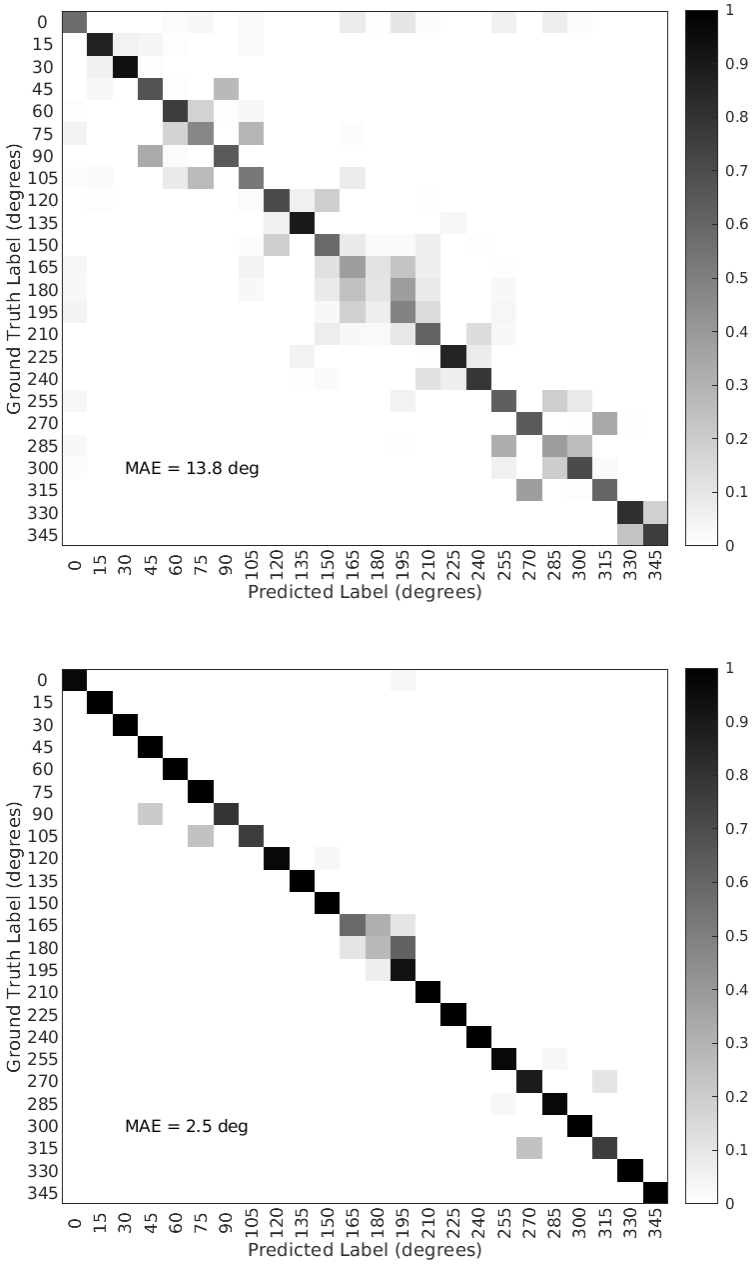


Figure 2.12: (Top) Directionality performance while trained with a 113.3 μCi Cs-137 source at 172.4 cm while observing a 113.3 μCi Cs-137 at 172.4 cm using 0.5s as the integration time. (Bottom) The same as the top plot, but using 5s as the integration time.

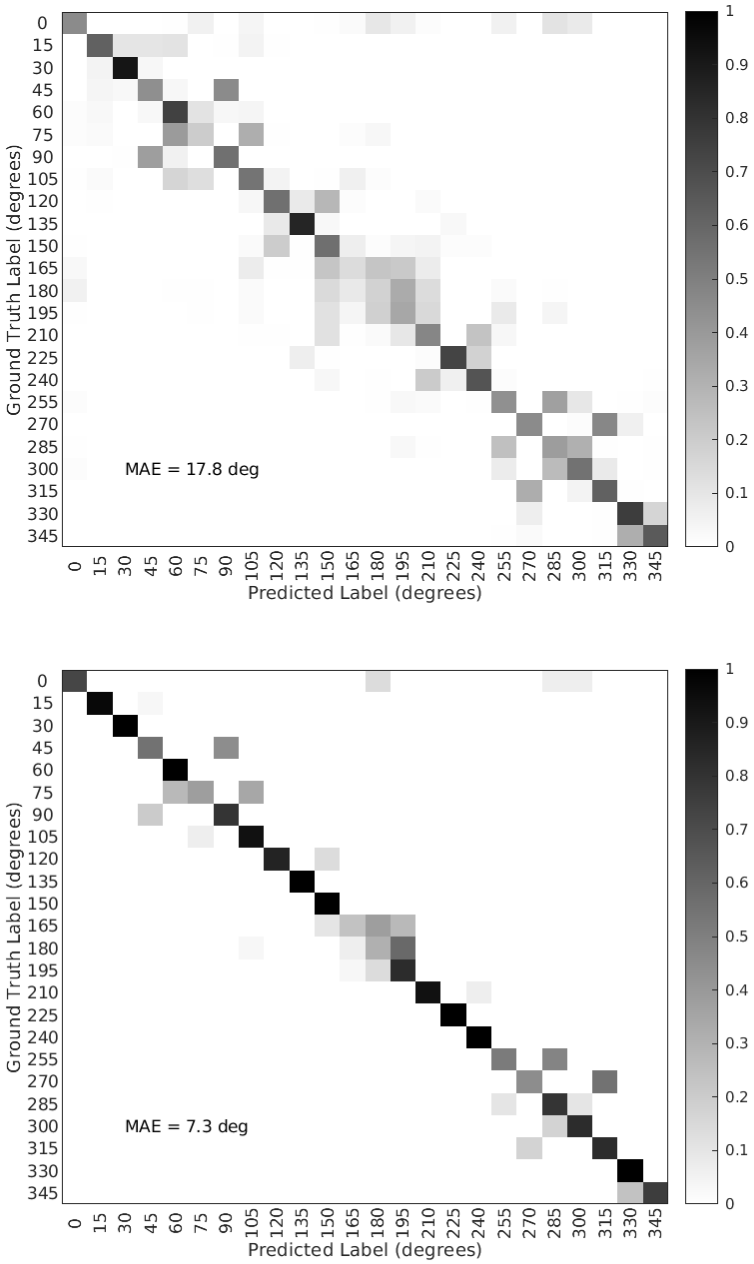


Figure 2.13: (Top) Directionality performance while trained with a 34.6 μCi Co-60 source at 172.4 cm while observing a 34.6 μCi Co-60 at 172.4 cm. Integration time for both is 1 s. (Bottom) Directionality performance with a 34.6 μCi Co-60 source, 172.4 cm, integration time of 1 s source template observing a 34.6 μCi Co-60, 172.4 cm, integration time of 5 s.

one could compare direction ranges 330° to 30° and 45° to 105° to conclude that the 0° is the preferred orientation to a suspected source direction. Moving forward with the discussion, the uncollided gamma flux is estimated to the first degree using $\phi = (A_0\beta/r^2)e^{-\mu r}$, where ϕ is the rate of uncollided gamma rays incident on the detector array per unit area, A_0 is the source strength, β is the source's branching ratio, r is the source distance, and μ is the total attenuation coefficient of air. The uncollided gamma flux acts as a first-order estimate for the incident gamma rays upon the detector array as it neglects the contribution of environmental scattering to the measured count rate. Note that multiplying the uncollided gamma flux with the domain of integration times, Δt, is an approximation to measuring sources of different strength but fixed integration time and distance. This approximation fails to account for experimental complications such as increase in dead time and pulse pileup when the count rate increases.

Due to better counting statistics, the MAE decreases with respect to the number of gamma particles incident to the detector array for a given integration time. A trend was observed between directionality performance and uncollided gamma fluence. An example exponential fit is shown in Figure 2.14 with a coefficient of determination ¿ 0.99. The x-coordinate is the uncollided gamma fluence Φ. To calculate Φ for a 535 μCi Cs-137 source at 300 cm, the rate of gammas given off by the source into the 4 π is 16,825,750 gammas/s, and the uncollided gamma flux to the detector array would be 175 (gammas / cm^2 s) assuming an air attenuation coefficient and density of 1.875 x 10^{-1} cm^2/g and 0.0012 g/cm^3, respectively. Using the MAE trend equation for the 113.3 μCi Cs-137 at 172.4 cm case (the bottom equation of Figure 2.14), a 1s integration time would give Φ = 175 (gammas/cm^2) and an interpolated MAE of 6.2°. For a 3s integration time, Φ = 524 (gammas/cm^2) and the interpolated MAE would be 2.7°.

In general, it was observed that lower set energy thresholds were better for directionality. Figure 2.15 shows the directionality performance with respect to the lower energy threshold. The lower energy thresholds are the same for both the template and the measurement, and as they are incrementally increased, directionality performance degrades. This is due to directionality information and counting statistics from the Compton continuum being excluded, making classification more challenging. When the energy threshold is increased to

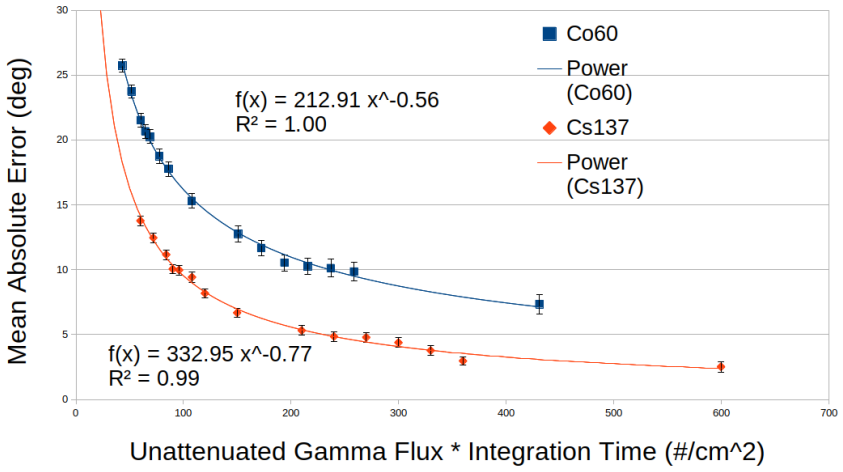


Figure 2.14: Directionality performance with respect to uncollided gamma fluence. The top equation is a fit for the Co-60 MAE, while the bottom equation is a fet for the Cs-137 MAE.

325 keV, the minimum net count rate of 100 cps needed to pass the Royston's test statistic, the multivariate normal assumption, starts to be violated by angle 0°. This particular angle has the lowest count rate across all detectors as the source is attenuated by the phantom. According to the angular response in the top of Figure 2.7, this energy threshold is where angles 0°, 90°, and 270° violate the multivariate normal assumption, while the rest of the angles are still in compliance. Further increasing the energy threshold decreases the directionality performance as more angles start violating the multivariate assumption, as can be observed when the maximum count rate, the count rate measured at 180 °, approaches the 100 cps requirement. Increasing the threshold has the similar effect to decreasing the integration time, where counts are excluded allowing Poisson variation to increase the overlap of angles with similar templates. Note that throughout this work the background is known a priori from the average of a 3-hour background collect. Background discrimination of this degree in practice would be challenging, especially in dynamic background scenarios such as when the backpack detector array is in motion.

2.3.3 Directionality Demonstration in the Stationary Detector Array, Moving Source

Application of the directionality algorithm was also demonstrated in a static detector array, moving source case (hereby referred to as static-dynamic case). The angular response of a 113.4 μCi Cs-137 at 172.4cm template and a 1 s integration time was used for the template. A comparison between the estimated and ground truth source angles is shown in the top Figure 2.16, where a MAE of 12.7° is calculated. The ground truth source angles are discretized into 15° increments for a more consistent comparison with other results in this paper, as shown in the bottom of Figure 2.16. A MAE of 13.6° is calculated using the discretized ground truth source angles. Note that these errors do not constitute the MAE of the array itself, as this particular experiment only carried the source from -45° to 45° (315° to 45°). Most of the confusion plot is white because this experiment only included source angles between 315° and 45°.

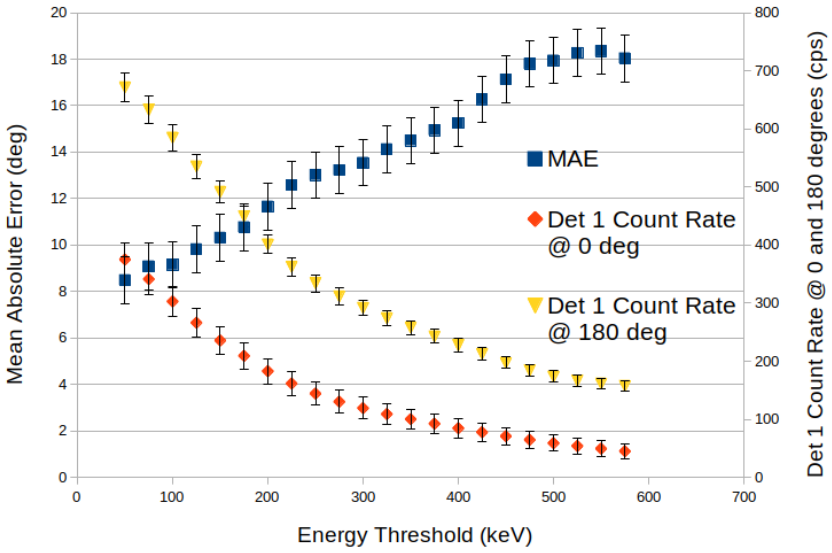


Figure 2.15: Directionality performance and count rates of detector 1, both with respect to set energy threshold. The blue squares denote MAE values which use the left axis, while the red diamonds and yellow triangles denote detector 1 count rate values using the right axis. The red diamonds represent the minimum count rate, the count rate of detector 1 when the source is placed at 0°. The yellow triangles represent the maximum count rate, the count rate of detector 1 when the source is placed at 180 °. Detector 1 is chosen arbitrarily, as all 3 detectors trend with one another at 0° and 180°. A 113.3 μCi Cs-137 at 172.4 cm was used with a 1 s integration time for the MAE, and the count rates were measured in the same manner as the angular response measurements.

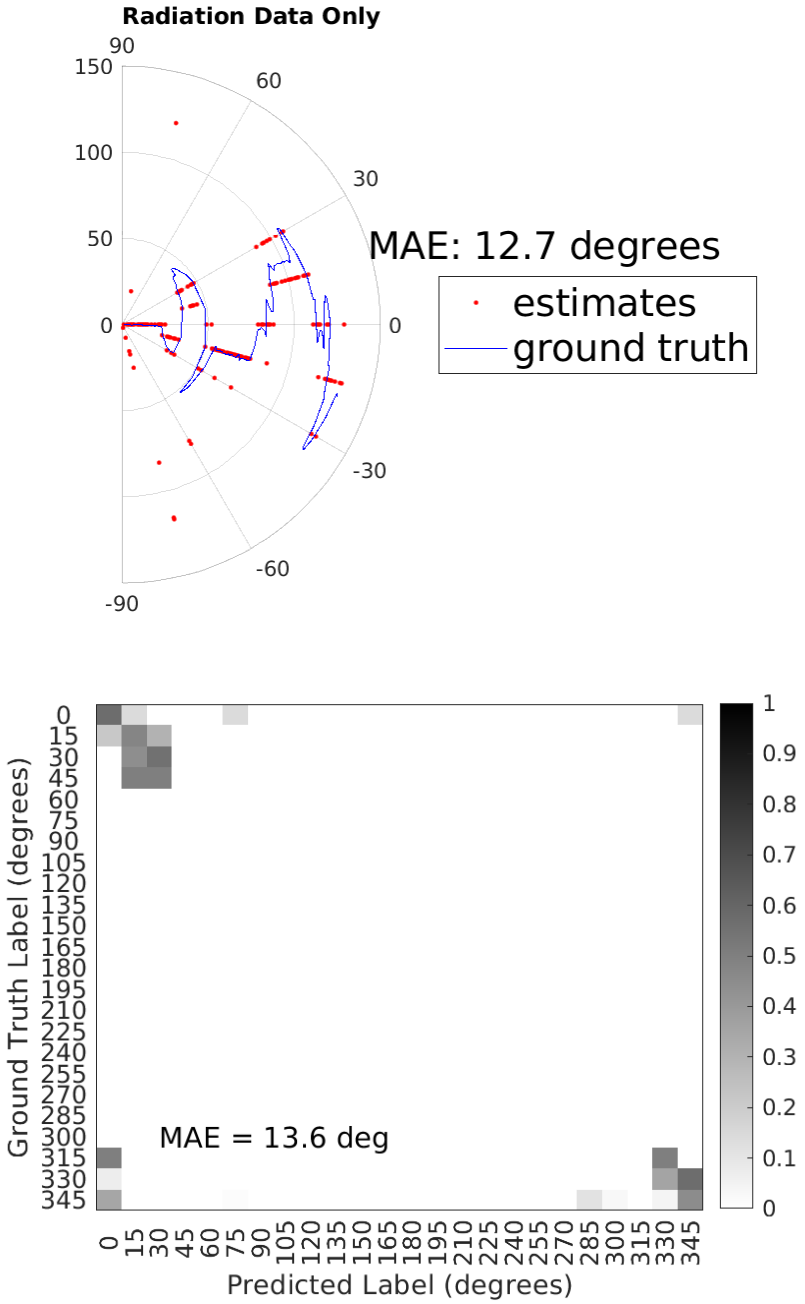


Figure 2.16: (Top) Directionality comparison to the ground truth in the static detector array, moving source case. As mentioned in the Methodology, ground truth source angle is known to $0.6° \pm 0.9°$, but is not plotted for clarity. (Bottom) Directionality performance as observed from the static detector array, moving source experiment.

As the average source distance to the detector is 350cm, a crude comparison can be made between the bottom of Figure 2.10 and the bottom of Figure 2.16 as they use the same source and have a similar distance. At first glance, the MAE from the static-dynamic case is lower than the static-static case. Upon closer inspection, the static-static case's MAE is 24.9 ± .5°, while the static-dynamic case's MAE is 14 ± 20°. Furthermore, this experiment only includes source angles from 315° to 45°. These caveats serve as a caution that these results represent merely a demonstration rather than a full characterization of the potential application of the proposed directionality algorithm to the case of moving sources, which is beyond the scope of this work.

2.4 Conclusions

This work demonstrated that Maximum Likelihood Estimation can be applied to closely packed detector arrays to achieve directionality: estimating the direction of a detected source using a single, short measurement. Using the Mean Absolute Error (MAE) as evaluation metric, the performance of the proposed directionality approach using a 1 s integration time was found to be 8.2° using a 113 μCi Cs-137 at 172.4 cm from the center of the array and 17.8° for a 34.6 μCi Co-60 at 172.4 cm. Directionality performance improved for both cases to 2.5° and 7.3°, respectively, as the integration time was increased to 5 s.

This work quantified the uncertainty in directionality estimates under different working assumptions. The gamma fluence to the detector array was manipulated by changing both the integration time of the measurement and the source distance to the array. Both of these changes showcased this method's robustness to unknown source strengths and distances. Radiation measurements with short integration times are used to make directionality estimates to point towards sources, such as the choke point monitoring scenario considered in Section 1. This work focused on direction estimates upon a static source, where the measured net count rate is derived from a fixed solid angle; however, this work has also demonstrated directionality estimates on a moving source in a rudimentary capacity. The dynamic source, stationary detector array experiment yielded a directionality MAE of 12.7° using a 113.4 μCi Cs-137 source at an average distance of 350 cm.

All of the results were achieved using measurements from a detector array consisting of 3 NaI(Tl) detectors with a combined mass of 2.89 kg. This method is expected to work with any close-packed detector array having at least two detectors. Directionality using this method can be done as long as one can characterize the angular response of the system as detailed in the Section 2. According to Ayaz-Maierhafer et al. [2], increasing the number of detectors or increasing detector mass may result in better directionality performance.

2.5 Acknowledgements

This material is based upon work supported by both the Department of Homeland Security and Department of Energy National Nuclear Security Administration under Award Numbers DHS-15-DNDO-077-001 and DE-NA0002576. This report was prepared as an account of work sponsored by an agency of the United States Government. Neither the United States Government nor any agency thereof, nor any of their employees, makes any warranty, express or implied, or assumes any legal liability or responsibility for the accuracy, completeness, or usefulness of any information, apparatus, product, or process disclosed, or represents that its use would not infringe privately owned rights. Reference herein to any specific commercial product, process, or service by trade name, trademark, manufacturer, or otherwise does not necessarily constitute or imply its endorsement, recommendation, or favoring by the United States Government or any agency thereof. The views and opinions of authors expressed herein do not necessarily state or reflect those of the United States Government or any agency thereof.

Chapter 3

Source Localization of the WIND Backpack Detector Array

3.1 Introduction

Radiation source localization is the act of locating a non-natural radiation source. Typically, a collection of radiation measurements from at least one detector is used to locate the fixed source, such that the measured data is compared to the expected data from a radiation transport model to infer the most likely source position. A Coded Aperture Imager (CAI) or Compton Imager (CI) could also be used for this application but is less typical as they often have less sensitivity than a 2" $\times$ 2" NaI(Tl) detector. Source localization performance is determined from some measure of how close the source position estimate is from the ground truth source position. This performance is dependent on the radiation measurement system, the transport model used, and the method used to compare the expected and measured counts.

This work characterizes the localization performance of a portable, wearable, backpack-sized radiation detector array with a total scintillator payload of 4.7 kg. Both the average and standard deviation of source localization errors are computed for this wearable detector array as a function of source offset as done in Reference 29. Furthermore, other experimental variables such as detector array speed, integration time, source type, and computational time are varied to understand their respective effects on localization performance. The

quantitative difference in performance due to these changes in variables for this wearable detector array are of particular interest.

3.2 Methodology

3.2.1 Angular Response

A set of angular response measurements for the detector array used in localization experiment was collected in the same fashion described in Reference 5. The angular response was collected in 5^o increments with a 5 minute collection time. PMT drift was assumed to be negligible as the measurement was performed in a temperature controlled environment. The average count rate determined from the 1-hour background measurement was subtracted out to obtain the net count rate from the sources for this angular response measurement.

The results of the angular response measurement have been provided below in Figures 3.1 and 3.2. Detectors 1 and 2 are the NaI(Tl) detectors, while detectors 3 and 4 are the CLYC detectors. Detectors 3 and 4 are optically separated and stacked upon one another, with detector 4 is placed on top of detector 3. Across all angles, it was observed that detector 4 had a higher count rate than detector 3. Furthermore, it was observed that detector 1 has a higher net count rate across corresponding angles (45^o compared to 315^o, 90^o compared ot 270^o, etc.) compared to detector 2. These observations were due to diagonal pieces of aluminum added for structural integrity for the frame, such that detector 3 experienced more occlusion than detector 4 and detector 2 experienced more occlusion than detector 1.

3.2.2 Radiation Transport

One-dimensional radiation transport is used to calculate the expected count rate, λ, in each detector. The expected count rate is a combination of both the background and source contributions: $\lambda = s + b$. The source contribution to the expected count rate is based on the positions of both the detector array, $\vec{r_d}$, potential source position, $\vec{r}$, the source strength, A_0, air attenuation coefficient, μ, the detector's angular response, $\epsilon(\vec{r_d}, \vec{r})$, and the angular response measurement distance, d_m. For this work, the background count

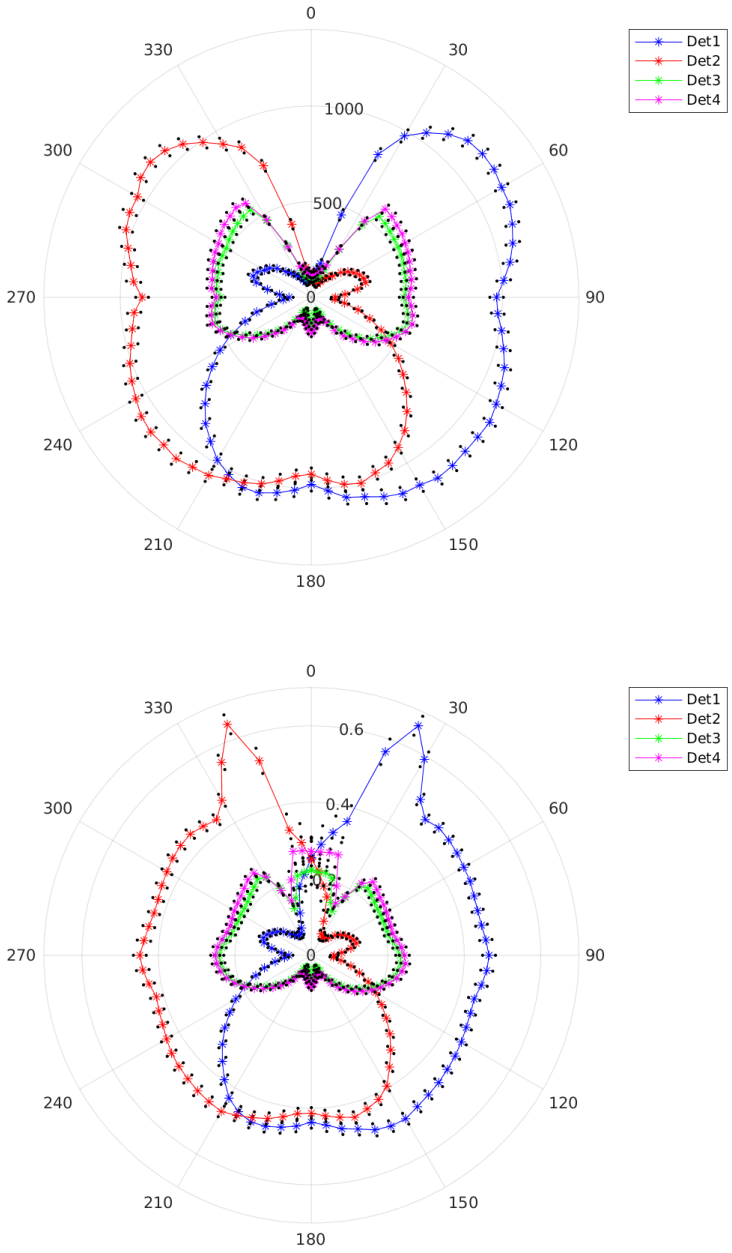


Figure 3.1: (Left) Measured angular response for a 95 μCi Co-57 source at 172.4 cm. The polar angle represents source position in degrees, while the radius denotes detector count rate in cps. Uncertainties are the standard deviation of the count rate across the 5 minute measurement. (Right) Measured angular response for a 95 μCi Co-57 source at 172.4 cm after L1 normalization. Polar angle corresponds to source position in degrees, while the radius denotes magnitude but is unitless due to normalization.

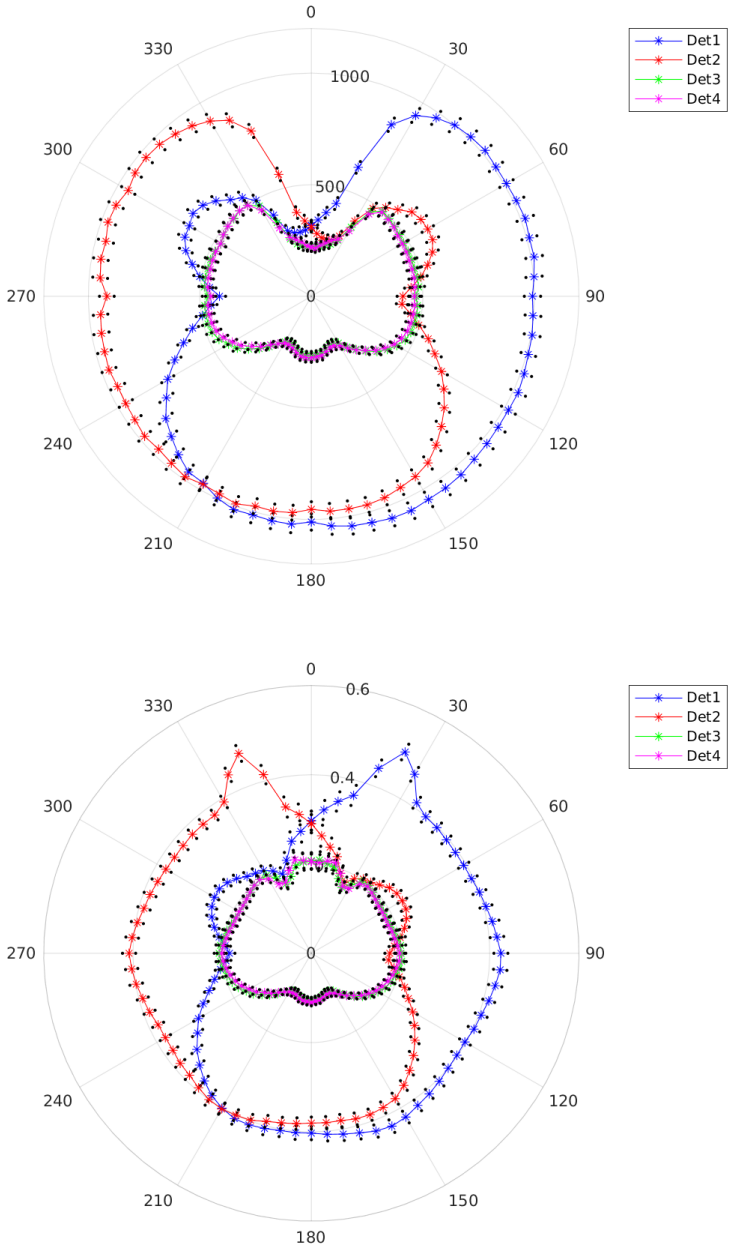


Figure 3.2: (Left) Measured angular response for a 113 μCi Cs-137 source at 172.4 cm. The polar angle represents source position in degrees, while the radius denotes detector count rate in cps. (Right) Measured angular response for a 113 μCi Cs-137 source at 172.4 cm after normalization. Polar angle corresponds to source position in degrees, while the radius denotes magnitude but is unitless due to normalization.

rate is assumed to be constant and is modeled as zero as the net count rate is used as the input for the localization algorithm. The angular response term, $\epsilon(\vec{r_d}, \vec{r})$, is captured using the angular response measurement. The source counts contribution is modeled as $s = \Delta t A_0 \frac{\epsilon(\vec{r_d},\vec{r})}{4\pi||\vec{r}-\vec{r_d}||_2^2} e^{-\int_0^{\vec{r}-\vec{r_d}} \mu(\vec{r'})d\vec{r'}}$. This work uses Maximum Likelihood Expectation Maximization (MLEM) to solve for the source term, A_0, for each potential source position, $\vec{r}$. Note that position vectors $\vec{r}$ and $\vec{r_d}$ are in reference to some origin in the cartesian system. In this experiment, the origin is defined by the position of the LIDAR sensor.

The denominator of the one-dimensional radiation transport equation is $\frac{1}{4\pi||\vec{r}-\vec{r_d}||_2^2}$, which describes the point source response: the chance a radiation particle is radiated from the source's position r to the detector's position $\vec{r_d}$. The exponential term, $e^{-\int_0^{\vec{r}-\vec{r_d}} \mu(\vec{r'})d\vec{r'}}$, describes the fraction of radiation particles that had not interacted between the particle's journey from source's position $\vec{r}$ to the detector's position $\vec{r_d}$. Multiplication of the point source response, the uncollided fraction of particles, angular response, and the source strength, A_0, yields the source's contribution, s, to the expected count rate, λ.

3.2.3 Maximum Likelihood Expectation Maximization

MLEM is used to iteratively solve for vector $\vec{x}$ in the linear equation $A\vec{x} + \vec{c} = \vec{y}$. The search space is discretized into pixels, where every pixel is considered a source. The source search space was discretized into pixels of 5 cm by 5 cm: the detector array's position uncertainty. Elements of matrix A are computed with the one-dimensional radiation transport equation to map the source activities in vector $\vec{x}$ to measurements in vector $\vec{y}$. Element $a_{i,j}$ of matrix A represents the radiation transport from pixel j to measurement i. The rows of matrix A are labeled with detector positions r_d, while the columns of matrix A are labeled with pixel positions r. Elements of vector $\vec{x}$ represent the source strength of a given pixel out of a total of n pixels in the space where the source is being localized. In essence, $\vec{x}$ represents position dependent estimated source activity. The A matrix is the radiation transport matrix which maps the source strengths, $\vec{x}$, to the measured count rates, $\vec{y}$. Matrix A contains m rows and n columns, where m is the number of measurements. The number of measurements is computed by the number of detectors multiplied by the total length of the data segment in seconds divided by the integration time. Vector $\vec{c}$ is a constant vector of size m which

represents the background contribution to each measurement. Finally, vector $\vec{y}$ is the vector of count rate measurements. This experiment was conducted inside a building where a constant background is assumed. As such, the background subtracted net count rates are input into $\vec{y}$, thereby making the background contribution, $\vec{c}$, a zero vector.

Solving for $\vec{x}$ creates an image where every pixel contributes to every measurement. For example, the first row of matrix A dotted with the $\vec{x}$ yields y_1. This operation can be interpreted as how each source activity across all pixels contributed to the first measurement. If a single point source is assumed, as what is actually true in the experiment, one can normalize each pixel indexed by k using $p_k = \frac{x_k}{\sum_{j=1}^{n} x_j^2}$, where x_j is the pixel value and n is the number of pixels in the image. This is an implicit assumption when performing maximum a posteriori (MAP), where source location estimate is chosen to be the maximum value within the generated probability map, as done in Reference 29. The image is then condensed into a single value to summarize the localization performance, L, using $L = \sum_{j=1}^{n} p_j \left\| r_j - r_0 \right\|_2$. Lower values of L denote better localization performance. Scoring the image in this fashion is essentially a weighted average euclidean distance between the estimated source position to the ground truth source position, r_0, given the assumption of a single point source as MLEM models every pixel as a source. Scoring the localization results with L is a way to force MLEM to make a source estimated using a weighted average, which allows a rough comparison to be made with MLE where a single source position is chosen via MAP which implicitly assumes a single point source.

Calculation time is ultimately a function of domain definition and hardware. Source localization estimates were done using post processing with an Intel i7-8700 CPU and a NVIDIA GTX 1070Ti with 8GB VRAM. The search space in this work consisted of 5 cm $\times$ 5 cm grid of pixels in a search space of 10 m $\times$ 10 m. The transport matrix, A, shape for a 30 s data segment and an integration time of 1.0 s is 120 $\times$ 10,000. Table 3.1 lists sample calculation times with respect to MLEM iteration number for this particular domain. MLEM iterations of 100 and 1,000 suggest a data transfer bottleneck on loading the matrices onto the GPU, while higher iterations suggest a bottleneck in calculation speed on the GPU itself. Furthermore, these results also suggest that a 5 s rolling buffer with 10,000 MLEM iterations could be an example of a real time calculation configuration for this domain definition and

hardware. Calculation times could also be improved by decreasing the search space's range or resolution, i.e. a 10 cm × 10 cm pixel size on a 7.5 m × 7.5 m grid would yield a transport matrix shape of 120 × 5,625, or the use of a better GPU. Note that the number of MLEM iterations was set to 10,000 for the analysis which follows unless otherwise mentioned, as it was observed that the source position estimates did not change more than 0.05 m (the width of a single pixel) between 10,000 and 100,000 iterations for most scenarios.

This localization metric intends to give insight on the accuracy (defined as the average weighted average euclidean distance between ground truth and estimated source position) and precision (defined as the standard deviation of the weightd average euclidean distance between ground truth and estimated source position) across multiple measurement segments. References 34 and 8 did not comment on their accuracy nor precision on their synthetic dataset despite being the most appropriate analogues to this work. Reference 19 gave the accuracy and precision as a function of included measurement time using Markov Chain Monte Carlo as their comparison procedure. The introduced localization metric serves as a bridge to generate similar plots as Reference 29 describing localization precision and accuracy. Since MLE generates a single result denoting the most likely source position and MLEM generates a source activity map where every discretized pixel is modeled as a source, the source localization metric L is needed to "select" the most likely source position under the assumption of a single point source. Note that References 29 and 19 assumes a single point source within their methodology.

3.2.4 Experimental Setup

The detector array was placed on top of a cart as shown in Figure 3.3. The detector array consisted of 2 NaI(Tl) detectors with 54 × 54 × 152 mm dimensions and 2 CLYC(Ce) detectors that stack upon one another to the same dimension. Two optically separated CLYC(Ce) detectors were used because a single CLYC(Ce) detector could not be grown to the same dimension as the NaI(Tl) detector. Each CLYC(Ce) detector was attached to a Hamamatsu R6231 photomultiplier tube (PMT), while each NaI(Tl) detector was attached to a SensL silicon photomultiplier (SiPM) Array J-60035-4P-EVB. The layout of the detectors formed an isosceles triangle. The center to center distance between the

Table 3.1: Sample calculation times with respect to number of MLEM iterations for a 30 s data segment.

Number of MLEM Iterations	Total Calculation Time (s)
100	0.2
1,000	0.4
10,000	4
100,000	38
1,000,000	390

NaI(Tl) detectors was 7.09 cm, while the same distance between the center of the CLYC(Ce) detectors and either of the NaI(Tl) detectors was 8.57 cm. Throughout the experiment, the two NaI(Tl) detectors were closest to the source. Signal from each PMT was fed through separate ORTEC Model 113 preamplifiers. A custom power module was built to power the preamplifiers from a battery source. The anode pulses from the 2 SiPM and the 2 pulses from the preamplifiers were collected through 4 separate channels of a CAEN DT5725 digitizer. CLYC(Ce) detectors were included to give the system neutron sensitivity. Ideally, the entire system would be composed of detectors that are both neutron and gamma sensitive, such as 3 NaIL detectors or 3 Li-6 enriched CLYC(Ce) detectors (see Reference 2 for more detail). The system is powered by a lithium ion battery. Energy thresholds were determined by the location of known peaks from Cs-137, Ba-133, and Co-57 sources. Unless mentioned otherwise, the energy threshold was set to 81 keV for the analysis which follows. Furthermore, the background for the localization experiment was determined using a 30 minute background collect prior to measurement.

As shown in Figure 3.4, the cart was moved past a source while varying a number of experimental variables. These variables include integration time, detector array speed, source offset, source type, and counts taken from different parts of the energy spectra. The cart is moved past a source in predefined source offsets of 1.2, 2.2, 3.2, 4.2, or 5.1 m. Source types include a 113.4 μCi Cs-137 source and a 95 μCi Co-57 source with an associated 10% uncertainty in both source activities. Both the height of the radiation source and the midpoint height of the array were the same: 1.1 $\pm$ 0.02 m from the floor. The cart position was determined from a manually segmented point cloud data measured every 0.2 s measured with a Velodyne VLP-16 LIDAR. The LIDAR was positioned just under and in front of the source such that the ground truth source position was (-0.3 m, 0 m), while the origin of the coordinate system was (0 m, 0m). Two different speeds of the cart was found to be 0.46 $\pm$ 0.02 and 0.69 $\pm$ 0.02 m/s after the cart's position information was processed. Array position uncertainties were determined to by at most 7 cm in the y-dimension and negligible in the x-dimension. Time integrations were taken at both 0.2 s and 1.0 s intervals.

The pointcloud segmentation procedure consisted of manually labeling the cart's position within the scene. Figure 3.5 is a snapshot of a pointcloud acquired in a 0.2 s period. Robot

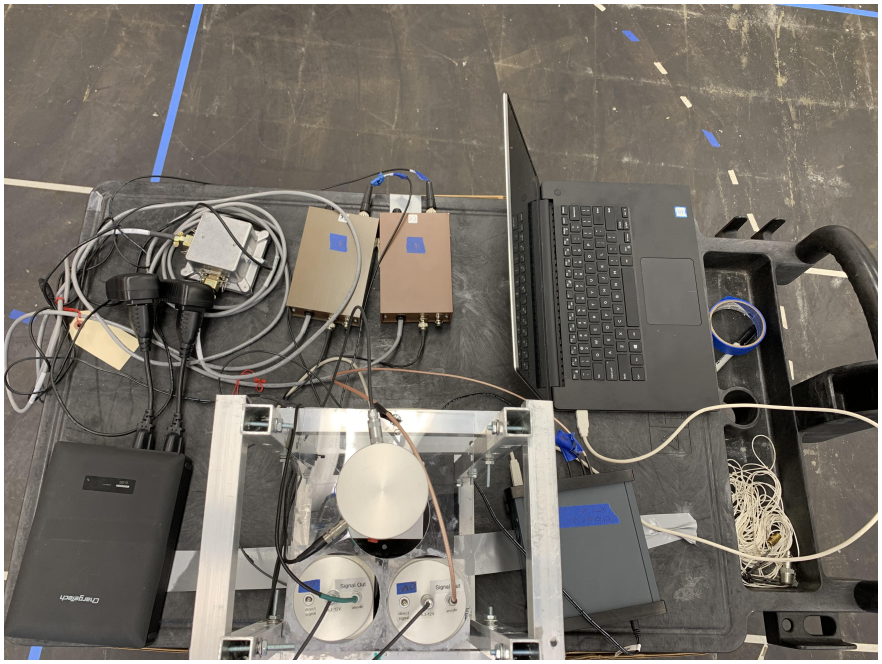


Figure 3.3: The source localization detector array setup. At the top left is a silver component: a custom power supply used to power the two ORTEC Model 113 preamplifiers. At the bottom left is a black box which is the lithium ion battery. The detector array is positioned at the bottom middle. At the top middle, there are the two brown Model 113 preamplifiers. At the bottom right is the CAEN DT5725 digitizer. Finally, the laptop used for data acquisition is shown at the top right.

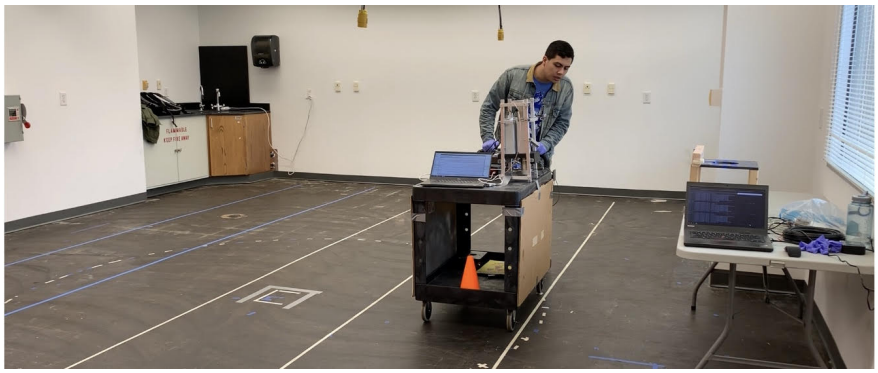


Figure 3.4: Source localization experiment in action. The experimenter moving at walking speed pushes a cart containing the detector array along one of the straight lines past a radiation source positioned at the same height as the center of the detectors.

Operating System (ROS) data analysis code was written such that the points described by the walls, floor, and measurement table were excluded, as if mocking up the more relevant outdoor environment. The experimentalist labeled the points induced by the cart's surfaces such that the detector array position could be inferred to an uncertainty of ±5 cm and ± 7 cm in the y-direction when the cart is traveling 0.46 and 0.69 m/s, respectively. The majority of the systemic uncertainty is due to the time synchronization between the radiation and LIDAR modalities could be resolved to 0.2 s. Each point's positional uncertainty is driven by the sensor's angular uncertainty of 0.2^o and distance measurement of ±3 cm, is negligible as the uncertainties are averaged out after 100s of points are selected after manual segmentation.

3.3 Results

3.3.1 Iteration Convergence Criteria

Before diving into the source localization trends, a note on source localization estimates with respect to number of MLEM iterations is described. Figures 3.6 and 3.7 show source localization estimates with 10,000 or 100,000 MLEM iterations, respectively. Both results use data reflecting a 30 s measurement of the detector array passing by a 113 μCi Cs-137 source at 0.46 m/s and a source offset of 2.2 m and a 1.0 s integration time. Figure 3.6 is less precise with a root mean square (RMS) pixel value of 0.097, while FIgure 3.7 is more precise with a pixel value RMS of 0.075. This precision trend is observed in Figure 3.8, where higher MLEM iterations were more precise: the Root Mean Square (RMS) of all pixel values decreased across all source offsets as the number of MLEM iterations increased. The convergence criteria was that the source position estimates did not shift more than the positional uncertainties of the experiment, 0.05 m. In this particular instance, Figures 3.6 and 3.7 are equally accurate as the distance of the pixel weighted average of the source position to the ground truth source position, or the localization error, is the same: 1.02 m. Figure 3.9 shows the localization error as a function of source offset and number of MLEM iterations, where 10,000 and 100,000 have within 0.05 m accuracy across all 30 s

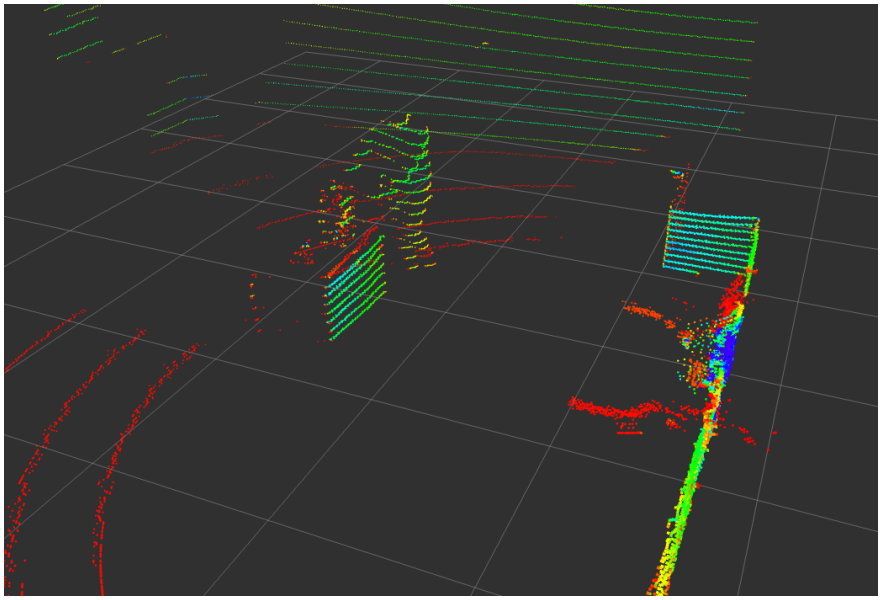


Figure 3.5: An example of an acquired point cloud during the experiment. At the middle of the point cloud, an experimentalist is pushing the cart setup shown in Figure 3.4. At the left of the point cloud, the red points denote contours describing the floor of the room. The back wall can be found at the top of the image labeled by green points. Towards the right of the figure, the cluster of points describes a wall with windows.

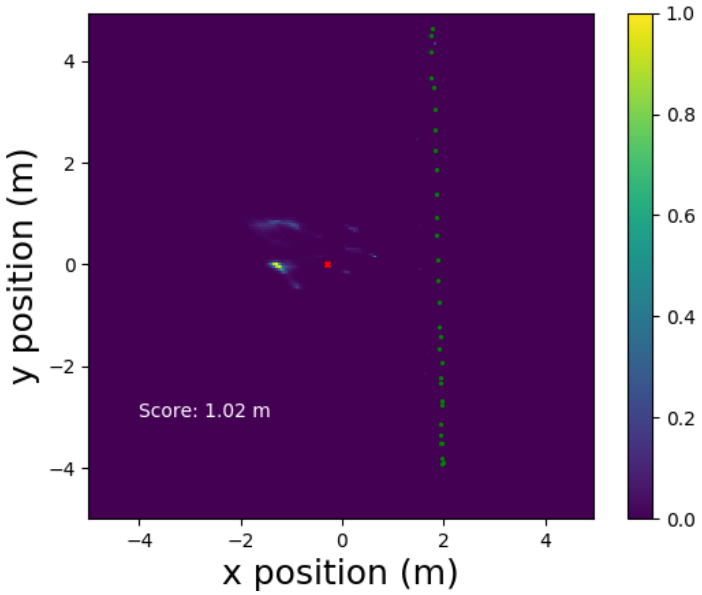


Figure 3.6: Sample of a source localization result. Red "x" denotes ground truth source position. Green dots denote detector array positions. The source was a 113 μCi Cs-137 source at a 2.2 m source offset. Detector array speed was at 0.46 m/s, and the net count rate was taken after a 81 keV energy threshold was applied with a 1.00 s time integration. MLEM iterations set to 10,000.

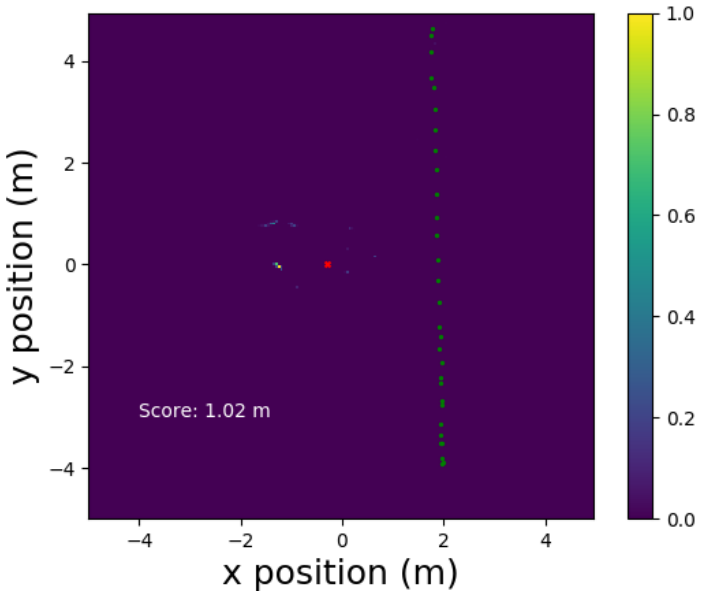


Figure 3.7: Sample of a source localization result. Red "x" denotes ground truth source position. Green dots denote detector array positions. The source was a 113 μCi Cs-137 source at a 2.2 m source offset. Detector array speed was at 0.46 m/s, and the net count rate was taken after a 81 keV energy threshold was applied with a 1.00 s time integration. MLEM iterations set to 100,000.

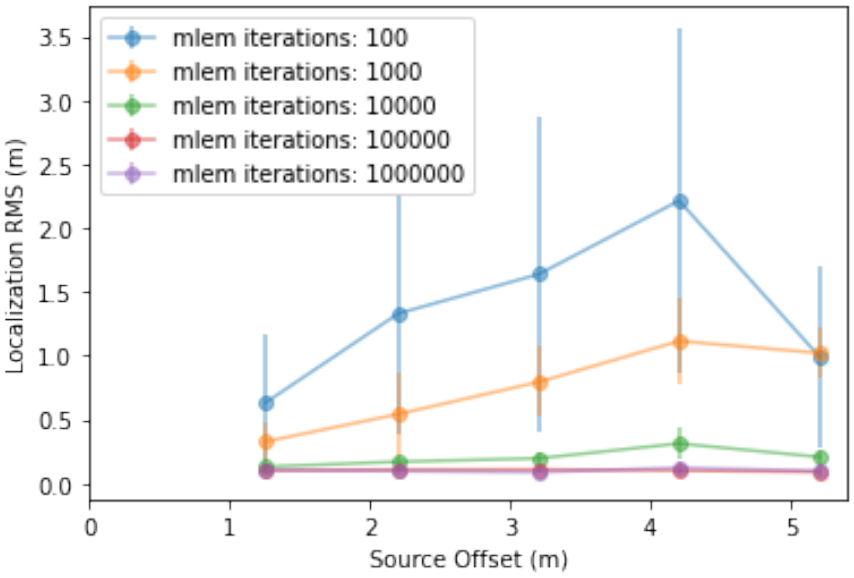


Figure 3.8: Localization RMS with respect to source offset using 30 s measurements. Results for a 113 μCi Cs-137 with 1.00 s time integrations and 0.46 m/s detector array speed. See the text for analysis.

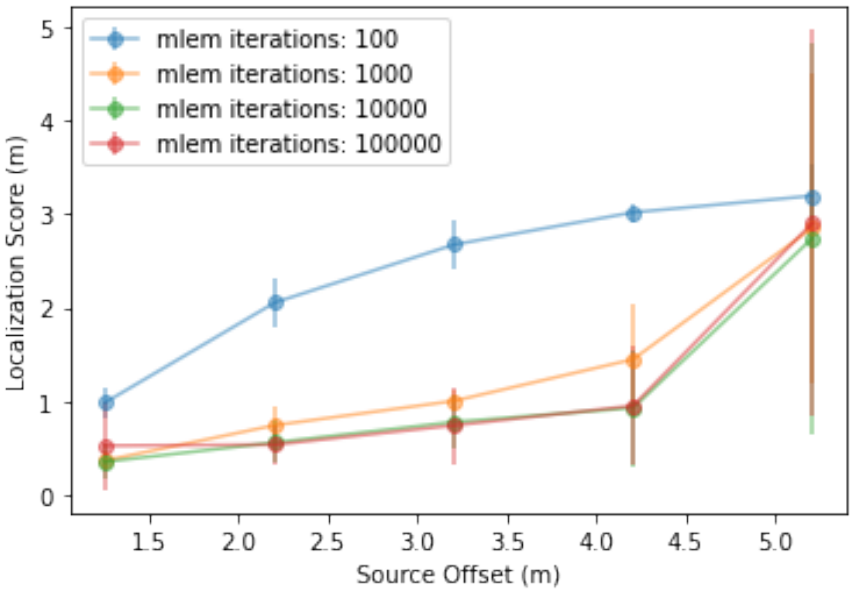


Figure 3.9: Localization performance with respect to source offset using 30 s measurements. Results for a 113 μCi Cs-137 with 1.00 s time integrations and 0.46 m/s detector array speed. See the text for analysis.

measurements. Note that the uncertainty at the 5.1 m offset is because the lack of statistics to make accurate source position estimates.

3.3.2 Source Type and Source Offset

Figures 3.6 and 3.10 can be compared to understand the localization estimate differences between a 113 μCi Cs-137 and 95 μCi Co-57 source, respectively. Both Figures showcase a 30 second measurement at a 2.2 m source offset, 1 s integration time, 0.46 m/s array speed, and 81 keV energy threshold. The results suggest that it is easier to localize the Co-57 source due to its lower energy gamma photons despite the Cs-137 source's higher source strength. Upon comparison of Figures 3.6 and 3.11, where the only difference between the scenarios are the source offsets of 2.2 and 4.2 m, respectively, smaller source offsets are expected to have better source localization performance. This observation is not surprising as higher source offsets involve measurements with poorer counting statistics. Note that all of the Figures involved source position estimates that suggest multiple sources, when in reality there is only a single source in the experiment. However, with the use of the introduced localization metric, these estimates are averaged with the weight of their pixel value to calculate a weighted average distance to the ground truth source position where one source is assumed for each calculation.

Figure 3.12 compares the localization scores between the 95 μCi Co-57 and 113 μCi Cs-137 sources. This figure also highlights that localization performance accuracy not only degrades at higher offsets, but the source localization error's variance increases as well. It was found that it was easier to localize the 95 μCi Co-57 source than the 113 μCi Cs-137 source as the counting statistics in each detector are a product between fluence and intrinsic efficiency. This can be observed in each detector's opacity to 122 and 662 keV gamma photons upon comparison between Figure 3.1 and 3.2, where the net count rates for the 113 μCi Cs-137 source at 150 degrees were 1050 $\pm$ 37, 933 $\pm$ 35, 242 $\pm$ 19, and 255 $\pm$ 19 cps. For the 95 μCi Co-57 source, the net count rates at the same angle were 1133 $\pm$ 37, 907 $\pm$ 32, 105 $\pm$ 15, and 152 $\pm$ 18 cps.

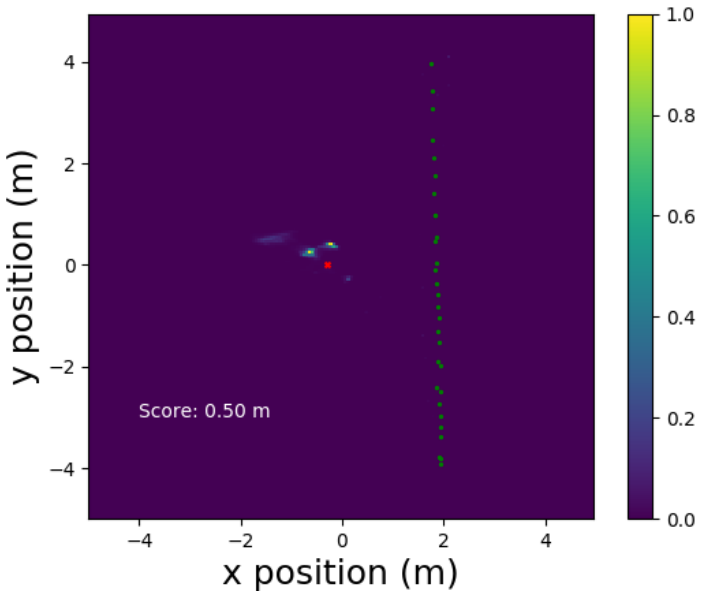


Figure 3.10: Sample of a source localization result. Red "x" denotes ground truth source position. Green dots denote detector array positions. The source was a 95 μCi Co-57 source at a 2.2 m source offset. Detector array speed was at 0.46 m/s, and the net count rate was taken after a 81 keV energy threshold was applied with a 1.00 s time integration.

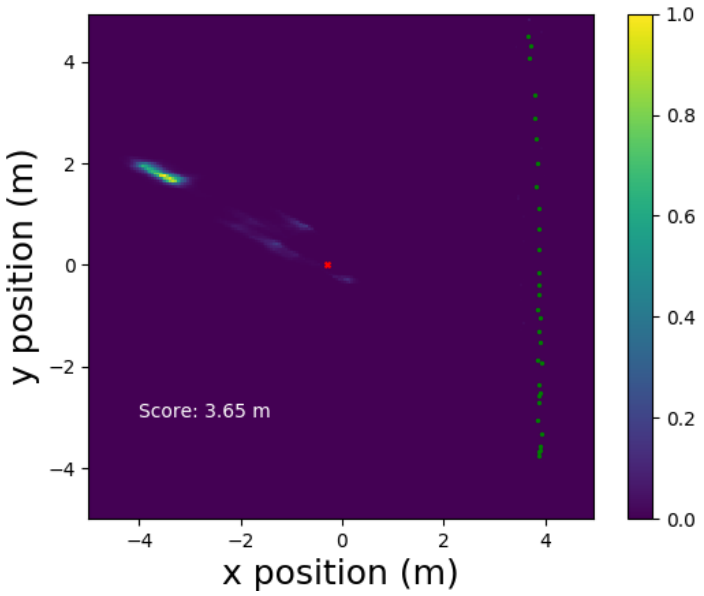


Figure 3.11: Sample of a source localization result. Red "x" denotes ground truth source position. Green dots denote detector array positions. The source was a 113 μCi Cs-137 source at a 4.2 m source offset. Detector array speed was at 0.46 m/s, and the net count rate was taken after a 81 keV energy threshold was applied with a 1.00 s time integration.

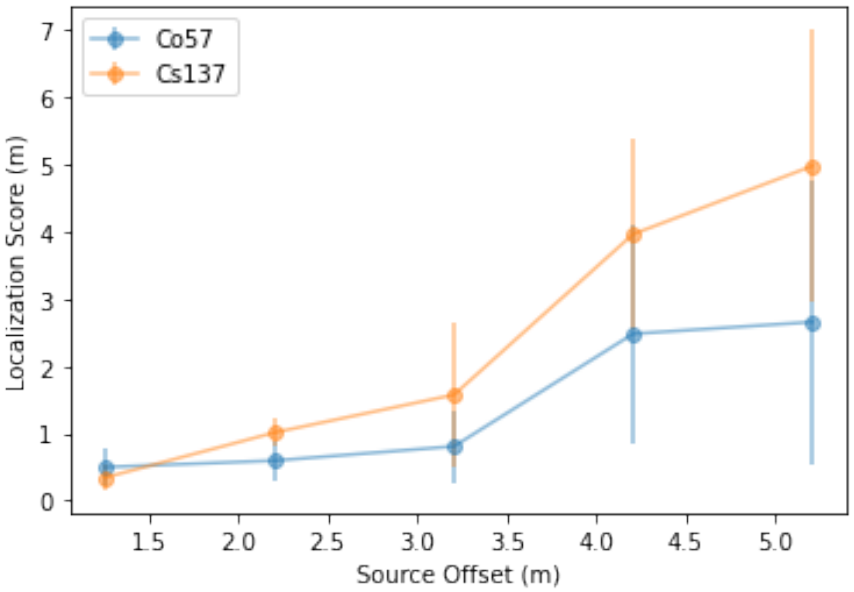


Figure 3.12: Localization performance with respect to source offset using 30 s measurements. Results between 95 μCi Co-57 and 113 μCi Cs-137 source are compared. See the text for analysis.

3.3.3 Integration Time and Detector Array Speed

Figure 3.13 compares localization results for a 113 μCi Cs-137 source at a 2.3 m source offset and a 81 keV energy threshold: the only difference between the results being time integration. The shorter integration time generated a better localization score and a more precise source position estimate as the 4 position estimates for the source average to an estimated position that is closer to the ground truth. The longer integration time generated a worse localization score only determining that the source was on the left side of the traveled path. The localization results across integration times are condensed into Figure 3.14 where these localization behaviors observed in Figure 3.13 could be generalized across the domain. Upon comparison between the top and bottom plots of Figure 3.14 which describe the detector array traveling at different speeds, motion blurring was observed to degrade localization performance of both integration times. It can be observed in the bottom plot that shorter integration times are more resistant to motion blurring effects on source localization results.

The observations thus far seem to support that low integration times lead to better source localization estimates; however, it is more accurate to say that lower integration times lead to favorable source localization estimates when counting statistics are sufficient. Figure 3.15 compares source localization error with respect to both integration time and energy threshold, where the top plot uses an 81 keV threshold and the bottom plot uses the photopeak counts for a Cs-137 source. The 81 keV threshold case has comparable performance between the integration times across all the source offsets with the exception of the 5.2 m source offset. The photopeak counts case has the longer integration time out performing the short integration time across all source offsets. The difference between these two input types is the magnitude of count rates involved: the photo peak count rates are roughly 10% of the 81 keV threshold counts where statistics greatly affects source position estimates.

Figures 3.16 shows localization results for a 113 μCi Cs-137 source, 81 keV threshold, 2.2 m source offset, and 0.2 s time integration. Figure 3.16 had the detector array traveling at 0.46 m/s in the top plot and 0.69 m/s in the bottom plot. When the localization

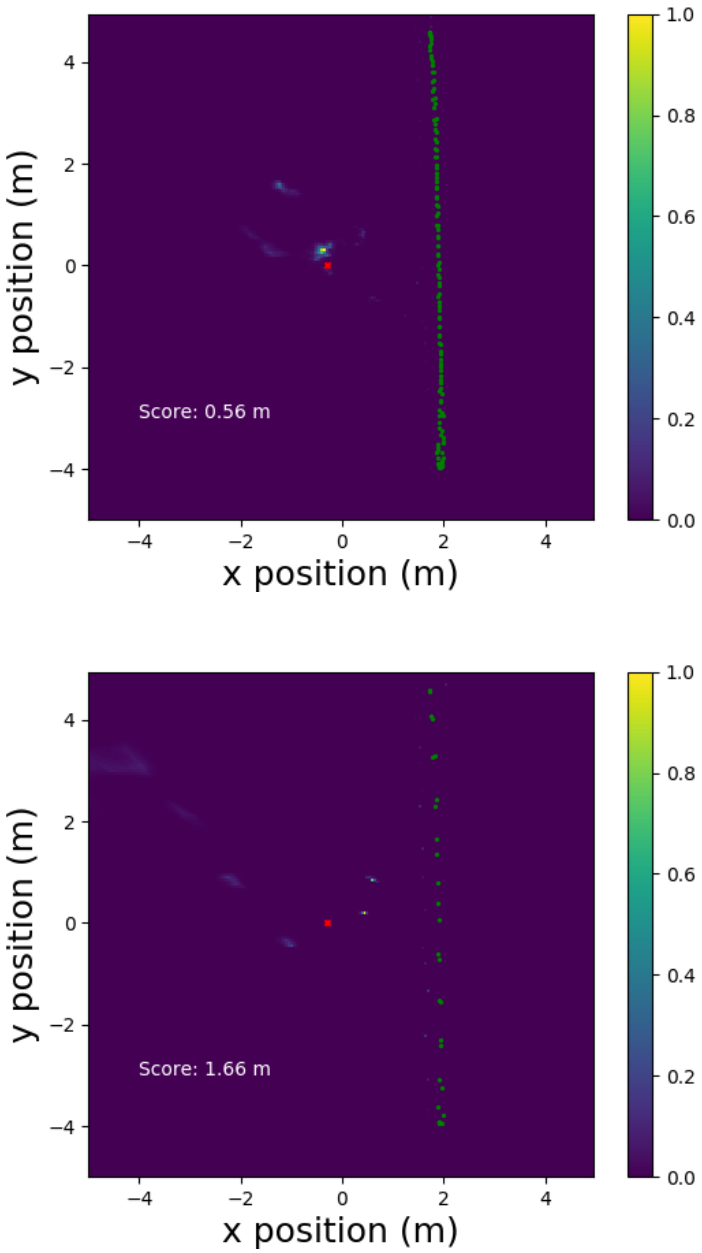


Figure 3.13: Sample of a source localization result. Red "x" denotes ground truth source position. Green dots denote detector array positions. The source was a 113 μCi Cs-137 source with a 2.3 m source offset. Detector array speed was at 0.69 m/s, and the net count rate was taken after a 81 keV energy threshold was applied. (Left) A 0.20 s time integration was used. (Right) A 1.00 s time integration was used. See the text for analysis.

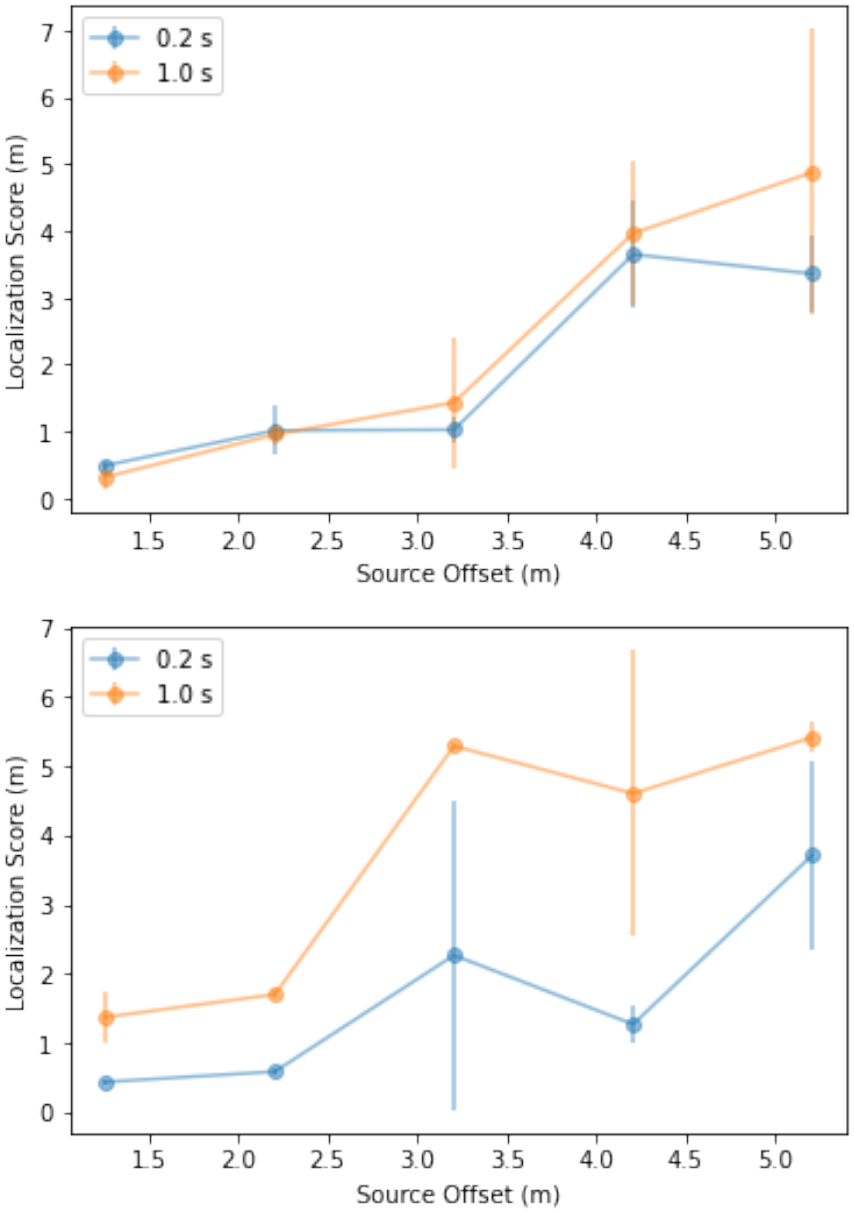


Figure 3.14: Localization performance with respect to source offset using 30s measurements, a 113 μCi Cs-137 source, and a 81 keV energy threshold. Results between 1.00 and 0.20 time integrations are compared. (Left) Detector array speed at 0.46 m/s. (Right) Detector array speed at 0.69 m/s. See the text for analysis.

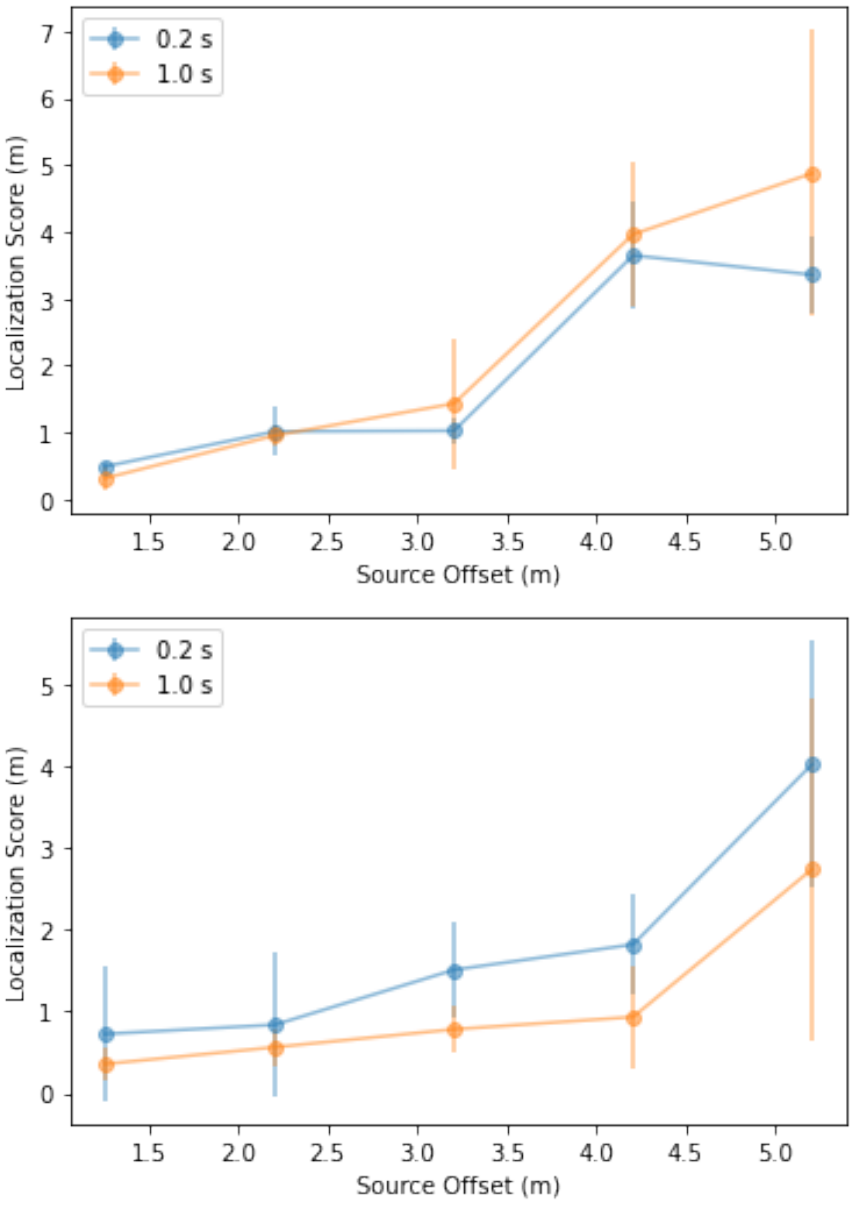


Figure 3.15: Localization performance with respect to source offset using 30s measurements and a 113 μCi Cs-137 source. Results between 1.00 and 0.20 time integrations are compared with the detector array traveling at 0.46 m/s. (Left) The energy threshold was set to 81 keV. (Right) Only Cs-137 photopeak counts were included. See the text for analysis.

results are condensed as in Figure 3.17, it was observed that slower speeds produce better localization results. This result reinforces that the decreasing motion blurring effects by decreasing detector array speed generates better localization results. Specifically, motion blurring occurs when there is a mismatch between the radiation transport model and what occurred during the experiment. Detector array movement during measurement periods, referred to as integration times in this work, was not captured in the radiation transport model described in 3.2.2. Reference 20 studied the improvements associated with including this detector movement within the radiation transport for a coded aperture system. To summarize, the effects of motion blur can be decreased in three ways: 1) decrease of time integration as done in Figure 3.14, 2) decrease of detector array speed as done in Figure 3.17, or 3) include the detector array movement within the radiation transport model as done in Reference [20]. All methods have the same net effect: the detector array position across the radiation measurement is more accurately represented in the radiation transport model, which consequently improves the source localization result. Note that the ANSI standard for walking speeds with backpack based systems is 1.2 m/s at a source offset at 2 m where motion blurring effects are expected to be more significant.

Another interesting trend is observed in Figure 3.17, where the higher detector array speeds yield more consistent source position estimates, where the uncertainty bars were smaller across all source offsets for the higher detector array speed. This is due to the repeated measurements of similar detector array positions associated with a higher detector array speed, the detector array path chosen in the experiment, and the measurement length chosen, all of which results in a more precise source localization result.

3.3.4 Energy Threshold

Localization tended to be better with lower energy thresholds when there was sufficient counting statistics. Figure 3.18 details the source localization performance with respect to inputs. The top plot had an integration time set to 1.0 s, where the counting statistics was sufficient to support a higher threshold of 122 keV or even Cs-137 photopeak counts. However, when the integration time decreased to 0.20 s, the lower energy thresholds of 32

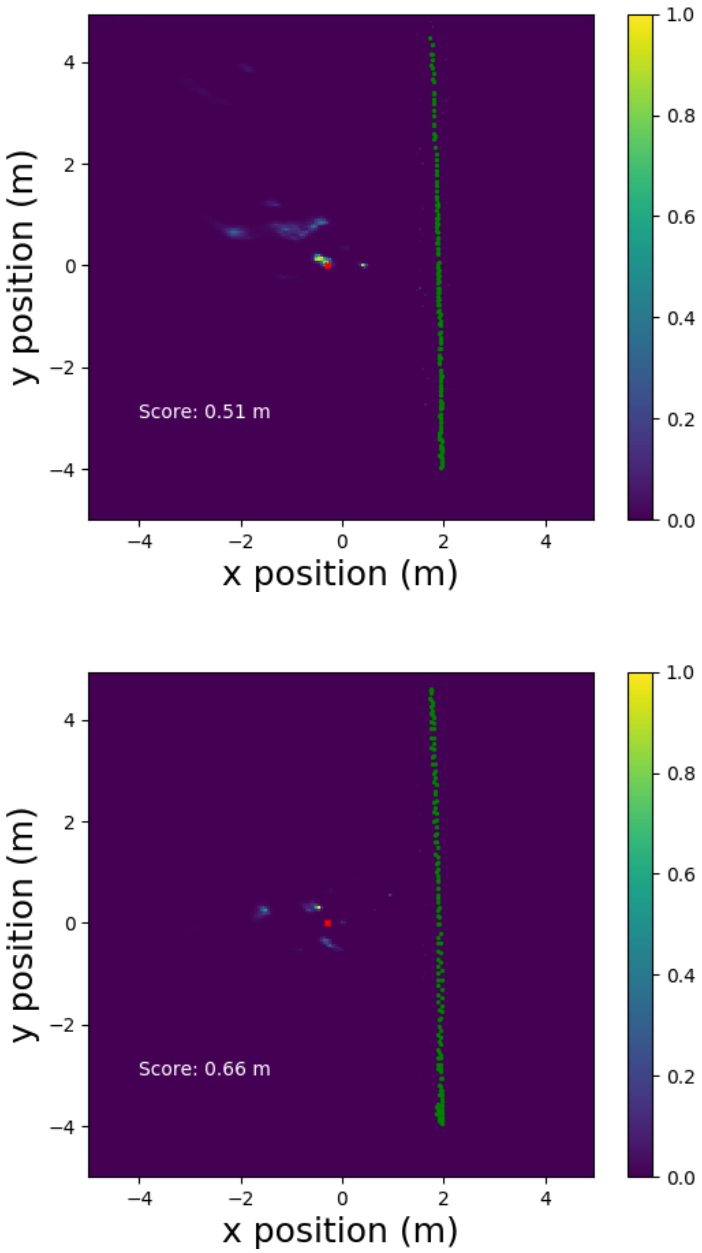


Figure 3.16: Sample of a source localization result. Red "x" denotes ground truth source position. Green dots denote detector array positions. The source was a 113 μCi Cs-137 source with a 4.2 m source offset, a 0.20 s integration time was used, and the net count rate was taken after a 81 keV energy threshold was applied. (Left) Detector array speed was 0.46 m/s. (Right) Detector array speed was 0.69 m/s. See associated text for analysis.

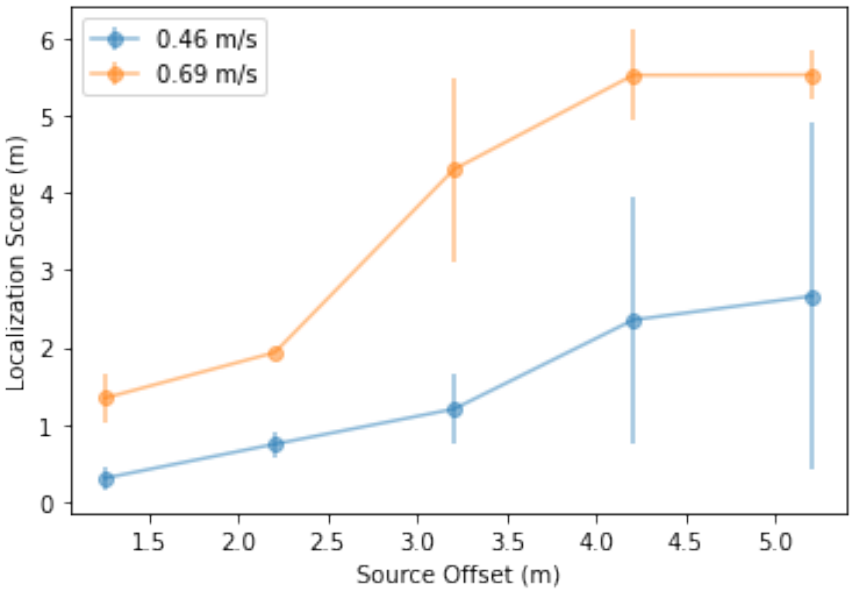


Figure 3.17: Localization performance with respect to source offset using 30s measurements. Results between 0.46 m/s and 0.69 m/s detector array speeds are compared. Source was a 113 μCi Cs-137 source with a 122 keV energy threshold and an integration time of 0.20 s. Refer to text for analysis.

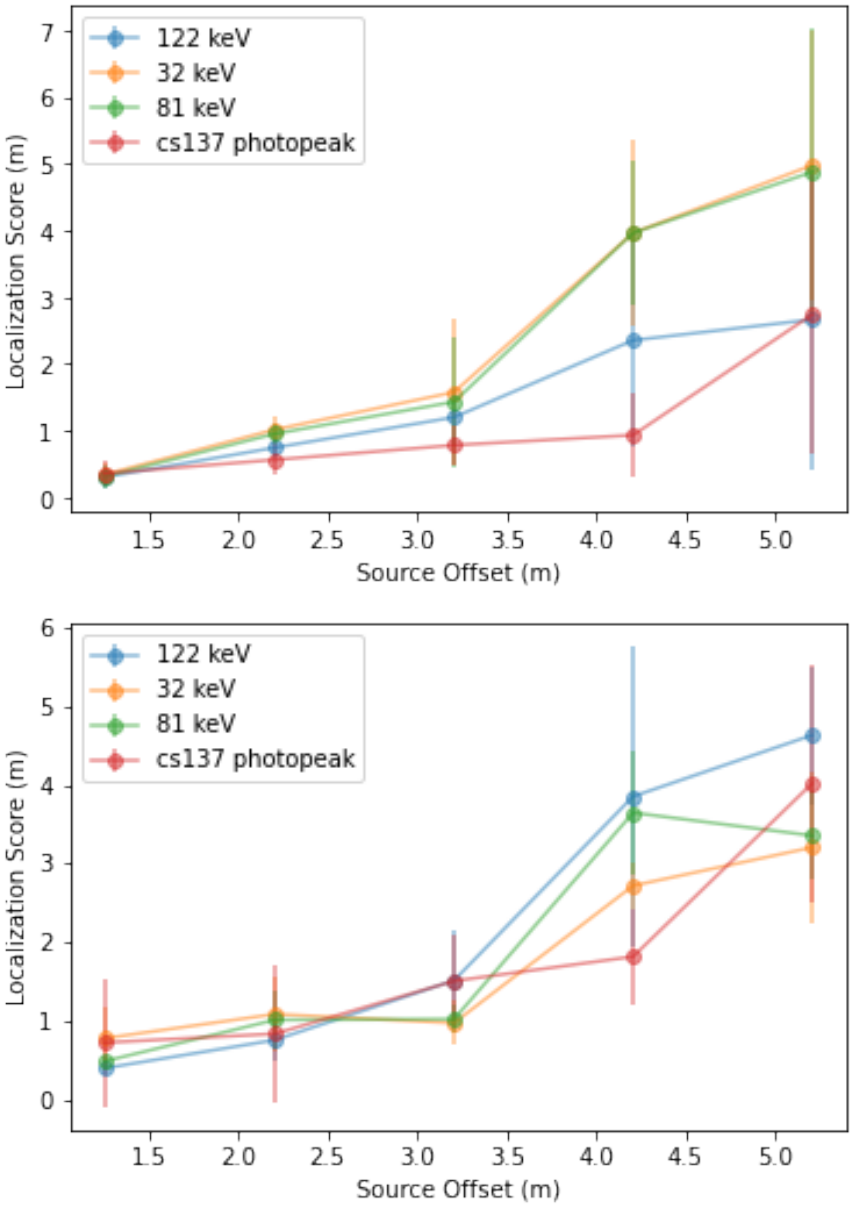


Figure 3.18: Localization performance with respect to source offset using 30 s measurements. Source was a 113 μCi Cs-137 source and the detector array's speed was 0.46 m/s. (Left) Integration time of 1.0 s. (Right) Integration time of 0.20 s. See the text for analysis.

keV and 81 keV corresponded to better performance. These observations are consistent with the previous analysis with respect to integration time and set energy threshold.

3.3.5 kSigma

To summarize, localization performance was studied as a function kSigma, which represents the measured counts above the expected background count rate. kSigma is borrowed from the radiation detection algorithm, as it represents the alarm level for a simple count rate based detection algorithm. Higher kSigma values denote a higher measured count rate, which correlates with a higher true positive rate for a given measurement. Figure 3.19 therefore shows the relationship of localization performance with respect to radiation detection confidence. The top plot considers an unrestrictive kSigma detection algorithm, where the measured counts from the majority of the energy spectrum is used. Note the improvement in localization performance when compared to the use of photopeak only counts in the bottom plot. This observation suggests that radiation signatures or features which are background resistant tend to lead to better localization performance.

3.4 Conclusions

The source localization performance for a wearable, backpack sized, and human portable detector array was characterized. This backpack was designed with directional capability for gamma sources of interest for nuclear security applications. Both experimental and operational variables were controlled to study their respective effects on localization performance. Variables included source offset, integration time, detector array speed, and source type. Key results include that a 95 μ Ci Co-57 source and a 113 μCi Cs-137 source could be localized to less than 1.0 m for source offsets less than 3.2 m. These results were obtained using an 81 keV threshold, an integration time of 0.2 s, and a speed of 0.46 m/s. Furthermore, it was observed that motion blur effects can be decreased by decreasing the integration time and slowing detector array speed, both of which improve localization performance.

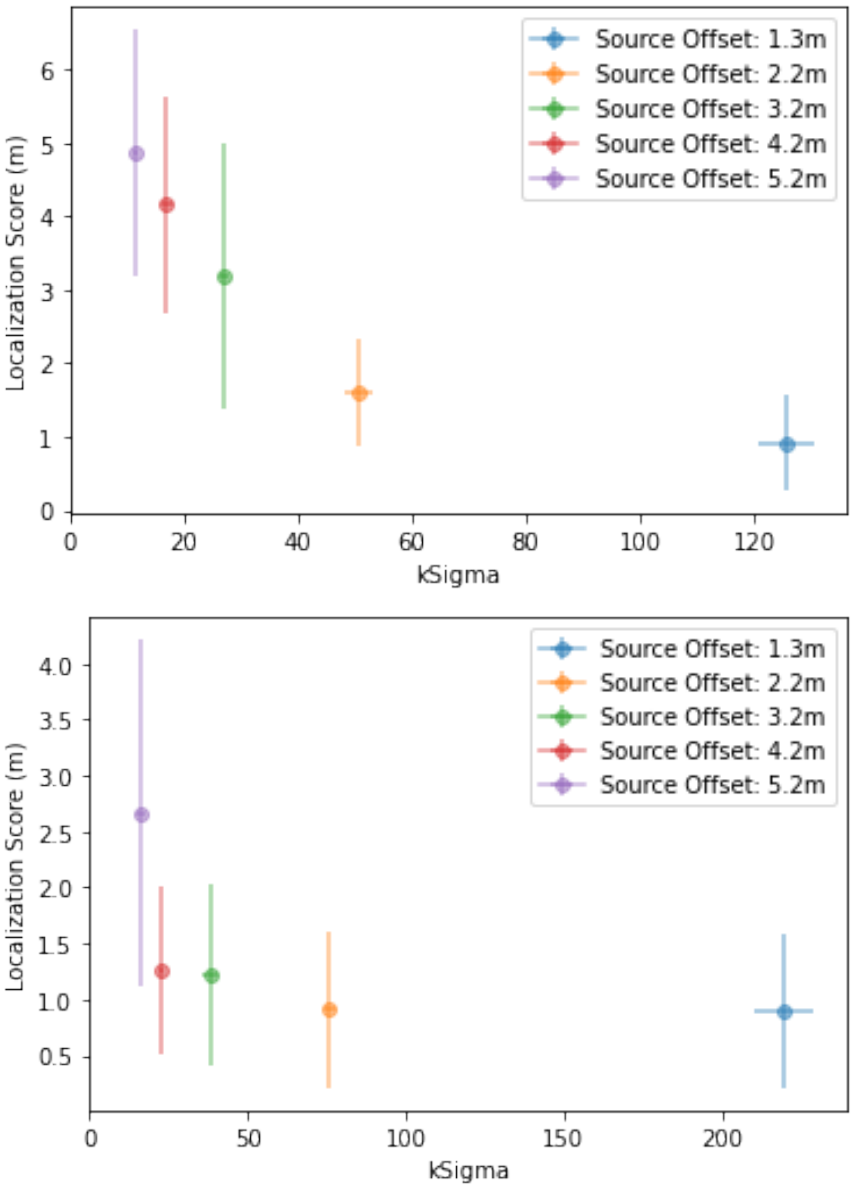


Figure 3.19: Localization performance with respect to kSigma. Measurement time was 30 s with an integration time set to 1.0 s. (Left) The energy threshold was set to 32 keV, where the entire energy spectrum is considered. (Right) Input type was photopeak counts, where fewer counts would be considered NORM, hence the higher kSigma.

Future work includes building a synthetic test bed based on the measurements taken with this system, such that arbitrary variation in experimental scenario can be performed. Variables such as detector array path, detector array orientation, speed, source offset, source type, etc. can be infinitely varied. This capability is similar to what is demonstrated in Reference [29]. Furthermore, investigation of localization performance with the inclusion of RGB video data is of interest.

3.5 Acknowledgements

This material is based upon work supported by both the Department of Homeland Security and Department of Energy National Nuclear Security Administration under Award Numbers DHS-15-DNDO-077-001, DE-NA0002576, and DE-NA0003180. This report was prepared as an account of work sponsored by an agency of the United States Government. Neither the United States Government nor any agency thereof, nor any of their employees, makes any warranty, express or implied, or assumes any legal liability or responsibility for the accuracy, completeness, or usefulness of any information, apparatus, product, or process disclosed, or represents that its use would not infringe privately owned rights. Reference herein to any specific commercial product, process, or service by trade name, trademark, manufacturer, or otherwise does not necessarily constitute or imply its endorsement, recommendation, or favoring by the United States Government or any agency thereof. The views and opinions of authors expressed herein do not necessarily state or reflect those of the United States Government or any agency thereof.

Chapter 4

Fusion of Radiation and Video Data Modalities

4.1 Introduction

Consider a hypothetical scenario where an operator is guarding a venue such as Grand Central Station from nuclear and radiological threats. This operator is equipped with a backpack-sized, closely-packed, radiation detector array, such as the one shown in Figure 4.1, which suddenly detects a non-natural radiation source within the vicinity. There are numerous potential fixed and dynamic locations for a source: a luggage case, a person's jacket pocket, and a trashcan are many examples. Furthermore, the scene only includes a fraction of the scene to clear: a similar scene can be viewed behind, to the left, and to the right of the operator.

Traditionally, the challenge of source localization consists of finding a fixed, non-natural radiation source with a set of field measurements. Examples of finding a fixed radiation source in the literature include: the use of a network of radiation sensors [8, 18], Compton imagers (CIs) [40], coded aperture imagers (CAIs) [45], and, the most akin radiation measurement system to this work, the use of roaming closely packed detector arrays [7, 23, 29, 13]. These references vary in source strengths, on the order of hundreds of μCi to tens of mCi, and distances, on the order of meters to 100s of meters, of interest.



Figure 4.1: WIND Backpack Detector Array. (Left) Concealed backpack configuration. (Right) Radiation detector array packaged within backpack.

Source localization has been done on moving with sources with known source movement and only radiation data. Ziock et al. showed that source localization results improve due to suppression of CAI imaging artifacts through the perspectives gained in relative movement between the source and CAI [46]. With similar source distances and source strengths to our work, Kaye et al. required enough measurement time to acquire 10,000 counts on a CAI system with an 85 μCi Cs-137 at a distance of approximately 1 m [24]. Source movement in their work was actually implemented as measurement dwells at 9 discrete locations [24]. Jarwoski et al. extended the work by generating imaging results for multiple sources with simple continuous motion with a fixed distance of 1.2 m and a fixed angular velocity [22]. Results from both References 24 and 22 demonstrated imaging results on moving sources and fixed CAI systems; however, source movement was known a priori.

The goal of this work is to demonstrate that video data can be both processed and fused with radiation directionality estimates to assign source carrier probabilities (SCPs) to potential moving targets in near real-time in the context of a wearable system. The key contribution is that the video data processing algorithms would infer arbitrary object movement, which extends the simple (compared to this work) and known a priori source movement explored in References 24 and 22. Radiation directionality has been demonstrated to work on moving sources using short time integrations [44, 5]; however, correlating target movement from video data streams with time series radiation measurements would provide actionable information to operators as potential targets are evaluated by their SCPs. The work presented in this paper describes the general method, demonstrates its capability, and quantifies its performance. This work determines which moving target is carrying the source using data fusion mainly through the exploitation of the angular response of a closely packed, wearable radiation detector array using radiation directionality [5]. This work also addresses scenarios where the target is undergoing complex and arbitrary movement where detected objects could occlude one another.

4.2 Methodology

4.2.1 Data Fusion Algorithm

Our data fusion methodology brings together algorithms developed for directionality based upon close-packed detector array data with algorithms for object detection and tracking based upon simple RGB camera data. Directionality refers to direction estimates to either a radiation source from radiation measurements or detected objects from the video data stream. Directionality in both contexts are relative to the detector array's orientation using measurements less than one second. The flow chart in Figure 4.2 serves as a high level overview for the data fusion strategy. The red ellipses denote measured data, the blue blocks denote algorithm modules, and the blue ellipses denote results generated from a module. The flow chart describes performing directionality, tracking directionality histories, and then correlating histories, all applied to both radiation and video data modalities.

The radiation directionality module makes estimates using one-second net count rate measurements. Briefly summarizing the algorithm, the directionality module uses Maximum Likelihood Estimation to calculate probabilities for a number of directions using the angular response template shown in Figure 4.3. Figure 4.4 is a confusion plot which describes directionality performance for each angular group, which this work exploits as probability distributions. The x-axis can be interpreted abstractly as radiation inputs without the direction estimation label: net count rates from each detector after one second that look similar to the labeled angle. The y-axis represents a probability distribution denoting where the source is actually located. When the source is located at 180^o, the bottom plot of Figure 4.4 shows that the directionality algorithm will predict source directions from 140^o to 220^o. The count rate profile is similar within this range of angles making it hard to distinguish one angle from another, as suggested by Figure 4.3. In contrast to when the source is located at 135^o, the directionality algorithm predicts with a probability distribution spanning from 130^o to 140^o where the count rate profile is relatively unique.

Concurrently, video data is collected using a web camera at a rate of 5 frames per second (fps) and is fed into the video object detection (VOD) algorithm, You Only Look Once (YOLOv3) [36]. YOLOv3 is a simple video object detection algorithm which resizes the

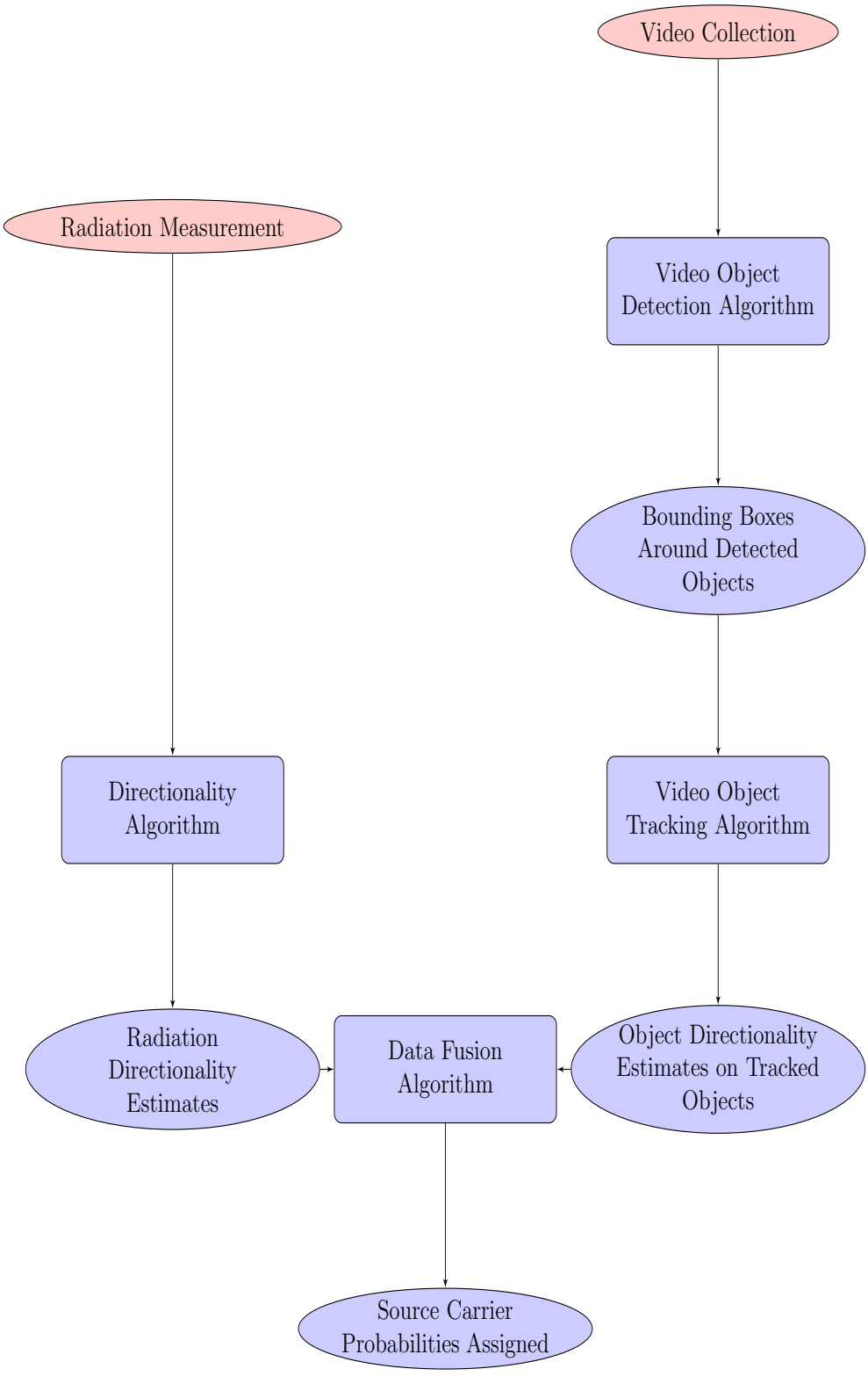


Figure 4.2: Data fusion workflow overview. Red ellipses denote measured data, blue blocks denote algorithm modules, and blue ellipses denote output generated from algorithms.

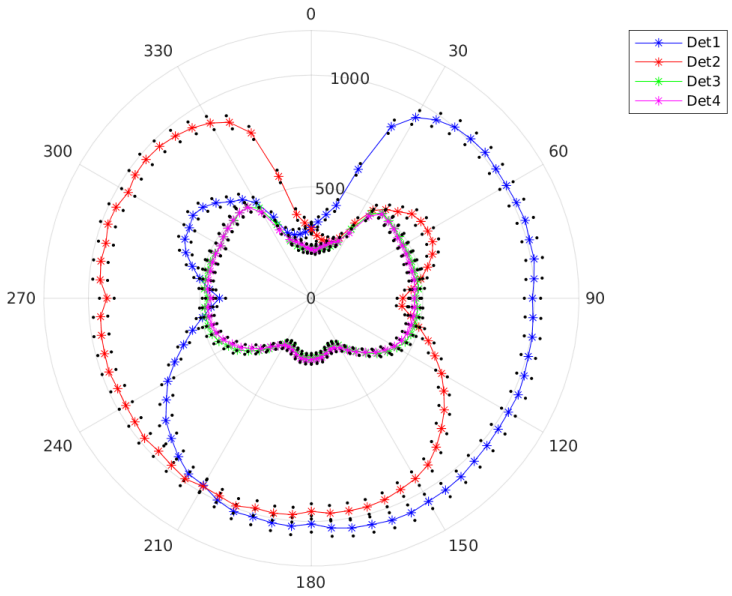


Figure 4.3: (Measured angular response for a 113 μCi Cs-137 source at 172.4 cm. The polar angle represents source position in degrees, while the radius denotes magnitude of the net count rate (cps) after background subtraction and an 81 keV threshold is applied.

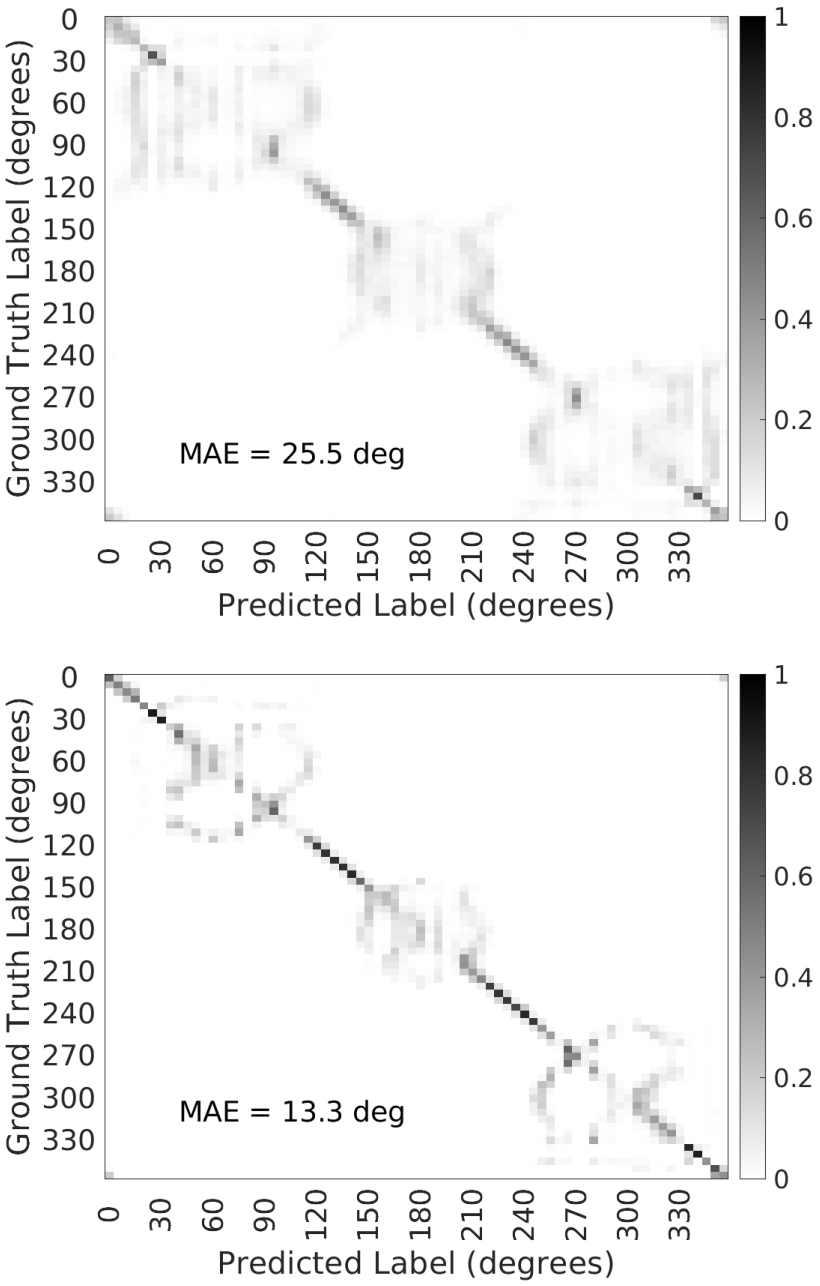


Figure 4.4: Directionality performance while trained with a 113.3 μCi Cs-137 source at 172.4 cm while observing a 113.3 μCi Cs-137 at 172.4 cm for the detector array used in this work. X-axis represents directionality estimates. Y-axis represents ground truth source angle. Color denotes probability of classification. Every pixel describes an angle spanning 5 degrees. See associated text for more detail. (Left) Directionality performance with an integration time of 0.2 s. (Right) Directionality performance with an integration time of 1.0 s.

input image, runs a convolutional neural network which "simultaneously predicts multiple bounding boxes and class probabilities for those boxes" [36]. Using this unified approach, Redmon et al. were able to demonstrate "the fastest general-purpose object detector in the literature and YOLO pushes the state-of-the-art in real-time object detection" [36]. YOLOv3 was chosen for two main reasons: 1) it's a fairly accurate object detector, 2) a real time implementation is possible, and 3) object detections are generalizable (i.e. people, trash bins, cars, bicycles) such that retraining the network for every environmental context (i.e. baseball stadium, concert venue, mall) is not necessary. At this point, one could extract video object directionality directly from the VOD; however, YOLOv3 detects objects in a single image in a time independent manner where objects detected in subsequent frames have no relation to the current frame. Consequently, the VOD in this work is used once every second.

This work uses SiamFC, a fully-convolutional siamese network, for the Video Object Tracking (VOT) algorithm [4]. Video object tracking is the act of understanding how a detected object in an image moves in subsequent frames. SiamFC poses VOT as a similarity problem, where two images are compared and rated in similarity. SiamFC specifically uses two seperate networks, one to understand the detected object's representation and another which convolves the detected object's image with the subsequent image to understand the detected object's translation [4]. The translation which scores highest in the similarity metric is the translation that most likely occurred. SiamFC was specifically chosen as the "method improves over recent state-of-the-art real-time trackers ... Moreover, it outperforms most of the best methods in the challenging VOT-15 benchmark, while being the only one that achieves frame-rate speed" [4].

The VOT is employed to associate detected objects and understand their movement throughout motion sequences. This addition grants two advantages. The first advantage allows tracked object angle histories to now be logged for each detected object. This allows radiation directionality estimates to accumulate such that assigned SCPs can be appropriately calculated. The second advantage refers to video object occlusion where one object within a video sequence partially or completely obscures another. Without a VOT algorithm, the tracked angle history would be lost and the accumulated SCP would reset

to zero. The introduction of a VOT allows a chance to salvage the tracked object's angle history and accumulated SCP. In this work, the VOT is used four times every second in order to account for movement between radiation directionality estimates.

The VOD and VOT algorithms represent the most computationally expensive operations in the data fusion work presented. This work used an implementation on a virtual machine running Ubuntu 64-bit 16.04 with 16GB of memory. The virtual machine ran on a Macbook Pro packaged with a 2.4 GHz Intel i9 processor and an AMD Radeon Pro 5500M 8 GB graphics processing unit (GPU). Video was taken at 5 frames per second. The VOD, YOLOv3, took 1.04 $\pm$ 0.07 s to draw boundary boxes given an image. The VOT, SiamFC, took 3.9 $\pm$ 0.9 s to track each object in the 4 subsequent frames. These results show that a real-time implementation of the VOD and VOT algorithms is almost possible with this current setup. Ultimately, this suggests that a real-time implementation would be possible with a laptop running the VOD and VOT natively on its own operating system, especially with a better GPU running CUDA drivers.

With radiation directionality and video object directionality completed, the data fusion module (DFM) uses an empirical application of Bayes' theorem, $p(\Theta_j|X) = \frac{p(X|\Theta_j)P(\Theta_j)}{\sum_{i=1}^{g} p(X|\Theta_i)P(\Theta_i)}$, to combine both data modalities. Let X be a set of m radiation measurements, such that $X = \vec{x_1}, \vec{x_2}, \ldots, \vec{x_m}$. Let Θ be the angle history of a tracked object indexed by j, where $\Theta_j = \theta_1, \theta_2, \ldots, \theta_n$ and n denotes the length of the object's angle history. The posterior probability is $p(\Theta_j|X)$, which describes the probability of tracked object j with an angle history Θ is the source carrier given a set of radiation measurements, X. The probability density function (pdf), $p(X|\Theta_j)$, is the probability of a source being located at a specific direction, which is summarized by the probabilities within the confusion matrices shown in Figure 4.4. The prior probability, $P(\Theta_j)$, is interpreted as the probability that object j with angle history Θ could be a source carrier. In this work, all detected objects are automatically considered as a potential source carrier, so $P(\Theta_j)$ is always one. Finally, the evidence term in the denominator compares tracked object j with angle history Θ to all currently tracked objects by summing across all g tracked objects. Note that this work assumes a single non-natural source.

Data fusion occurs by constraining the pdf of Bayes' theorem to objects that existed at the intersection of angles for a given time history. The assumption is made that one of the tracked objects is carrying the source that was observed in the radiation measurements. Furthermore, the source track is constrained to that tracked object's movement throughout some time period. The data fusion module's (DFM) rolling window was set to 5 seconds, and object 1's position was measured to be 5^o, 25^o, 345^o, 300^o, and 315^o for that rolling window period. With that object's history, only radiation directionality probabilities (pdf values of $p(X|\Theta)$) given at 5^o, 25^o, 345^o, 300^o, and 315^o would be accrued: $p(X|\Theta_1) = p(\vec{x_1}|5^o) + p(\vec{x_2}|25^o) + p(\vec{x_3}|345^o) + p(\vec{x_4}|300^o) + p(\vec{x_5}|315^o)$. Each element of the summation is ultimately assigned by the radiation directionality algorithm; however, note that this assignment is also dependent upon information from the video object tracking algorithm for angle histories Θ. This process is repeated for the g tracked objects, then compared to one another such that the highest value is the most likely source carrier.

4.2.2 Experimental Setup

The experimental setup involved in the dynamic source localization is given in Figure 4.5. A phantom's torso is set on top of a table to mimic an operator monitoring a chokepoint. A radiation detector array is placed behind the phantom to simulate the radiation detector array being worn as a backpack. This array consisted of 2 NaI(Tl) ($\rho = 3.67$ g/cc) of 54 × 54 × 152 mm dimension and 2 Li-6 enriched CLYC(Ce) of 54 × 54 × 76 mm dimension. The CLYC(Ce) ($\rho = 3.31$ g/cc) detectors are optically separated and stacked on top of another to yield the same dimension, as each of the NaI(Tl) detectors as CLYC(Ce) aren't grown in sizes larger than 76 mm. Taped chest height to the phantom is a Spedal 1080p webcam. This webcam has capabilities akin to cameras worn by law enforcement: a field of view of 120^o and video run at 5 frames per second.

A Velodyne VLP-16 LIDAR is positioned in front of the phantom to measure the ground truth source position every second. In front of this setup, there are 3 experimentalists instructed to follow a predetermined path for roughly 500 seconds. One of the three experimentalists is carrying either a 113 μCi Cs-137 or 95 μCi Co-57 source. The point clouds acquired by the LIDAR were not used to calculate the source carrier probabilities,

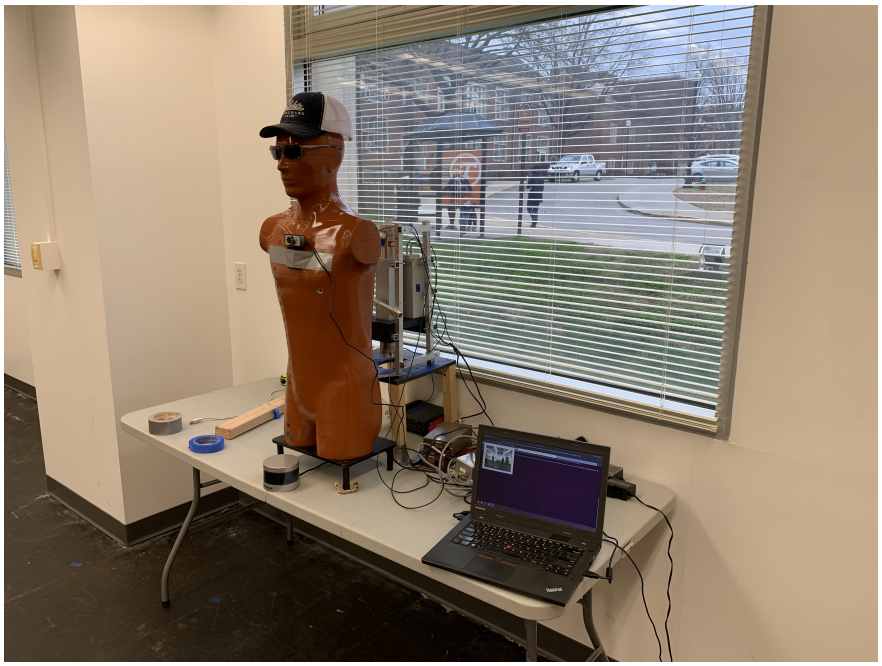


Figure 4.5: Dynamic source localization experimental setup.

but the source was manually segmented to the experimentalist's hand in the acquired pointclouds. The majority of the source's ground truth positional uncertainty was due to time synchronization uncertainty of ±0.1 s between the LIDAR, video, and radiation data modalities. Given the average experimentalist speed in the worst direction, the ground truth source position uncertainty of ±5 cm which translates to an angular uncertainty of 0.9 ± 0.3^o. The video and LIDAR sensors were calibrated by hand with an additional positional uncertainty of 5 ± 1^o, which calculates to a total uncertainty of 6 ± 1^o for video directionality estimations upon inclusion of the time synchronization uncertainty.

4.3 Results

4.3.1 SCP Calculation Example

An excerpt from the acquired results is given in Table 4.1 to elaborate on the data fusion strategy. The values which relate to objects 1, 5, and 6's angular track histories are found in the columns labeled with $\Theta_1, \Theta_5, \Theta_6$. The values which relate to the objects 1, 5, and 6's current angle are found in columns labeled with $\theta_1, \theta_5, \theta_6$. The PDF and SCP values are calculated using directionality information from the radiation and video sensors. The ground truth (GT) angle is taken from the LIDAR sensor. The angle 0^o is defined as directly in front of the operator. The pdf value columns are calculated by mapping object positions to the radiation directionality pdfs, such as what is shown in Figure 4.4. For example, objects 1, 5, and 6 are located at 17^o, -36^o, and -1^o at t=5.6 s, respectively. The directionality algorithm determines that objects 1, 5, and 6 at those directions have a pdf values of 0.53, 0.00, and 0.00 from the radiation data stream in that second. The SCP values denote the probabilities that a tracked object carried the radiation source given its respective movement history over the past 5 seconds, from t=0.6 s to t=5.6 s. The SCP is calculated by taking the ratio of the sum of a given tracked object's pdf values and the sum of all tracked objects' pdf values, both of which are over the past 5 seconds. At t=5.6 s, the SCPs for Objects 1, 5, and 6 are 0.68, 0.18, and 0.14, respectively. From the video stream and the radiation measurement history, the SCP can be calculated which determines that Object 1 is the most likely source

Table 4.1: Subset of data fusion results. The row in dark gray is the specific time step mentioned in the text. PDF values denote the single time step probabilities as given by the radiation directionality algorithm for the tracked object. SCP values denote the source carrier probabilities given the tracked object directionality histories from both the radiation and video data modalities. The PDF values of the rows in light gray are used to calculate the SCP value of the row in dark gray.

Time (s)	GT Source Angle (^{o})	θ_1 PDF	Θ_1 SCP	θ_1 Angle (^{o})	θ_5 PDF	Θ_5 SCP	θ_5 Angle (^{o})	θ_6 PDF	Θ_6 SCP	θ_6 Angle (^{o})
0.0	-16	0.10	0.13	-1	0.00	0.00	36	0.72	0.87	-13
0.2	-16	0.10	0.13	-1	0.00	0.00	35	0.72	0.87	-13
0.4	-16	0.10	0.13	-1	0.00	0.00	33	0.57	0.87	-10
0.6	-15	0.11	0.13	-1	0.00	0.00	32	0.49	0.87	-8
0.8	-14	0.15	0.13	-1	0.00	0.00	29	0.48	0.87	-8
1.0	-13	0.18	0.14	-1	0.00	0.00	26	0.43	0.86	-7
1.2	-12	0.22	0.15	-1	0.00	0.00	22	0.42	0.85	-7
1.4	-12	0.22	0.16	-1	0.00	0.00	17	0.45	0.84	-8
1.6	-10	0.29	0.17	-1	0.03	0.00	13	0.00	0.00	-8
1.8	-8	0.36	0.19	-1	0.12	0.01	10	0.00	0.00	-8
2.0	-6	0.43	0.21	-1	0.30	0.03	5	0.00	0.00	-8
2.2	-5	0.47	0.23	-1	0.43	0.05	2	0.00	0.00	-8
2.4	-3	0.57	0.25	0	0.60	0.08	0	0.00	0.00	-8
2.6	0	0.70	0.27	0	0.65	0.11	-1	0.00	0.00	-8
2.8	2	0.47	0.29	5	0.52	0.14	-2	0.00	0.00	-8
3.0	4	0.43	0.30	6	0.40	0.16	-3	0.00	0.00	-8
3.2	7	0.43	0.32	7	0.24	0.17	-5	0.00	0.00	-8
3.4	10	0.47	0.34	8	0.07	0.17	-10	0.23	0.49	0
3.6	11	0.51	0.36	9	0.04	0.18	-11	0.17	0.46	-1
3.8	12	0.58	0.39	10	0.02	0.18	-12	0.14	0.44	0
4.0	12	0.58	0.41	10	0.00	0.18	-17	0.13	0.41	-1
4.2	13	0.70	0.44	12	0.00	0.18	-18	0.09	0.38	-1
4.4	14	0.80	0.48	13	0.00	0.18	-19	0.04	0.34	-1
4.6	16	0.86	0.52	14	0.00	0.18	-23	0.00	0.30	-1
4.8	17	0.86	0.56	15	0.00	0.18	-27	0.00	0.27	-1
5.0	19	0.70	0.59	16	0.00	0.18	-29	0.00	0.23	-1
5.2	20	0.64	0.63	16	0.00	0.18	-33	0.00	0.19	-1
5.4	22	0.53	0.65	17	0.00	0.18	-33	0.00	0.16	-1
5.6	22	0.53	0.68	17	0.00	0.18	-36	0.00	0.14	-1
5.8	22	0.53	0.70	17	0.00	0.18	-37	0.00	0.11	-1
6.0	21	0.57	0.73	17	0.00	0.18	-38	0.00	0.09	-1
6.2	21	0.57	0.75	17	0.00	0.18	-37	0.00	0.07	-1
6.4	21	0.57	0.77	17	0.00	0.19	-36	0.00	0.04	-1
6.6	21	0.57	0.78	17	0.00	0.18	-37	0.00	0.04	-1
6.8	20	0.62	0.78	17	0.00	0.17	-37	0.00	0.04	-1
7.0	20	0.62	0.80	17	0.00	0.16	-36	0.00	0.04	-1
7.2	20	0.62	0.82	17	0.00	0.14	-37	0.00	0.04	-1
7.4	20	0.62	0.85	17	0.00	0.11	-36	0.00	0.05	-1
7.6	20	0.62	0.88	17	0.00	0.08	-37	0.00	0.05	-1
7.8	21	0.57	0.91	17	0.00	0.05	-37	0.00	0.05	-1
8.0	21	0.57	0.93	17	0.00	0.02	-37	0.00	0.05	-1

carrier; as such, the source angle deviation from ground truth is found to be 3^o; the correct object was identified at t=5.6 s.

4.3.2 DFM Scenario Commentary

Snapshots of the DFM's output are shown in Figures 4.6, 4.7, and 4.8. These snapshots span from 17 minutes, 51 seconds (17:51) to 18:24 (18:24) where objects are labeled with their respective SCPs over the 33 second video segment. The bounding boxes are drawn by the VOD algorithm, where each drawn boundary box is assigned an ID number. These objects are tracked from the VOT algorithm in subsequent frames, and the DFM combines both the radiation video data to calculate each object's SCP, noted by "P:". Finally, the green dot shows the ground truth source location in degrees as seen by the LIDAR measurement, where the source lies along the vertical axis denoted by this green dot. The green dot lies along one dimensional axis along the horizontal of the image, as only the coordinates parallel to the ground were used to calculate the angle.

Figure 4.6 describes a scenario where the source is transfered from one experimentalist to another and how the SCP changes as a function of time. The top of Figure 4.6 has the experimentalist in flannel carrying the 113 μCi Cs-137 source but is about to pass it to the experimentalist in orange. Note that currently, the flannel experimentalist's SCP is highest. After the orange experimentalist takes possession of the source 2 s later, the SCP score from the experimentalist wearing flannel is transferring to the experimentalist wearing orange as shown in the middle of Figure 4.6. Four seconds after the experimentalist orange takes position of the source, his SCP increases to 0.99 at the bottom of Figure 4.6.

Figure 4.7 studies the SCP changes after an occlusion event where all experimentalists block each other from view and the true target is the furthest from the camera. The top figure shows that the SCP for the experimentalist wearing orange is highest before the occlusion event at 17:56. From this point, the orange experimentalist will move from left to right. The middle of Figure 4.7 describe the results soon after the occlusion event at 18:05. Note that all of the experimentalists' identities have changed (for example, the experimentalist wearing orange's ID had changed from ID:3 to ID:1), which means that the VOT algorithm had failed to account for these objects during the video object occlusion event. Furthermore, the SCP

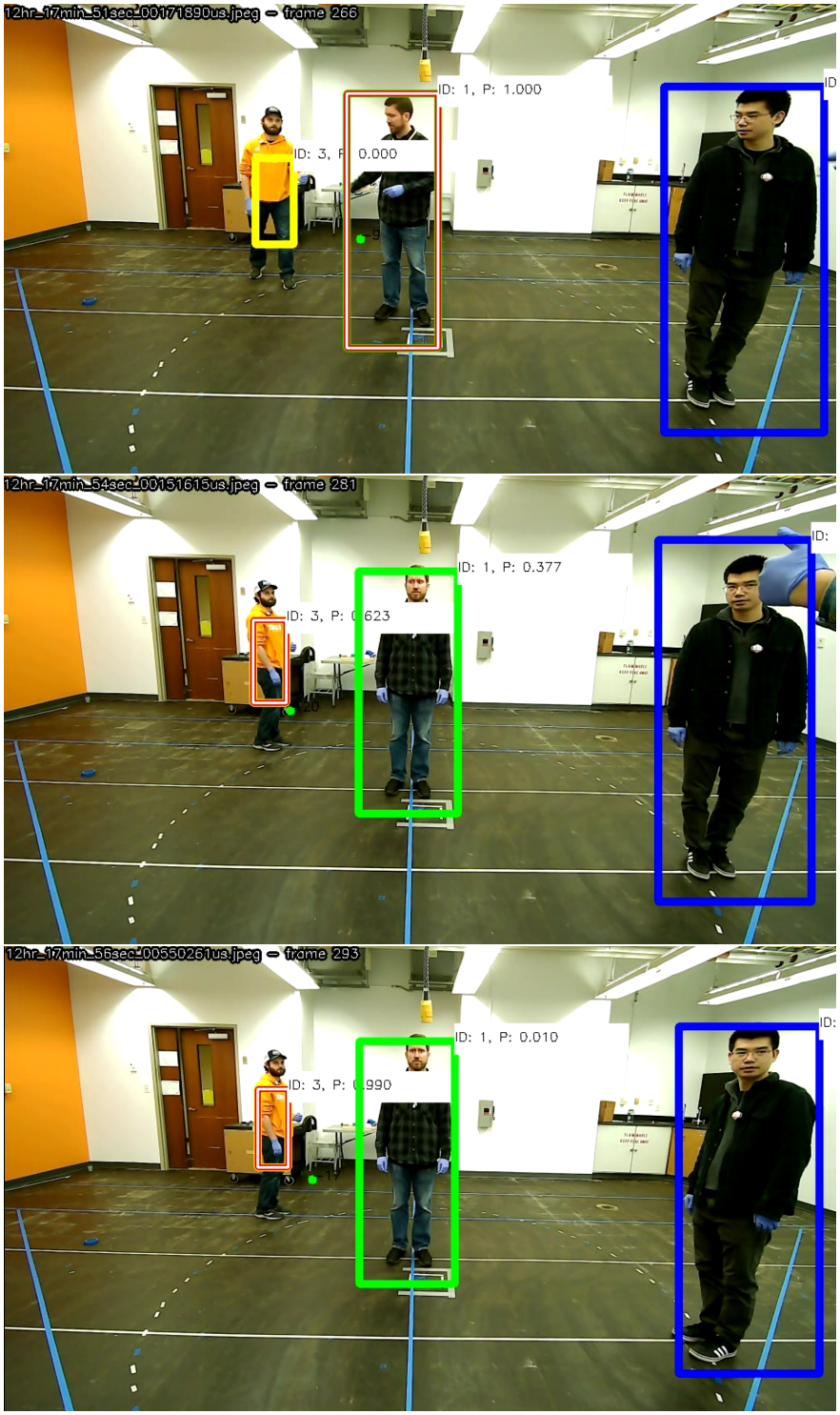


Figure 4.6: Source transfer scenario. (Top) DFM output at 17:51 where the experimentalist in the flannel shirt is carrying the 113 μCi Cs-137 source. (Middle) Fusion output at 17:54 where the experimentalist in orange now carries the source. (Bottom) Fusion output at 17:56. See the text for analysis.

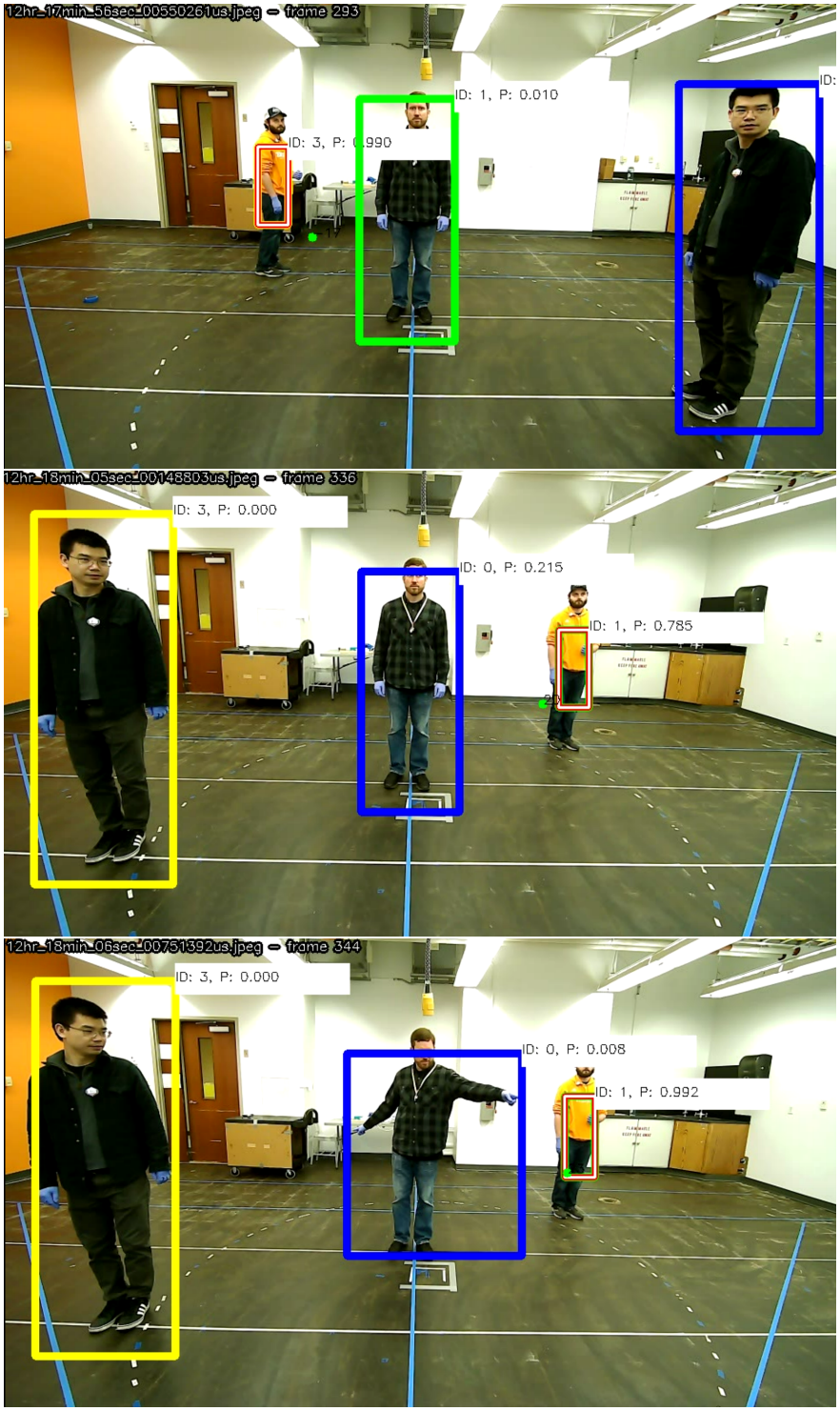


Figure 4.7: Object occlusion scenario, where the true target is the furthest away. (Top) Fusion output at 17:56, before the occlusion event. The experimentalist in orange is carrying the 113 μCi Cs-137 source. (Middle) Fusion output at 18:05. (Bottom) Fusion output at 18:06, after the occlusion event. See the text for analysis.

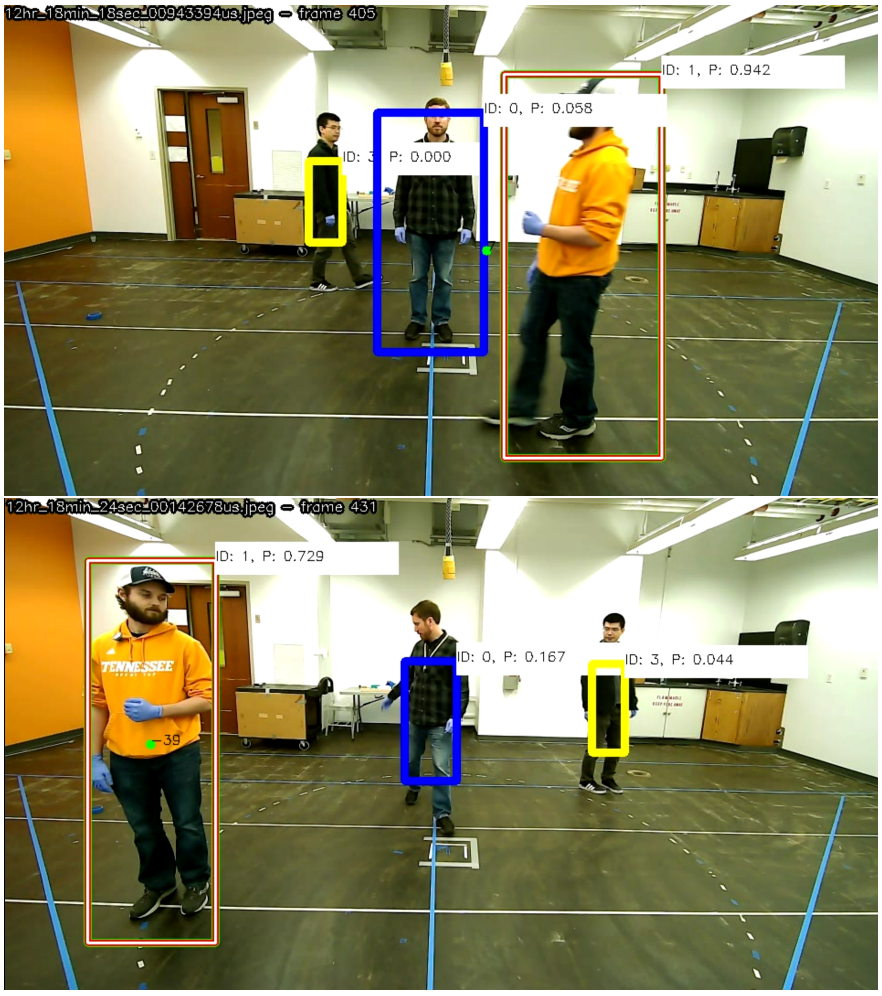


Figure 4.8: Object occlusion scenario, where the true target is the closest person. (Top) Fusion output at 18:18, before the occlusion event. The experimentalist in orange is carrying the 113 μCi Cs-137 source. (Bottom) Fusion output at 18:24, after the occlusion event. See the text for analysis.

is shared between the experimentalists in flannel and orange due to similar radiation and video directionality histories during the occlusion event. The bottom of Figure 4.7 shows the results at 18:06, where more evidence is collected to confirm that the orange experimentalist is carrying the source.

Figure 4.8 also studies the SCP changes during an occlusion event, but this time with the true target at the very front. The top figure shows the results at 18:18, right before the occlusion event. The orange experimentalist is carrying the source and is moving right to left. The bottom of Figure 4.8 are the results after the occlusion event at 18:24. This time, VOT successfully tracked all three objects as none of the identification numbers had changed. Furthermore, the SCP is still highest on the experimentalist wearing orange.

4.3.3 DFM Performance Summary

The directionality results from data fusion were compared to the radiation only data in Figure 4.9. Again, ground truth information was acquired from LIDAR pointcloud data which was manually segmented at the source position every 1 s, but linearly interpolated. The top of Figure 4.9 summarizes the directionality performance of the 113 μCi Cs-137 source when only radiation data is used determine the source carrier. A Mean Absolute Error (MAE) of 19 ± 17^{o} was measured in this scenario. The observed fluctuations are due to directionality estimates being made with only 1 s of radiation measurements, where estimates are made independent from one another. With such a short measurement time, the counting statistics are insufficient to get accurate radiation directionality estimates, especially when the source is further away from the detector array.

The bottom of Figure 4.9 summarizes the results obtained by using both the video and radiation data to determine which agent is carrying the 113 μ Cs-137 source. The fluctuations seen in the bottom plot are due to instances of misattributing the source carrier. For example, the large deviations from t=15 s to t=28 s were occlusion events while the experimentalists were getting in position. The large deviation at t=36 s was the first planned occlusion event of the movement sequence. The large deviation at t=63.5 s was the occlusion event described in more detail in the associated text with Figure 4.7 and its associated text. Finally, the large deviation at t=247.6 s occurred because one of the experimentalists was at the edge

of the video camera's field of view and wasn't detected by the VOD. The next highest SCP was therefore the closest detected object, which was at the center of the field of view. Despite these VOD and VOT failures during occlusion events, the data fusion improved the directionality performance from a MAE of 19 $\pm$ 17^o to a MAE of 4 $\pm$ 6^o: an improvement of 79%. A fraction of the improvement is due to constraining directionality estimates to detected objects on a second-by-second basis; however, the majority of this improvement is the accounting of object movement from the video stream, allowing multiple radiation directionality estimates to accrue on a tracked object.

Similar improvements were observed in the 95 μ Co-57 source case. Using only radiation data to determine the most likely source carrier, the top of Figure 4.10 shows a MAE of 18 $\pm$ 15 ^{o}, where the fluctations are again due to the low statistics nature of the measurements. Using both radiation and video data to determine the most likely source carrier, the bottom of Figure 4.10 shows a MAE of 6 $\pm$ 6 ^{o}. Once again, the large deviations in the data fused result are due to source carrier misattribution. For example, the large deviation at t=16 s is due to the experimentalist in the middle of the FOV not being detected by the VOD algorithm due to his strange pose. Consequently, the nearest experimentalist was deemed the most likely source carrier. At t=29 s, the large deviation was caused by an unplanned occlusion event where the entire FOV was blocked by a single experimentalist close to the RGB camera. At t=41 s, the large deviation was caused by a planned occlusion event during the experiment. Despite these VOD and VOT failures, data fusion once again improved directionality performnace from a MAE of 18 $\pm$ 15 ^{o} to a MAE of 6 $\pm$ 6 ^{o}: an improvement of 67%. Once more, the majority of this improvement is the accounting of object movement from the video stream, allowing multiple radiation directionality estimates to accrue on a tracked object.

4.4 Conclusions

Both radiation and video data were used to generate source carrier probabilities for moving objects with complex and arbitrary motion including object occlusion. A radiation directionality algorithm was applied to closely packed, wearable radiation detector array of

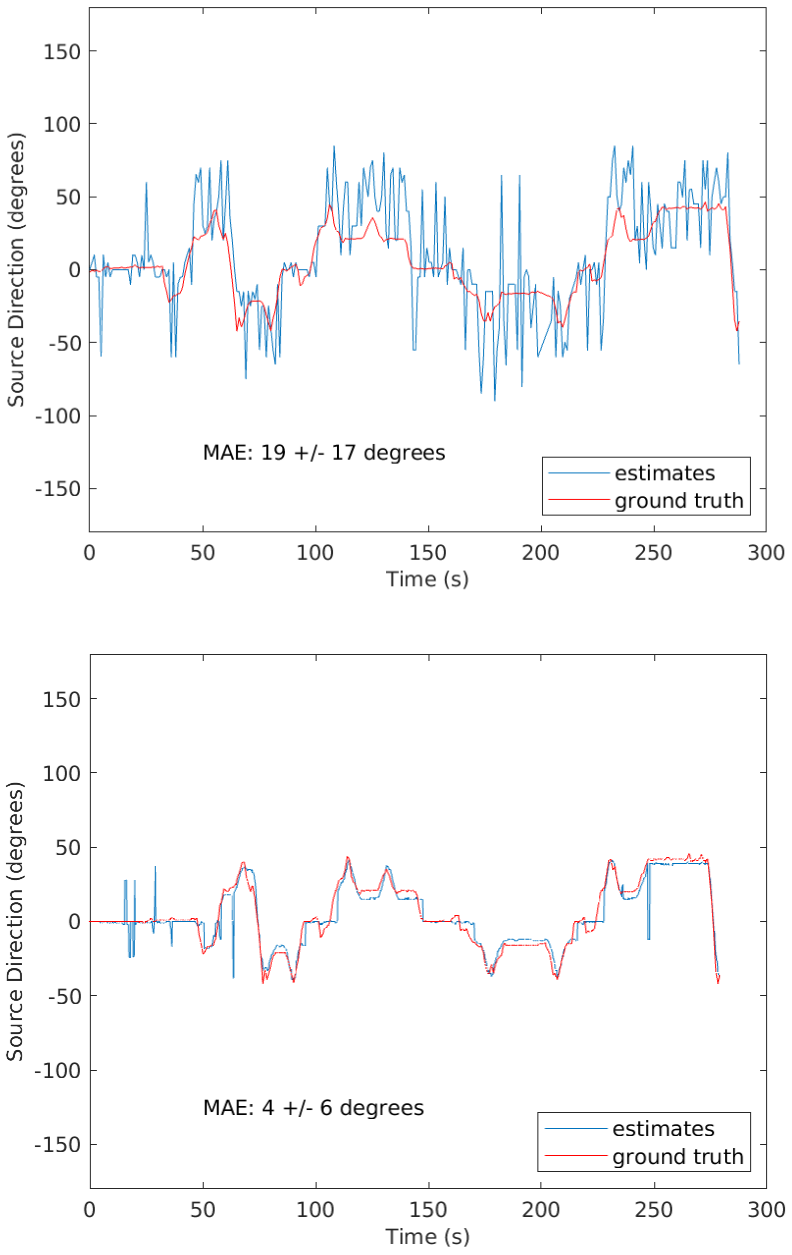


Figure 4.9: 113 μCi Cs-137 directionality results. (Top) Radiation data only. (Bottom) Video and radiation data fused result.

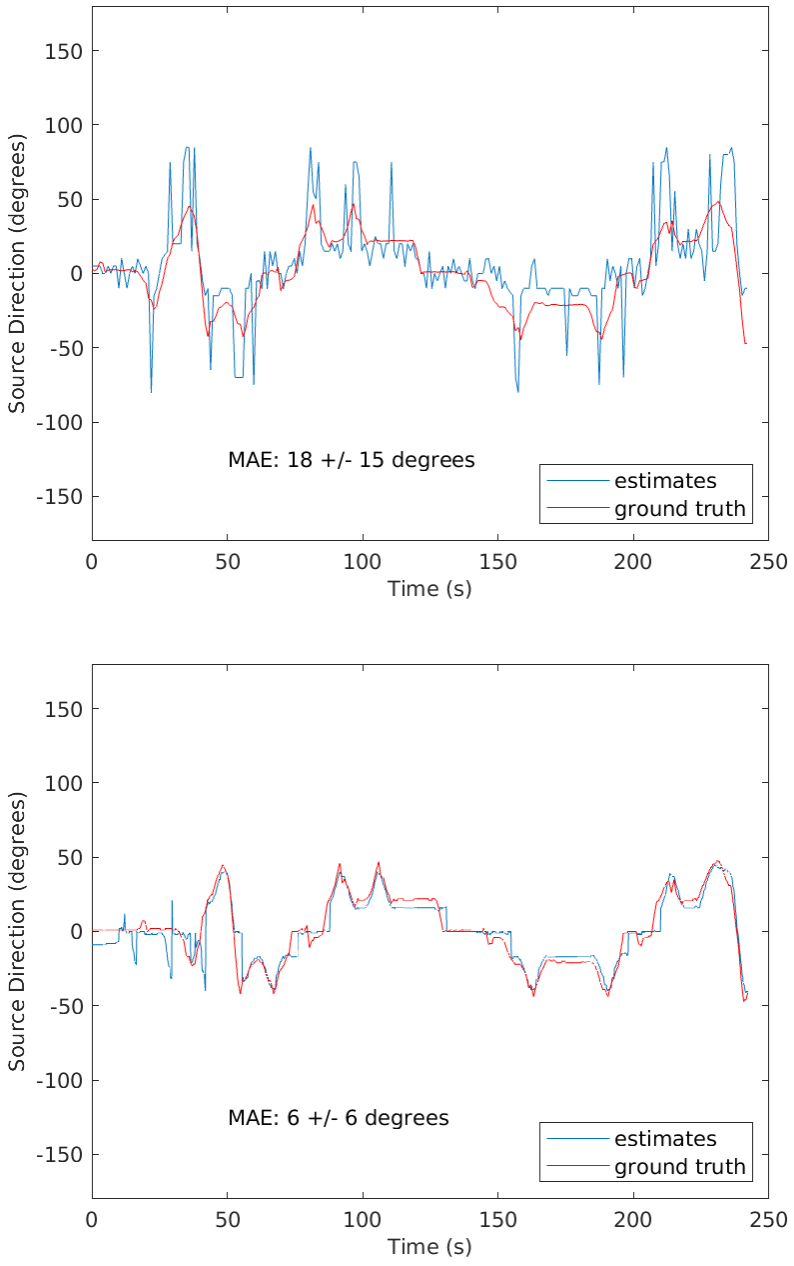


Figure 4.10: 95 μCi Co-57 directionality results. (Top) Radiation data only. (Bottom) Video and radiation data fused result.

NaI(Tl) and CLYC(Ce) detectors, with a total detector mass of 4.7 kg. The experiment conducted only involved a gamma radiation source; however, the detector payload is both gamma and neutron sensitive. Computer vision algorithms were used to infer object movement with respect to time, such that both the radiation and video data could be correlated with one another. With a 113 μCi Cs-137 source, the MAE was found to be 19 $\pm$ 17^o with radiation data only and 4 $\pm$ 6^o with the data fused result, a 79 % improvement. With a 95 μ Co-57 source, the MAE was found to be 18 $\pm$ 15 ^{o} with radiation data only and 6 $\pm$ 6 ^{o} with the data fused result, a 67 % improvement. In both cases, the observed improvement is due to the accounting of object movement from the video stream, which facilitated multiple radiation directionality estimates to be made on the same object.

Future work includes describing directionality performance during a source pursuit scenario. The operator would be guided in his or her movement in the pursuit of source carrier in motion through a populated search space. A comparison would be made in the source pursuit outcomes between the radiation only and data fusion cases.

4.5 Acknowledgements

This material is based upon work supported by both the Department of Homeland Security and Department of Energy National Nuclear Security Administration under Award Numbers DHS-15-DNDO-077-001, DE-NA0002576, and DE-NA0003180. This report was prepared as an account of work sponsored by an agency of the United States Government. Neither the United States Government nor any agency thereof, nor any of their employees, makes any warranty, express or implied, or assumes any legal liability or responsibility for the accuracy, completeness, or usefulness of any information, apparatus, product, or process disclosed, or represents that its use would not infringe privately owned rights. Reference herein to any specific commercial product, process, or service by trade name, trademark, manufacturer, or otherwise does not necessarily constitute or imply its endorsement, recommendation, or favoring by the United States Government or any agency thereof. The views and opinions of authors expressed herein do not necessarily state or reflect those of the United States Government or any agency thereof.

Chapter 5

Conclusions

Radiation directionality was characterized for a detector array comprised of 3 NaI(Tl) of 2" × 2" × 4" dimension. The directioinality Mean Absolute Error (MAE) was found to be 8.1^o for a 113 μCi Cs-137 source at a distance of 172.4 cm and 17.9^o for a 35 μCi Co-60 at the same distance. The directionality performance increase was quantified when the unattenuated gamma fluence increases, such that the change of directionality performance can be estimated for this array when the source distance or strength changes. Furthermore, this directionality algorithm was demonstrated to have a MAE of 12.7 m/s on a moving 113 μCi Cs-137 source with an average source distance of 4 ± 1 m and speed of 0.5 m/s.

The source localization capabilities for the WIND Backpack detector array with the 2 NaI(Tl), 2 CLYC detector configuration was characterized. The 95 μCi Co-57 source could be localized to less than a meter with source offsets less than 4.2 m, while 113 μCi Cs-137 source could be localized to less than a meter with source offsets less than 3.2 m. It was found that either decreasing the integration time or detector array speed would improve source localization results by decreasing motion blurring effects. These conclusions aren't surprising, but add to the existing literature by the system used within the measurement: closely-packed detector arrays consisting of essentially 3 detectors and 4.9 kg of mass.

A data fusion strategy was developed which incorporated the video data from an RGB camera to the directionality estimates. The directionality MAE using only radiation data was 18 ± 15^o and 19 ± 17^o for the 95 μCi Co-57 and 113 μCi Cs-137 sources, respectively.

This performance improved to 4 ± 6^o and 6 ± 6^o upon inclusion of video data: a performance increase of approximately 50% in each case.

All of these capabilities were developed and demonstrated on a closely-packed, human portable, backpack-sized radiation detector array. These methods are detector agnostic, which is to say they were developed for any closely-packed detector array of any configuration, such as the arrays packaged within ARBL or MURS.

5.1 Future Work

Radiation directionality algorithm could use a gamma energy correction. For example, an experimentalist would measure the angular response for Co-57 and Co-60, then interpolate the angular response for Cs-137. This would save time as the experimentalist would not have to measure the response for every possible source, especially when taking the WIND Backpack detector array's modular nature into account: new detector configurations would require the angular response to be measured.

The entire capability of the WIND Backpack detector array has not been entirely investigated. This work only covered the measured dataset, which is miniscule in comparison to the infinite amount of synthetic radiation data one could generate with a validated test bed for this detector array. With this validated test bed, the system's operational domain can be discovered.

There is a significant amount of research potential with regard to data fusion. Inclusion of more sophisticated contextual sensors such as stereoscopic RGB cameras include distance information that would enable implementation of source localization algorithms, such as MLEM shown in Chapter 3. Or perhaps replace the RGB camera with a LIDAR, where LIDAR segmentation (equivalent to object detection) would have its own set of challenges. Replacing the RGB camera with a 360^o camera would require video preprocessing such that the video algorithms would still work, but recent research shows that it can be done [21, 43]. This would equip the WIND Backpack detector array with contextual sensors of similar caliber to References [17], [28], [16], and [3]. Furthermore, it is unclear how these data fusion backpack systems would work cooperatively with one another, as cooperation implies

understanding of object identity. For example, the orange experimentalist detected from backpack A is the same orange experimentalist detected from backpack B, such that the SCP should reinforce one another across both systems. This would require the use of object reidentification algorithms [33, 27].

5.2 Acknowledgements

This material is based upon work supported by both the Department of Homeland Security and Department of Energy National Nuclear Security Administration under Award Numbers DHS-15-DNDO-077-001 and DE-NA0002576. This report was prepared as an account of work sponsored by an agency of the United States Government. Neither the United States Government nor any agency thereof, nor any of their employees, makes any warranty, express or implied, or assumes any legal liability or responsibility for the accuracy, completeness, or usefulness of any information, apparatus, product, or process disclosed, or represents that its use would not infringe privately owned rights. Reference herein to any specific commercial product, process, or service by trade name, trademark, manufacturer, or otherwise does not necessarily constitute or imply its endorsement, recommendation, or favoring by the United States Government or any agency thereof. The views and opinions of authors expressed herein do not necessarily state or reflect those of the United States Government or any agency thereof.

Bibliography

[1] Aucott, T. J., Chivers, D. H., and Vetter, K. (2011). Proximity localization with the mobile imaging and spectroscopic threat identification (misti) system. In *IEEE Nuclear Science Symposium Conference Record*, pages 1303–1305. xi, 11, 12

[2] Ayaz-Maierhafer, B., Britt, C. G., August, A. J., Qi, H., Seifert, C. E., and Hayward, J. P. (2017). Design optimization for a wearable, gamma-ray and neutron sensitive, detector array with directionality estimation. *Nuclear Inst. and Methods in Physics Research, A*, 870:131–139. 26, 30, 62, 71

[3] Barnowski, R., Haefner, A., Mihailescu, L., and Vetter, K. (2015). Scene data fusion: Real-time standoff volumetric gamma-ray imaging. *Nuclear Instruments and Methods in Physics Research, A*, 800. xii, 22, 27, 118

[4] Bertinetto, L., Valmadre, J., Henriques, J. F., Vedaldi, A., and Torr, P. H. (2016). Fully-convolutional siamese networks for object tracking. In *European conference on computer vision*, pages 850–865. Springer. 102

[5] Britt, C., Wen, X., Qi, H., and Hayward, J. (2021). Directionality for wearable, closely packed radiation detector arrays. *Nuclear Instruments and Methods in Physics Research Section A: Accelerators, Spectrometers, Detectors and Associated Equipment*, 986:164708. 32, 33, 64, 97

[6] Bubble Technology Industries (2013). Flexspec mobile. Available at http://bubbletech.ca/product/flexspec-2/. 3

[7] Curtis, J. C., Cooper, R. J., Joshi, T. H., Cosofret, B., Schmit, T., Wright, J., Rameau, J., Konno, D., Brown, D., Otsuka, F., Rappeport, E., Marshall, M., and Speicher, J. (2020). Simulation and validation of the mobile urban radiation search (murs) gamma-ray detector response. *Nuclear Instruments and Methods in Physics Research Section A: Accelerators, Spectrometers, Detectors and Associated Equipment*, 954:161128. Symposium on Radiation Measurements and Applications XVII. x, 6, 8, 95

[8] Deb, B., Ross, J. F., Ivan, A., and Hartman, M. J. (2011). Radioactive source estimation using a system of directional and non-directional detectors. *IEEE Transactions on Nuclear Science*, 58(6):3281–3290. xii, 17, 24, 34, 69, 95

[9] Department of Homeland Security (2013a). Standoff radiation detectors market survey report. Available at https://www.dhs.gov/sites/default/files/publications/SRDs-MSR_0813-508_0.pdf. 1, 2, 3

[10] Department of Homeland Security (2013b). Summary: Radiation detection backpacks. Available at https://www.dhs.gov/sites/default/files/publications/RadBackpacks-SUM_0113-508.pdf. 2, 3

[11] Department of Homeland Security (2015). Handheld radionuclide identification devices (rids) market survey report. Available at https://www.dhs.gov/sites/default/files/hhrid-msr_0915-508.pdf. 2, 3

[12] Department of Homeland Security (2017). Personal radiation detectors (prds) and spectroscopic prds market survey report. Available at https://www.dhs.gov/sites/default/files/NUSTL-SAVER_PRD-SPRD-MSR_1707-508.pdf. 2, 3

[13] Detwiler, R., Pfund, D., Myjak, M., Kulisek, J., and Seifert, C. (2015). Spectral anomaly methods for aerial detection using kut nuisance rejection. *Nuclear Inst. and Methods in Physics Research, A*, 784:339–345. 95, 140

[14] FLIR (2015). All-purpose radionuclide identification device identifinder r400. Available at https://www.flir.com/products/identifinder-r400/. 3

[15] Gueorguiev, A., Preston, J., Hoy, L., Pausch, G., Herbach, C.-M., and Stein, J. (2010). A novel method to determine the directionality of radiation sources with two detectors based on coincidence measurements. In *IEEE Nuclear Science Symposuim & Medical Imaging Conference*, pages 1525–1530. IEEE. xii, 19, 20, 21

[16] Haefner, A., Gunter, D., Plimley, B., Pavlovsky, R., and Vetter, K. (2014). Gamma-ray momentum reconstruction from compton electron trajectories by filtered back-projection. *Applied physics letters*, 105(18):184101–. 6, 118

[17] Henderson, K., Liu, X., Stadnikia, K., Martin, A., Enqvist, A., and Koppal, S. J. (2020). Proximity-based sensor fusion of depth cameras and isotropic rad-detectors. *IEEE Transactions on Nuclear Science*. xiii, 22, 26, 28, 118

[18] Hite, J. and Mattingly, J. (2019). Bayesian metropolis methods for source localization in an urban environment. *Radiation Physics and Chemistry*, 155:271–274. 34, 95

[19] Hite, J., Mattingly, J., Archer, D., Willis, M., Rowe, A., Bray, K., Carter, J., and Ghawaly, J. (2019). Localization of a radioactive source in an urban environment using bayesian metropolis methods. *Nuclear Instruments and Methods in Physics Research Section A: Accelerators, Spectrometers, Detectors and Associated Equipment*, 915:82 – 93. xii, 17, 22, 25, 69

[20] Huh, S., Maltz, J., Gunter, D., Mihailescu, L., and Vetter, K. (2012). Real-time radioactive source localization with a moving coded-aperture detector system at low count rates. pages 666–673. IEEE. x, 2, 5, 34, 88

[21] Itakura, K. and Hosoi, F. (2020). Automatic tree detection from three-dimensional images reconstructed from 360° spherical camera using yolo v2. *Remote Sensing*, 12(6):988. 118

[22] Jaworski, J. M., Wahl, C. G., Wang, W., Fessler, J. A., and He, Z. (2013). Model-based reconstruction of spectral and spatial source distribution for objects with known motion. *IEEE Transactions on Nuclear Science*, 60(5):3981–3989. 97

[23] Joshi, T. H. Y., Quiter, B. J., Maltz, J. S., Bandstra, M. S., Haefner, A., Eikmeier, N., Wagner, E., Luke, T., Malchow, R., and Mccall, K. (2017). Measurement of the energy-dependent angular response of the ares detector system and application to aerial imaging. *IEEE Transactions on Nuclear Science*, 64(7):1754–1760. x, 6, 10, 95

[24] Kaye, S. J., Kaye, W. R., and He, Z. (2009). Experimental demonstration of coded aperture imaging using thick 3d-position-sensitive cdznte detectors. In *IEEE Nuclear Science Symposium Conference Record*, pages 1902–1906. 97

[25] Kulisek, J. A., Wittman, R. S., Miller, E. A., Kernan, W. J., Mccall, J. D., Mcconn, R. J., Schweppe, J. E., Seifert, C. E., Stave, S. C., and Stewart, T. N. (2018). A 3d simulation look-up library for real-time airborne gamma-ray spectroscopy. *Nuclear Inst. and Methods in Physics Research, A*, 879:84–91. x, xxi, 6, 9, 134

[26] Lehner, C. E., Zhong He, and Feng Zhang (2004). 4/spl pi/ compton imaging using a 3-d position-sensitive cdznte detector via weighted list-mode maximum likelihood. *IEEE Transactions on Nuclear Science*, 51(4):1618–1624. 6

[27] Li, X., Qi, Y., Wang, Z., Chen, K., Liu, Z., Shi, J., Luo, P., Tang, X., and Loy, C. C. (2017). Video object segmentation with re-identification. *arXiv preprint arXiv:1708.00197*. 119

[28] Marshall, M. R., Hellfeld, D., Joshi, T. H. Y., Salathe, M., Bandstra, M. S., Bilton, K. J., Cooper, R. J., Curtis, J. C., Negut, V., Shurley, A. J., and Vetter, K. (2021). 3-d object tracking in panoramic video and lidar for radiological source–object attribution and improved source detection. *IEEE Transactions on Nuclear Science*, 68(2):189–202. xii, 22, 26, 28, 118

[29] Miller, E. A., Robinson, S. M., Anderson, K. K., Mccall, J. D., Prinke, A. M., Webster, J. B., and Seifert, C. E. (2015). Adaptively reevaluated bayesian localization (arbl): A novel technique for radiological source localization. *Nuclear Inst. and Methods in Physics Research, A*, 784:332–338. x, xi, 6, 9, 11, 14, 15, 34, 36, 63, 68, 69, 94, 95

[30] Mukhopadhyay, S., Maurer, R., Wolff, R., Mitchell, S., Guss, P., and Trainham, C. (2013). Exploitation of geometric occlusion and covariance spectroscopy in a gamma sensor array. In *Hard X-Ray, Gamma-Ray, and Neutron Detector Physics XV*, volume 8852, page 88520H. International Society for Optics and Photonics. xii, 19, 21

[31] ORTEC (2013). Detective-ex-100t and detective-dx-100t hpge-based hand-held radioisotope identifiers. Available at https://www.ortec-online.com/-/media/ametekortec/brochures/detective-100t.pdf. 3

[32] Passport Systems Inc. (2015). Nets2 smartshield g300 radiation detector. Available at https://passportsystems.com/wp-content/uploads/2020/05/1405946923smartshield_g300_product-sheet.pdf. 3

[33] Peng, L., Yang, Y., Qi, X., and Wang, H. (2014). Highly accurate video object identification utilizing hint information. In *2014 International Conference on Computing, Networking and Communications (ICNC)*, pages 317–321. IEEE. 119

[34] Penny, R. D., Crowley, T. M., Gardner, B. M., Mandell, M. J., Guo, Y., Haas, E. B., Knize, D. J., Kuharski, R. A., Ranta, D., Shyffer, R., Labov, S., Nelson, K., Seilhan, B., and Valentine, J. D. (2015). Improved radiological/nuclear source localization in variable norm background: An mlem approach with segmentation data. *Nuclear Inst. and Methods in Physics Research, A*, 784:319–325. xi, 6, 13, 16, 34, 69

[35] Quiter, B. J., Joshi, T. H. Y., Bandstra, M. S., and Vetter, K. (2016). Csi(na) detector array characterization for ares program. *IEEE Transactions on Nuclear Science*, 63(2):673–678. 6

[36] Redmon, J. and Farhadi, A. (2018). Yolov3: An incremental improvement. *arXiv preprint arXiv:1804.02767*. 98, 102

[37] Royston, J. (1983). Some techniques for assessing multivarate normality based on the shapiro-wilk w. *Journal of the Royal Statistical Society: Series C (Applied Statistics)*, 32(2):121–133. 42

[38] Royston, J. (1992). Approximating the shapiro-wilk w-test for non-normality. *Statistics and Computing*, 2:117–119. 42

[39] Sensor Technology Engineering (2013). Radpack backpack-based radiation detection system. Available at https://ste-sb.com/radpack/. 3

[40] Sullivan, J. P., Tornga, S. R., and Rawool-Sullivan, M. W. (2009). Extended radiation source imaging with a prototype compton imager. *Applied Radiation and Isotopes*, 67(4):617–624. 34, 95

[41] Vilim, R., Klann, R., and Thomas, J. (2011). Integrated treatment of detector arrays for source tracking. *Nuclear Technology*, 175:314–325. xi, xii, 17, 18, 19, 23, 34

[42] Wahl, C. G., Kaye, W. R., Wang, W., Zhang, F., Jaworski, J. M., King, A., Boucher, Y. A., and He, Z. (2015). The polaris-h imaging spectrometer. *Nuclear Instruments and Methods in Physics Research Section A: Accelerators, Spectrometers, Detectors and Associated Equipment*, 784:377 – 381. Symposium on Radiation Measurements and Applications 2014 (SORMA XV). 6

[43] Wang, K.-H. and Lai, S.-H. (2019). Object detection in curved space for 360-degree camera. In *ICASSP 2019-2019 IEEE International Conference on Acoustics, Speech and Signal Processing (ICASSP)*, pages 3642–3646. IEEE. 118

[44] Willis, M. J., Skutnik, S. E., and Hall, H. L. (2014). Detection and positioning of radioactive sources using a four-detector response algorithm. *Nuclear Instruments and Methods in Physics Research Section A*, 767:445–452. 19, 34, 36, 97

[45] Ziock, K., Boehnen, C., Ernst, J., Fabris, L., Hayward, J., Karnowski, T., Paquit, V., Patlolla, D., and Trombino, D. (2016). Motion correction for passive radiation imaging of small vessels in ship-to-ship inspections. *Nuclear Inst. and Methods in Physics Research, A*, 805:116–126. 22, 95

[46] Ziock, K., Collins, J., Fabris, L., Gallagher, S., Horn, B., Lanza, R., and Madden, N. (2006). Source-search sensitivity of a large-area, coded-aperture, gamma-ray imager. *IEEE transactions on nuclear science*, 53(3):1614–1621. x, 2, 4, 97

Appendix

A Source Localization Using the Government Reference System

A.1 Preliminary Dataset

Results shown in this appendix was collected using a 6 Sodium Iodide (NaI) detector array, named the Government Reference System (GRS), in the configuration shown in the left of Figure 1. All the detectors have a 2" diameter. Detectors 1, 3, 4, and 6 have a 4" height, while detectors 2 and 5 have a 2" height. The phantom consists of a polymethyl methacrylate (PMMA) block. The measured angular response of the system is shown in the right half of Figure 1 collected by Archer et al's group at Oak Ridge National Laboratory using an automated rotating stage setup shown in Figure 2. The experiment measures the angular response of the system due to a 25 μCi Cs-137 source in 15 degree increments. First, the background at each angular position was taken for 20 minutes. After the background measurement, a 25 μCi Cs-137 source was placed at a fixed position 2m from the center of the PMMA block, and another round of rotational measurements were taken with 10 minutes at each position. With this, the background was subtracted at each matching position to yield the right of Figure 1. The total uncertainty for the count rate for all of the measured locations is less than 1 cps for all position. The algorithms use this angular information by incorporating it into the ray tracing function, $f(\theta)$, unless stated otherwise.

This measurement platform was driven in a straight line by a 50 μCi Cs-137 source 3 meters away from the Point of Closest Approach (PoCA). Unfortunately, a high fidelity ground truth location of the source was not logged for this measurement, so no assessment can be made on the accuracy on any of the methods for this dataset. The data consists of both GPS and energy spectra taken in 0.1s intervals, as shown in Figure 3. The high fluctuation in the signal as well as the volume of measurements are not ideal for the algorithms employed, so the integration time was changed from 0.1s to 1s by summing across 10 measurements. Each count rate measurements adopts the 10th GPS location of measurement. Fundamentally, this trades position fidelity for a decrease in noise and calculation time. The aggregation can be seen in Figure 4, which serves as the ultimate input for the source localization algorithms.

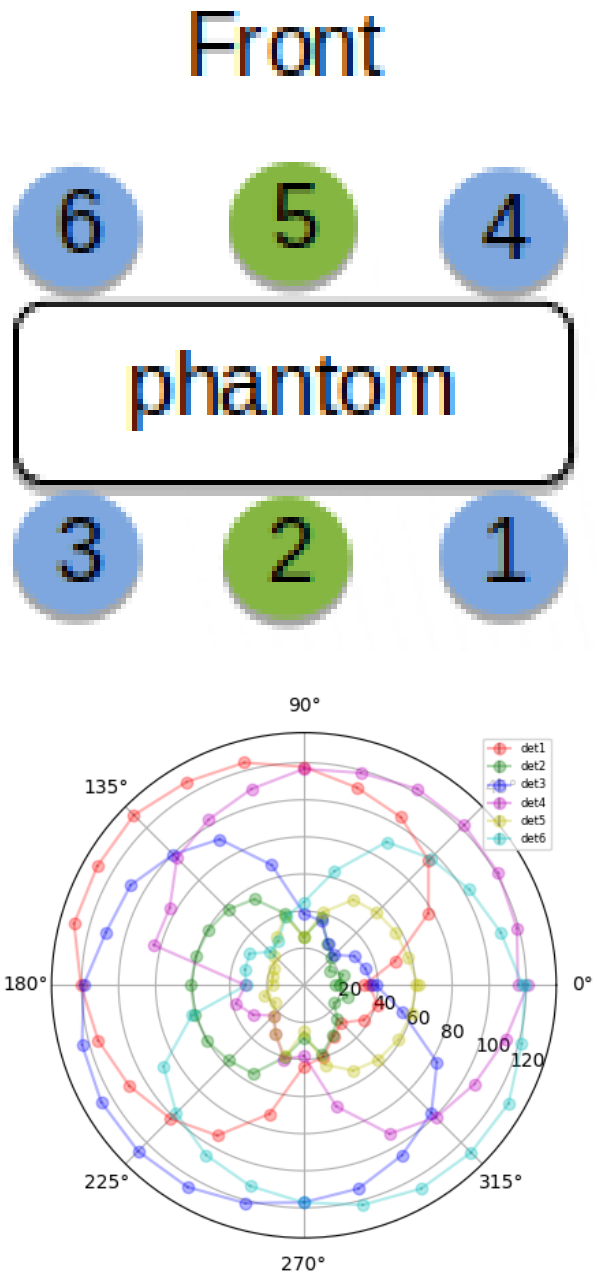


Figure 1: (Top) Detector array configuration. (Bottom) Angular response (count rate in cps) with uncertainties of the detector array to a 25 μCi source placed 2m away.

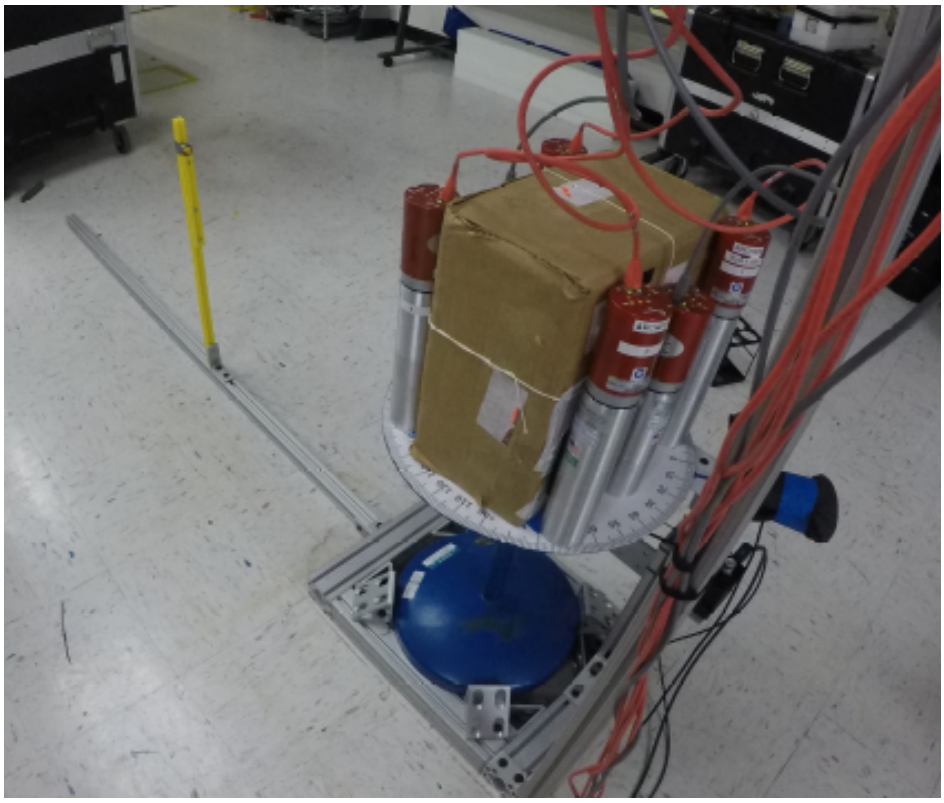


Figure 2: Rotating stage setup. The detector array rotates at a fixed position and the source is in a fixed position.

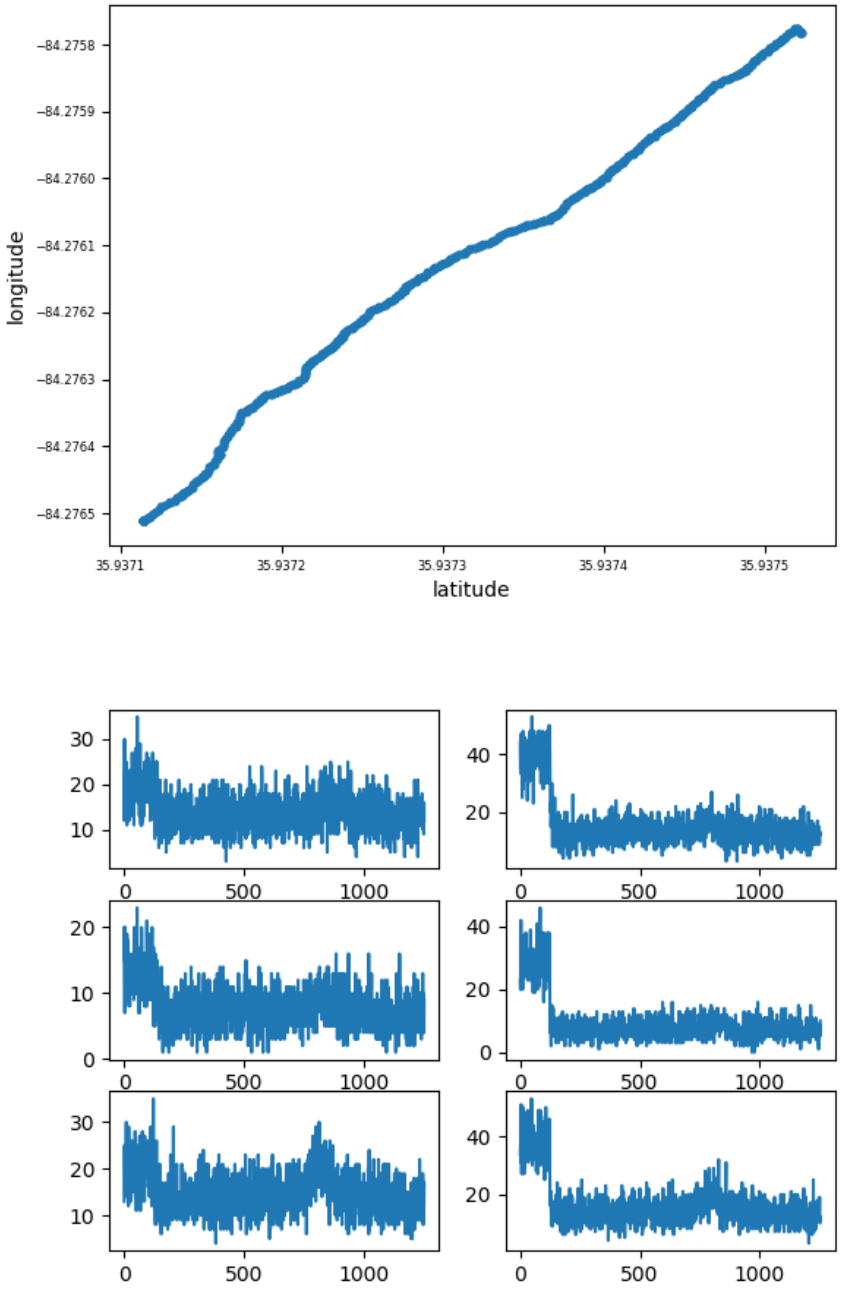


Figure 3: (Top) GPS location of each measurement. Actual movement of the measurement platform was a straight line at a constant velocity. (Bottom) Count rate measured at each measurement interval every 0.1s.

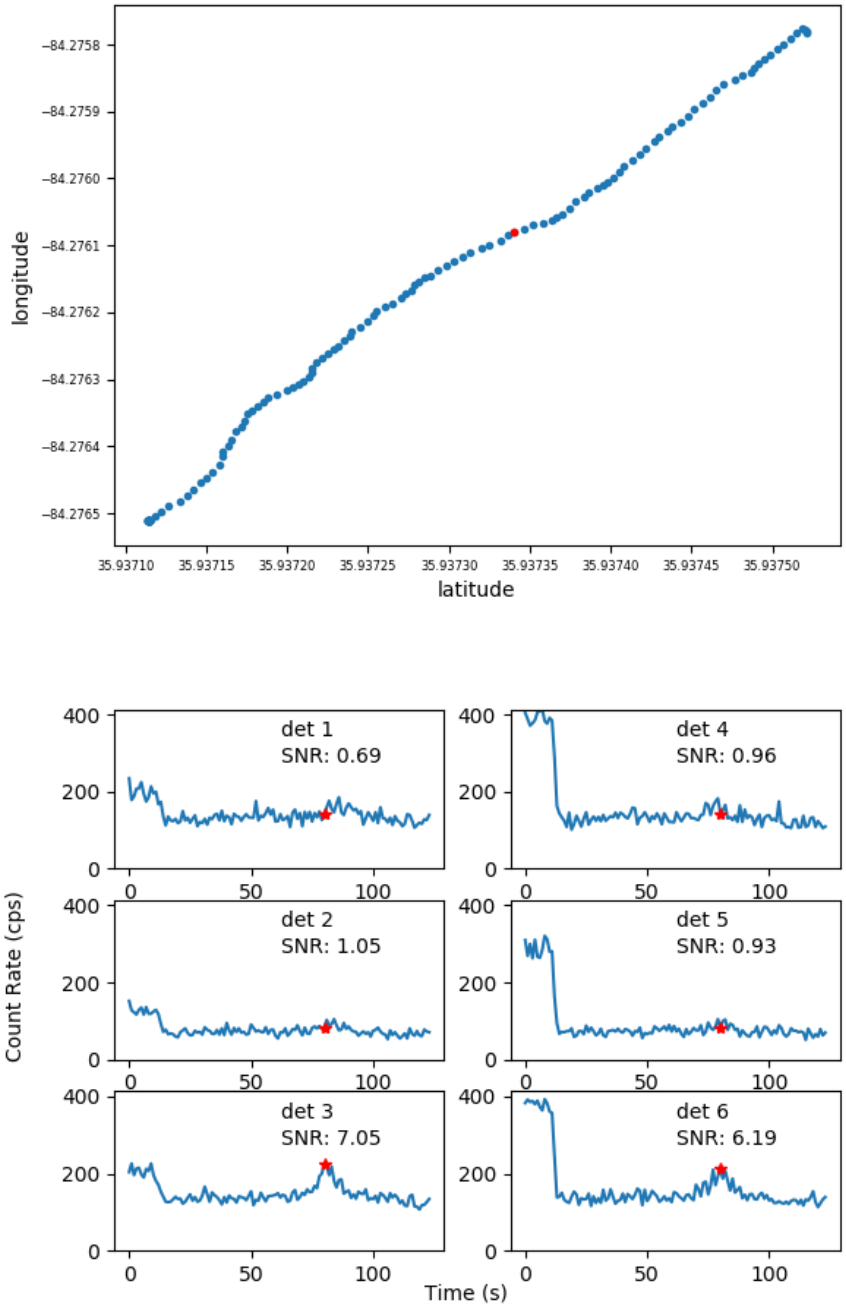


Figure 4: (Top) GPS location of each aggregated measurement. The red dot denotes the location of the estimated Point of Closest Approach. (Bottom) Count rate after aggregating the raw measurements to an integration time of 1s. The red dot denotes the estimated Point of Closest Approach. The SNR for the PoCA location is also provided.

To estimate PoCA, an adhoc procedure was used for this dataset to get an idea of the Signal to Noise ratio (SNR). The definition for Signal to Noise Ratio (SNR) used in this work is $SNR(x_i) \approx \frac{S_i}{\sqrt{B_i}}$, where it is assumed that each measurement, x_i, is composed of a signal, S_i, (counts contributed by the source being present) and background, B_i (counts contributed by natural background radiation). The background is assumed to be the median value of a given set of measurements. The PoCA location is based on the detector with the highest SNR value after 30 seconds. This was done to adjust for individual detector gains, as well as to accommodate the initial increased count rate in all of the detectors due to experimental procedure to synchronize the measurement indexes.

A.2 Preliminary Results

Demonstrations of the source localizations methods mentioned in Chapter 1 are applied to this preliminary dataset. Note that at the location of each measurement, there are concentric circles of decreased probability regions of where the source might be. This is a hack introduced in the implementation such that there is not an infinite probability directly under the location of the measurement platform. Note that the pdf evaluated within these regions are still non-zero, as other measurement locations can still provide perspective on those locations that have been artificially suppressed. Each result uses the viridis colormap, where regions of low probability are denoted in blue, while high regions of probability are denoted in yellow. Finally, the colors shown at each pixel is the log posterior probability to make comparisons to each method as well as the literature.

The left of Figure 5 shows the localization result using MLE. The skewness of the distribution towards the South side of the path suggests that the angular response is being utilized to some degree in the result. The final source estimate is an amorphous blob, which is similar in behavior to Kulisek et al's result in the right of Figure 1.5, which has been duplicated in the right of Figure 5 for the reader's convenience. Figure 6 shows the localization result using MLEM, where there there is more conviction on the source's location as shown in the decreased width of the white contours denoting the Gaussian fit.

Figure 7 is the result of 4.8 million samples of the posterior probability distribution using MCMC. This figure is a 2D histogram which tallies how often a particular source state was

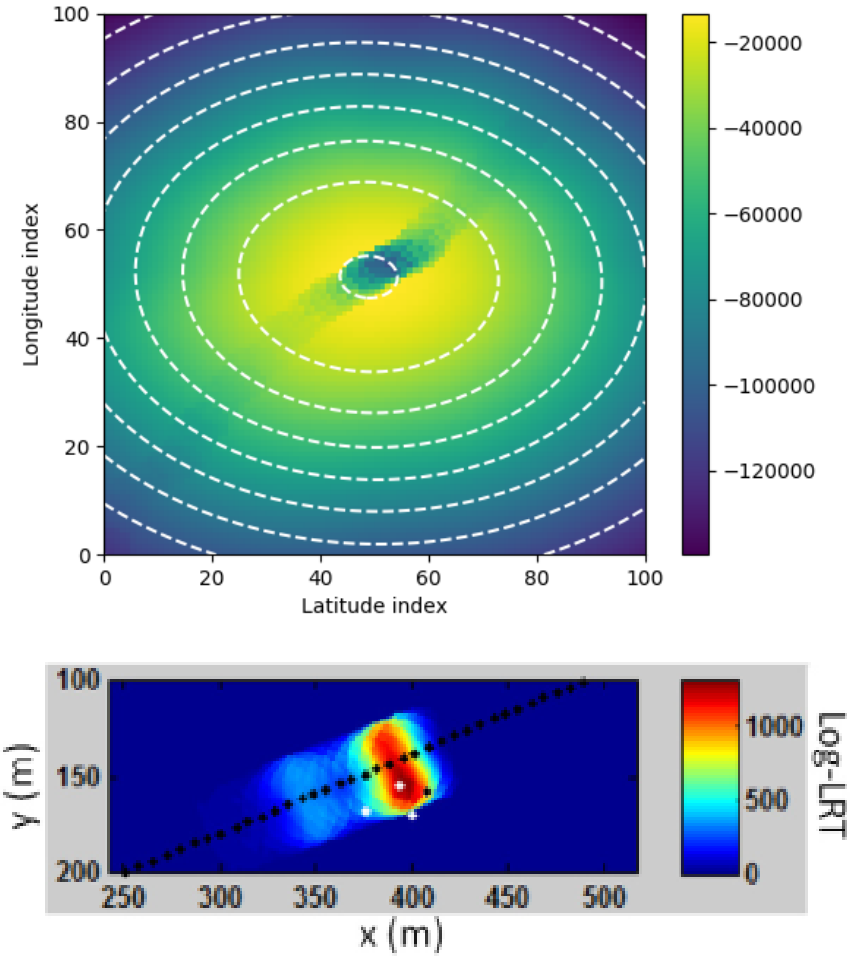


Figure 5: (Top) MLE result. White lines are the contours of the 2D Gaussian fit. The pixel color denotes the log probability value of the posterior. (Bottom) MLE result from Reference [25].

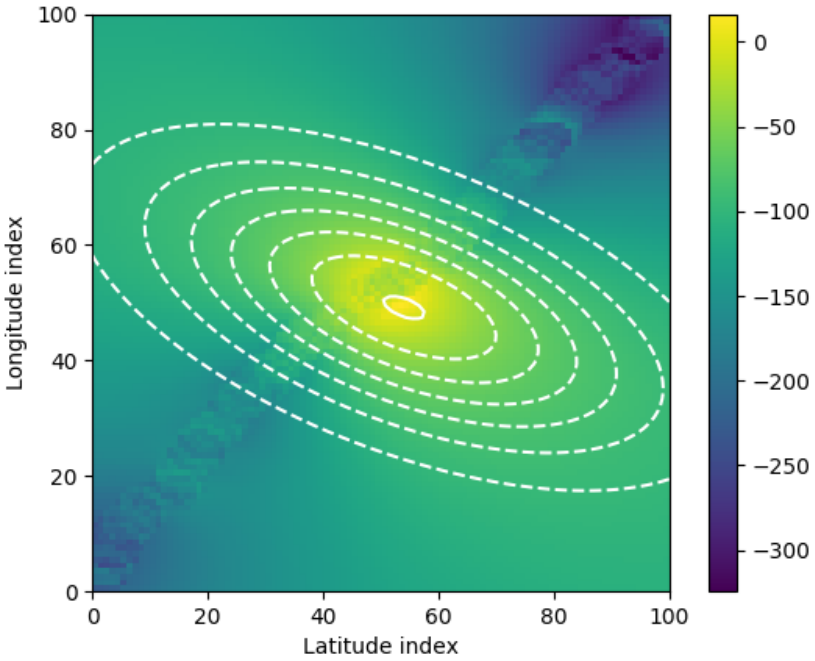


Figure 6: MLEM Result. White lines are the contours of the 2D Gaussian fit. The pixel color denotes the log probability value of the posterior.

chosen. Unlike the other methods, the color in the figure are the number of times a state was chosen, where the mode of the source states is the most likely source state which drives the observations. The observed pixelation is an artifact of the sampling nature of the method and is expected to vanish as the number of samples tend towards infinity. Asymmetry is seen in the solution, which suggests that the angular response of the system helps in source localization. Admittedly, the image plotted has an error in orientation: the y-axis is flipped, due to a different method in plotting, which explains why the contour of the fit and image do not align correctly. Consequently, the fitting position in Table 1 is inaccurate; however, the width of the distribution indirectly measured through the Gaussian sigmas are still valid.

The left of Figure 8 showcases source localization performance using MLEM without incorporating the angular response of the detector array itself. In comparison with Figure 6, which is duplicated in the right of Figure 8, the effect of not modeling the unique angular responses from the right Figure 1 is apparent as there is much more symmetry in the posterior probability distribution. Note that there is still a little asymmetry due to the uncertainty in the measurement system's position.

Table 1 showcases 2-dimensional, unimodal, Gaussian optimal fitting parameters upon the posterior probability distributions for each of the localization approaches shown as dotted white contour lines in Figures 5, 6, 7, and 8. All the units are in pixels, where each pixel is approximately 0.72m x 0.72m in dimension. Weighted least squares is chosen as the fitting method. This fitting serves to give intuition for localization performance from each approach on this measurement platform. This by no means serves as the best localization performance to be obtained by this system, as the configuration of each method (hyper parameters, modeling behavior, etc.) has not been optimized. The strongest and honest these results can claim is that some of the behavior of each approach has been replicated and is still very much a work in progress. Ideally, the mean position of the fits would be compared to the ground truth source location to give systematic error estimates; however, this comparison cannot be done due to the lack of ground truth information. It is also interesting to note that the "total width" (last column of Table 1) is smaller for the MLEM result without angular responses information than the normal MLEM result. The author believes this is due to the

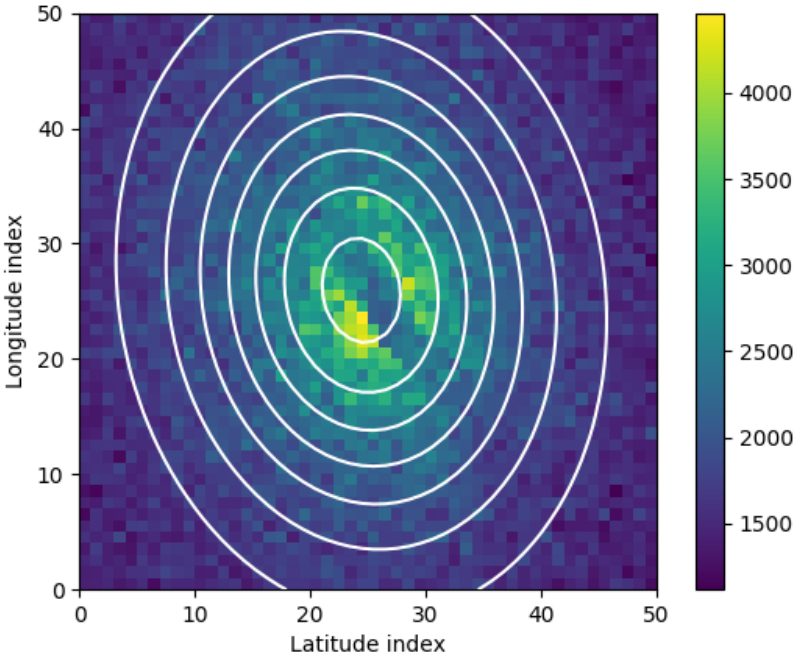


Figure 7: MCMC Result.

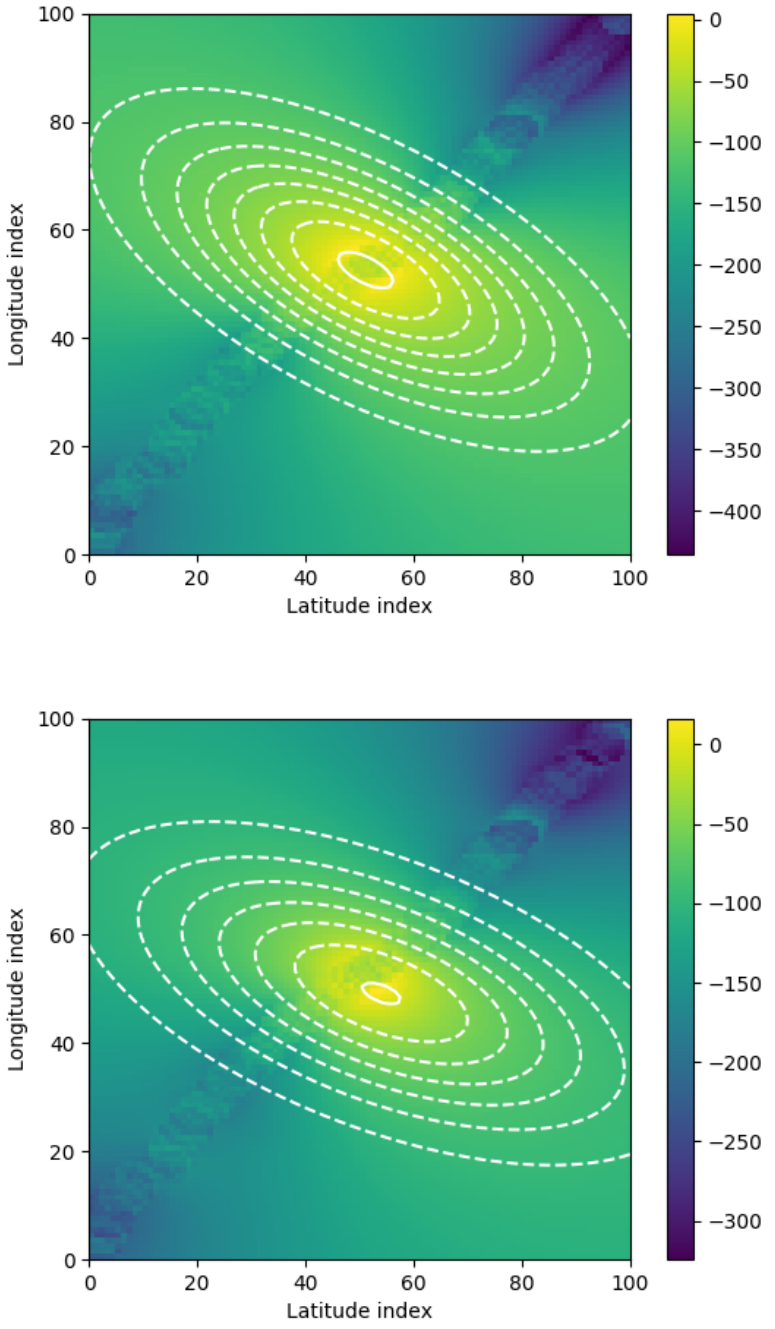


Figure 8: (Top) MLEM Result with the removal of angular response. (Bottom) MLEM Result with angular response information. Duplication of Figure 6 for the reader's convenience. (Both) White lines are the contours of the 2D Gaussian fit. The pixel color denotes the log probability value of the posterior.

Table 1: Summary of Results: 2D Gaussian optimal fitting parameters.

Approach	**position (x, y) in pixels**	**(σ_x, σ_y) in pixels**	**$\sqrt{\sigma_x^2 + \sigma_y^2}$ in pixels**
MLE	(48.9, 51.3)	(53.5, 39.0)	66.2
MLEM	(54.0, 50.8)	(12.2, 29.4)	31.8
MLEM (no angular)	(51.1, 47.4)	(26.8, 11.3)	29.1
MCMC	(48.8, 48.2)	(27.2, 20.2)	(33.9)

consistent SNR in summing the counts across all detectors compared to the fluctuation in SNR of the individual detector responses.

The source localization results are influenced by the estimates for background radiation. For the purposes of demonstration, only the median background of the entire dataset is used to help aid in source localization. In operation, the background would be discriminated against either with a rolling average, exponentially weighted moving average, or NSCRAD [13]. Using more sophisticated techniques such as these to estimate the background is expected to yield better results.

Vita

Carl G. Britt III was a Consortium for Nonproliferation Enabling Capabilities Fellow at the University of Tennessee - Knoxville from 2016. His research advanced knowledge and capabilities of a closely-packed, human portable, radiation detector array with respect to directionality, static source localization, and dynamic source localization. As a result of his interests in deep learning, he demonstrated the fusion of radiation and video data modalities to aid in the localization of moving radiation sources. He continues to look for challenges where multidisciplinary approaches are key in its solution.

He received his B. Sc. in nuclear engineering at the University of Tennessee - Knoxville in 2016 with research experience in modeling steam generators for Small Modular Reactors. He also led the top nuclear engineering senior design team in the development of radiation detectors for sensor network applications. During his undergraduate studies, he gained industry experience on safety related vendor oversight tasks during his year long technical Co-Op experience with Southern Nuclear and summer internship at Areva NP.

Most of Carl's personality stems from the interactions from individuals of diverse backgrounds. Carl spent the first 12 years of his life overseas. He was born in Manila, Philippines, and spent 2-4 years each in countries including Belize, Morocco, and Sri Lanka. He applies what he learned during his upbringing: diversity in perspective is critical for understanding. This is a theme which spans across his academic portfolio, his dissertation topic, and team interactions. However, an unintended consequence of his childhood is the constant wanderlust he attempts to keep at bay with hobbies which involve some level of travel: competitive swing dancing and cycling.